Super-MeV Compton Imaging and 3D Gamma-Ray Imaging Using Pixelated CdZnTe

by

Daniel Shy

A dissertation submitted in partial fulfillment
of the requirements for the degree of
Doctor of Philosophy
(Nuclear Engineering and Radiological Sciences)
in The University of Michigan
2020

Doctoral Committee:

Professor Zhong He, Chair
Professor Christine Aidala
Professor Jeffrey Fessler
Professor Igor Jovanovic
Dr. Scott Thompson

Daniel Shy

danielshy@danielshy.com

ORCID iD: 0000-0002-3699-265X

למשפחה שלי

ACKNOWLEDGEMENTS

I was told that one of the most difficult tasks in scheduling the defense would be to get 5 committee members all in the same room together. This was very true in my PhD journey when I tried to plan my prospectus as it was postponed due to the polar vortex ($\leq -45°$F), which resulted in the closing of the school. The defense proved more difficult as a result of the COVID-19 pandemic. I thank everyone who was able to join me the day of my defense, physically and remotely.

Special thanks to Dr. Zhong He, who has inspired me to work harder and smarter. He molded the basis of my research techniques and critical thought process. Not only did he teach me 'How', but to also ask 'Why?'. Huge credit to elevating my education experience is given to Niral Shah and Charles Leak, where we together made up the 'Three Musketeers', as Tony used to call us in our early years. It is the attention to detail that we had for each other that really influenced me (and the group) to become more rigorous in both our academic and social thought process.

Extreme appreciation is given to Prof. Fessler for teaching elegance and has greatly influenced me as a researcher. Each comment that he made was met with extreme analysis that eventually influenced this work. From his comments, even at ones that are directed towards non-imaging work, I have learned to step back and rely on some principle and basic components to assist in building the argument. Thanks to Dr. Scott Thompson, who has tolerated a dewy-eyed undergrad when he was stuck with me in my first INL internship. He is at fault for everything after that. I would like to thank my other committee members, Prof. Jovanovic and Prof. Aidala for working

with me in this journey. Finally, I acknowledge Prof. Wehe for his quick wit and his superb teaching skill. I will attend any course instructed by him.

I would also like to acknowledge every past, present and future Orion group member. In particular, my former senior imaging students, Drs. Steven Brown, Jiyang Chu and David Goodman. Even following their departure from the group, I still learn from them. Although not in the Orion group, Niral has provided a great companion to learn from, bounce ideas with, and has influenced this work.

I both apologize and express gratitude to anyone who has endured reviewing my work, especially my writing monthly-report buddies, Valerie Nwadeyi and Dr. Bennett Williams. Thank you also to Sara Abraham, Erik Hall, Zhuo Chen, and Matthew Petryk who helped edit this dissertation. A large amount of respect is given to the detector team (Zhuo Chen, Drs. Jiawei Xia and Yuefeng Zhu) who not only maintained detectors but offered a platform to experiment on, which makes this thesis work a little more meaningful. The group will not be complete without Jim Berry, who offered a welcomed combat to anything.

Thanks to Dr. Andrea Pocar for giving me the first taste of research and everyone from the UMass-Amherst for providing great companionship during my undergraduate years.

During this work, Sam has provided me a pillar to reality through her love and support. But, perhaps the most impactful support originates from my family. Even the large distance has not attenuated any of it, which also demonstrates the large intensity that was emitted.

TABLE OF CONTENTS

LIST OF FIGURES

Figure

LIST OF TABLES

Table

ABSTRACT

The dissertation presents work in gamma-ray imaging in the MeV range, 3D Compton imaging, and time encoded imaging. The first thrust in high energy gamma-ray imaging begins with analyzing the artifacts produced. These factors include the increase in pair-production events, incorrect event sequencing, and charge sharing due to the larger electron clouds. They all result in shift-variant artifacts that degrade the signal-to-noise ratio as well as create artifacts that might be mistaken for a hot spot. The degradation from artifacts is discussed and possible mitigation techniques are presented to allow for recovery of the Compton image.

One of the presented mitigation techniques proposes a new sequencing algorithm for 3-or-more interaction events, called FIL-MSD. Missequencing presents one of the more dominant artifacts and by fixing the first interaction to be the largest deposited energy, the sequencing efficiency has increased by 20% in simulated data. Experimental results show an almost twofold increase in the signal to noise ratio (SNR) for simple backprojection images of a ^{22}Na (1.7 MeV) source.

The image resolution using filtered backprojection (FBP) was improved on by developing an analytical point spread function model for high energy 3-interaction events. Previous models did not account for missequencing effects in the model. Adding these effects into the model improved the resolution of the image, but at a cost of increased artifact production. In addition, the Wiener filter was formalized for spherical harmonics, which could be used for any number of interaction given an appropriate point spread function model.

Next, demonstration of a 3D Compton imaging system is accomplished via sensor fusion of a foot-mounted odometer and a CdZnTe detector. A comparison between 3D Compton imaging and inverse-square image-reconstruction algorithms for certain measurement conditions is presented. The experiments demonstrate the advantage of 3D Compton imaging over traditional localization techniques in those scenarios. Improvements in time encoded imaging (TEI) were also made with advancements in the reconstruction algorithms and was done so in three thrusts: use of subpixel sensing, depth of interaction correction, and 3D imaging of extended sources. Complex 3D objects was accomplished via the use of magnification-parallax effects which allowed for the estimation of a source in distance away from the detector. Both the 3D Compton imaging and TEI techniques were explored at the Idaho National Laboratory.

CHAPTER I

Introduction

Radiation and its usages can sometimes be a scary phenomena. In most cases, it cannot be seen, smelled, or felt by the human senses, making it impossible to identify. Therefore, tools and instruments have been developed to assist the user with measurements of such events. Compton gamma-ray imaging, which is the main subject in this dissertation, is one of those vital tools that has a multitude of applications in fields ranging from astronomy [1], through medicine [2], to nuclear security [3].

1.1 Gamma Rays

Radiation is the emission of energy in the form of an electromagnetic wave or a subatomic particle [4]. The main topic in this section will revolve around gamma (γ) rays, a 'high-energy' photon with a very short wavelength. It usually arises from the decay of nuclei, but can be produced via other exotic means. It was discovered by Paul Ulrich Villard, a French chemist, in 1900 when he studied the radiation emitted from radium. In Villard's investigation, he noticed that some radiation was more penetrating than alpha (α) particles, which were discovered a year before by Ernest Rutherford [5]. Moreover, they were not deflected by a magnetic field as the beta (β) particles were, implying the discovery of a new neutral particle [6].

The manner in which gammas, or rather photons in general, interacted with matter

was still unclear in the first years of the 20th century. It was known that a photon, over a certain energy threshold, would eject an electron when interacting with matter [7]. It was not until 1905 that Albert Einstein described light as a quantized packet [8], which awarded him the 1921 Nobel Prize in Physics.

The dual particle nature of the photon was further confirmed with Arthur Compton's observations of a wavelength shift of a photon that has scattered [9]. The wavelength change observed was as follows:

$$\lambda' - \lambda = \frac{h}{m_e c}(1 - \cos\Phi), \tag{1.1}$$

where λ and λ' represent the wavelegnth before and after the interaction, h is Planck's constant, m_e is the electron rest mass, c is the speed of light, and Φ is the scattering angle. This discovery, which was later named Compton scattering, led him to win the 1927 Nobel Prize in Physics.

It would be almost another decade until pair-production, the creation of an electron-positron pair from a photon ($\gamma \rightarrow e^- + e^+$), was fully realized. It was through observations by Chadwick, Blackett, and Occhialini with a cloud chamber [10], for which Blackett won the 1948 Nobel Prize in Physics, that pair-production was fully realized. They noticed that some gamma rays would produce an electron and a equivalent anti-particle, which they called 'positive electrons'[1] [11].

1.2 The University of Michigan OrionUM Digital Detector System

The current University of Michigan 4π imaging-spectrometer, named OrionUM, employs an array of $2 \times 2 \times 1.5$ cm^3 CdZnTe crystals (Fig. 1.1) arranged in a 3×3 configuration. Each module consists of an 11×11 pixelated anode and a planar cathode which can perform high-resolution spectroscopy and real-time Compton imaging [12].

[1]Note that positrons were observed over a decade earlier by Chung-Yao Chao and the 1936 Nobel Prize was given to Carl David Anderson for the discovery.

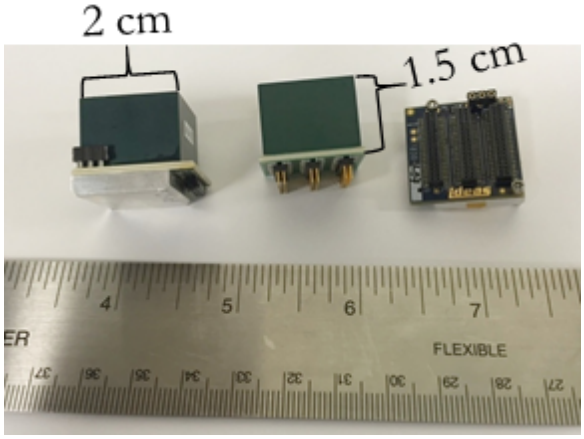

Figure 1.1: The leftmost object presents a 'direct-attached' CdZnTe crystal where it is attached directly to the application-specific integrated circuit (ASIC). The center object is a 'standard' attached detector which is then connected to an interposer which facilitates the mating with the ASIC (the rightmost object).

These detectors can provide the positions of interactions with a spatial resolution of 500 nm for a 120 keV interaction and 300 nm for a 662 keV event [13]. Fig. 1.2 plots the sub-pixel interaction map in two energy ranges.

The OrionUM system has an energy resolution of about 0.35% full width at half max (FWHM) at 662 keV using single-pixel events, and about 0.5% FWHM for all events, operated at room temperature. Fig 1.3 plots a Cs-137 spectrum using the OrionUM system.

The cross section, or probability, of each interaction varies for different materials (Z). Fig. 1.4 plots the cross-sections for the different interaction mechanism with $Cd_{90}Zn_{10}Te_{100}$. It can be seen that photoelectric absorption is the dominant interaction until about 250 keV and is when Compton scattering becomes the main mode of interaction. Pair-production becomes the dominant gamma-matter interaction above 6.4 MeV.

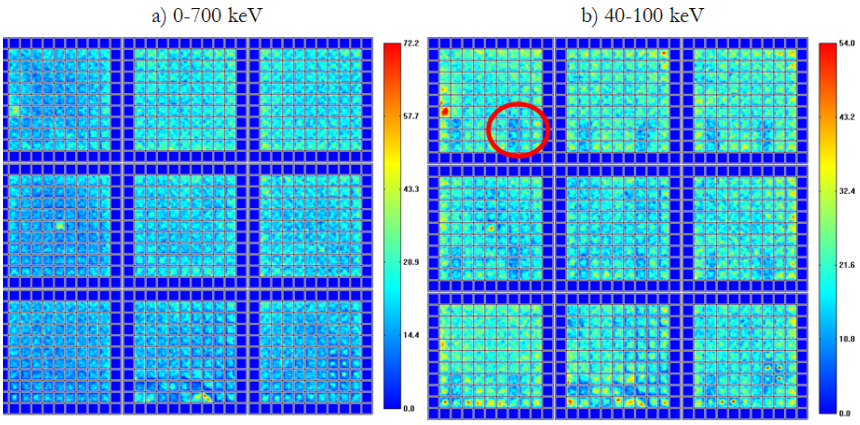

Figure 1.2: Plotted are the subpixel distributions for a Ba-133 and Cs-137 measurement. a) Presents the distribution for an energy range of $0 - 700\ keV$ while b) plots it for a $40 - 100\ keV$ range. The edge pixels are not presented as subpixel estimation for edge pixels was not implemented at the time. Note the red circle encompasses the shadow of a capacitor placed on the bias distribution board above the cathode.

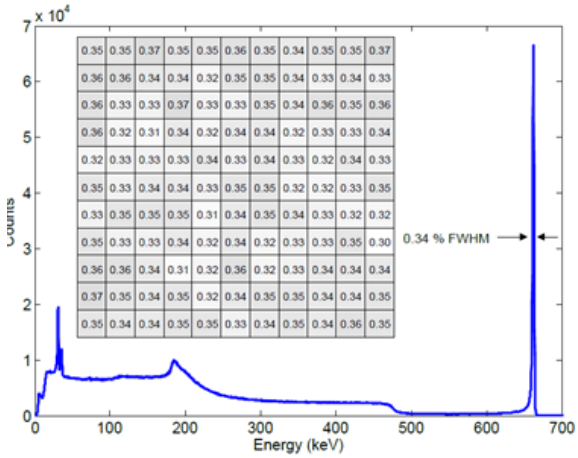

Figure 1.3: Cs-137 spectrum of OrionUM-Beta. Courtesy of Dr. Yuefeng Zhu.

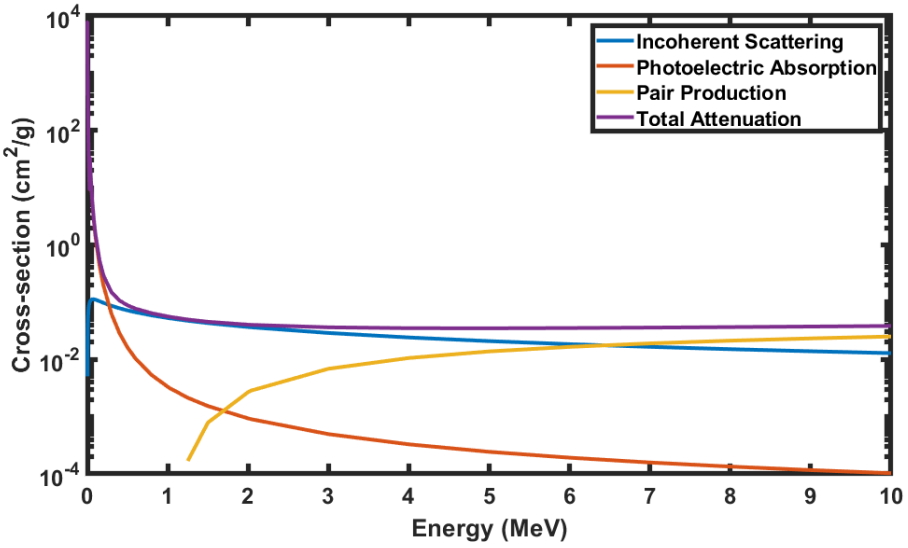

Figure 1.4: Different gamma-matter interaction cross sections for $Cd_{90}Zn_{10}Te_{100}$.

1.3 Objectives and Overview of This Work

The main focus of this work revolves around Compton imaging of super-MeV gamma rays, specifically 1-5 MeV. This work offers improvements and additional analysis for these high-energy gamma rays as their characteristics slightly differ. Chap. III examines the artifacts associated with high-energy gamma rays. Through that analysis, several mitigation techniques are offered to remove pair-production and missequenced events by analyzing the distribution of scattered events. Another technique is via the application of the FIL-MSD sequencing algorithm, which was developed during the course of this work and presented in Chap. IV. The new algorithm has increased the sequencing efficiency by $\sim 20\%$ which resulted in a two-fold SNR increase for 3-or-more interaction events using simple backprojection. The high-energy work culminates with a derivation of an analytical point spread function that is used for filtered backprojection (FBP).

The other projects, referred to in the title of this dissertation, summarizes what Prof. Zhong He describes as the 10% work. This work, although still relevant to the

main topic at hand[2], should be something different. What is chosen in this manuscript is work on 3D gamma-ray imaging and advancements in the time encoded imaging (TEI) system. This work on 3D imaging, although accomplished by the Orion group in previous years, presents a different approach to estimating pose of the detector. It makes use of an inertial measurement unit (IMU) to estimate pose rather than using computer vision/SLAM based techniques and is discussed in Chap. VII. TEI was improved upon by implementing the sub-pixel of the system further pushing the capabilities of the system. The work also adds a dimension to TEI by estimating the 3D source distribution of special nuclear material. The work on TEI is summarized in Chap. VIII.

[2]which is anything that involves pixelated CdZnTe

CHAPTER II

Gamma-Ray Imaging Using Pixelated CdZnTe

Compton imaging requires knowledge of the gamma ray interaction's locations and deposited energies, the order of which are sequenced, the locus of points where the gamma ray could have originated from reconstructed, and then backprojected to estimate the direction of the incident gamma ray. It was first proposed by [1]. With 3D-position-sensitive detectors, both the position ($\mathbf{r}_i$) and energy deposited (E_i) of the ith interaction in the event are recorded.

Fig. 2.1 sketches the 3×3 crystal OrionUM detector, which is the detector used thorough this manuscript. In the schematic, the norm of the cathode is in the $\hat{y}$ direction and the source is located at coordinate (ϕ, θ).

When a gamma ray with energy E_{O} enters the detector, it commonly interacts through the following modes: photoelectric absorption, Compton scattering, or pair production. If the photon scatters first and interacts a total of two or more times, the line between the first two interaction locations creates the axis of the Compton cone with an opening angle derived from the Compton scattering formula. The Compton cone represents the possible directions from which the incident photon originated. The opening angle (Φ) is represented by:

$$\cos(\Phi) = 1 - \frac{m_e c^2 E_A}{E_O(E_O - E_A)}, \tag{2.1}$$

where E_{A} is the deposited energy in the first interaction, the electron rest energy is

represented by $m_e c^2$, and the incident energy E_0 is either known a priori or assumed to be the summation of the observed interactions. Imaging events that did not undergo full energy deposition will result in an incorrect cone opening angle and image artifacts [14]. Full energy peaks are commonly imaged as they have a large probability of full energy deposition. Therefore, partial energy depositions were not included in these studies.

The Compton cone is then backprojected onto an image sphere, which intersects it along a ring known as a Compton ring. Combining multiple Compton rings estimates the direction of the emitting source[1].

In detectors where poor timing resolution prevents the temporal sequencing of interactions, "sequence reconstruction", or "gamma-ray tracking", algorithms must be implemented to sequence events [15]. This is required for CZT as the timing resolution for the system is quoted as 10 ns and in that time, the scattered photon could have traveled almost 3 meters[2]. This concept will be further discussed in Chap. IV.

This chapter aims to summarize the imaging modalities commonly applied with the University of Michigan OrionUM pixelated CdZnTe detector.

2.1 General Model for Imaging

A general model for imaging can be made as follows:

$$\bar{\mathbf{y}} = \mathbf{T}\mathbf{f}, \tag{2.2}$$

where $\mathbf{f}$ is the true source vector of length J that is being measured, $\bar{\mathbf{y}}$ is the expected observation vector of length I, and $\mathbf{T}$ is an $I \times J$ sized system matrix. The entries of each element will depend on how the system is defined, i.e. is it reflecting activity or some normalized intensities. The jth entry of each element of $\mathbf{f}$ can denote an

[1]Note that the imaging space need not necessarily be a sphere. In standard far-field 4π imaging, we approximate the center of the detector to be the origin of the cone which is then backprojected to an image space which is modeled as a sphere. However, in near field application spaces, depending what is known a priori, the image space can be planar or a volumetric voxelated cube.

[2]Speed of light is about a foot (0.3 meters) per nanosecond.

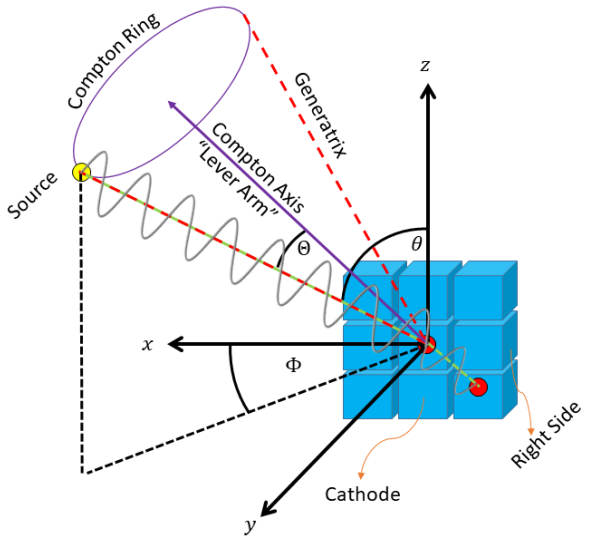

Figure 2.1: Sketch of the $3 \times 3 \times 1$ OrionUM CdZnTe system where the array is placed in the $x - z$ plane. The yellow circle represents a source which emits a gamma ray (grey), which Compton scatters off the upper-left red circle and photoabsorbs in the lower-right red circle. A Compton cone (red) with opening angle of Θ is backprojected onto a spherical image space which intersects it in what is known as a Compton ring (purple). The cathode plane has a normal vector of $\hat{y}$ and the anode plane has a normal vector of $-\hat{y}$.

intensity or activity in j, while $\bar{\mathbf{y}}$'s entries will consist of detected counts or detection efficiency.

$$\mathbf{T} = \begin{bmatrix} p_{11} & \cdots & p_{1j} & \cdots & p_{1J} \\ \vdots & \ddots & \vdots & & \vdots \\ \vdots & & p_{ij} & & \vdots \\ \vdots & & \vdots & \ddots & \vdots \\ p_{I1} & \cdots & p_{Ij} & \cdots & p_{IJ} \end{bmatrix}, \tag{2.3}$$

where each jth column is a single detection bin that has characteristics:

$$i \rightarrow \left\{ E_1, \ldots, E_N, \vec{\mathbf{R}}_1, \ldots, \vec{\mathbf{R}}_N \right\} \tag{2.4}$$

with E_n representing the nth energy deposition in the $\vec{\mathbf{R}}_n$ location of N total interactions. Each element (p_{ij}) in the matrix represents the probability a gamma ray originated from location j and was detected as i. The structure of $\mathbf{T}$ implies that each row is a Compton cone in the image space. Therefore, $\mathbf{T}$ is a very large matrix as there is a huge number of possible interaction permutations a gamma ray can undertake

while being attenuated in the detector. In other words, I is very large. We therefore result to list mode reconstruction techniques to simplify the reconstruction process rather than some 'binned' matrix.

There exist several reconstruction methods, with 'inverse' and 'iterative' techniques presenting the two main categories. Inverse techniques, which mainly consist of 'Simple Backprojection' (SBP) and 'Filtered Backprojection' (FBP), are discussed in Sec. 2.2. These algorithms are considered to be very fast and computationally cheap. Iterative reconstruction algorithms, however, rely on a multiple step process to converge on the solution and might result in a better reconstruction, but at a high computational cost. They are discussed in Sec. 2.3.

2.2 Inverse Reconstruction Algorithms

2.2.1 Simple Backprojection

The simple backprojection (SBP) process can be modeled as:

$$\hat{\mathbf{f}}_{sbp} = \mathbf{T}^t\mathbf{y} = \mathbf{T}^t\mathbf{T}\mathbf{f} = \mathbf{B}\mathbf{f}, \tag{2.5}$$

where $\mathbf{B}$ is a matrix of point spread functions. However, in the Orion group CZT, this estimator is biased, and does not provide a shift-invariant[3] solution because $\mathbf{T}^t\mathbf{T} = \mathbf{B} \neq \mathbf{I}$, where the jth column is the PSF of for a source located in the jth image pixel[4]. $\mathbf{I}$ is an identity matrix.

In simple backprojection, we generally normalize the rings. The effect of this process can be seen in Fig. 2.2. Events with smaller scatter angles are "weighted more" and appear to be brighter because each rings is normalized to 1. This means that each row in $\mathbf{T}$ is normalized to its sum. Therefore, each element along the Compton

[3]A system $H(x)$ will be shift invariant if $H(x(t)) = y(t)$ and $H(x(t+\tau)) = y(t+\tau)$ both hold true. In words, if an input is shifted in time, then the output will be shifted by the same amount.

[4]For $\hat{\mathbf{f}}_{sbp}$ to be unbiased estimator of $\mathbf{f}$, $\mathbf{B}$ will have to be an identity matrix such that $\hat{\mathbf{f}}_{sbp} = \mathbf{B}\mathbf{f} = \mathbf{f}$. The mathematical definition of bias is $\text{Bias}[\hat{\mathbf{f}}] = \mathbf{E}_{y|f}[\hat{f} - f]$ and will be 0 for an unbiased system [16].

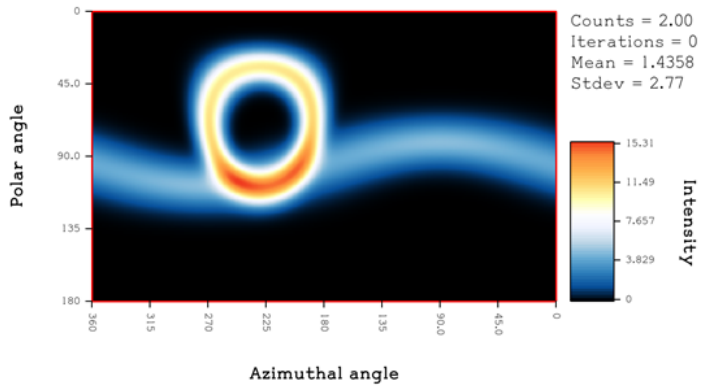

Figure 2.2: Two projected Compton cones each normalized to 1. Note that the cone with the larger opening angle appears dimmer than the cone with the smaller opening angle.

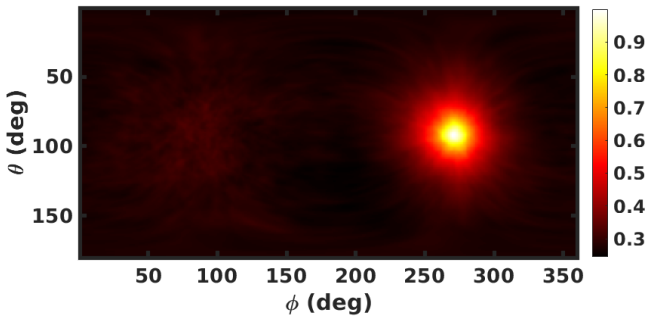

Figure 2.3: SBP image using experimental data of a ^{228}Th source consisting of only 15882 3-pixel events.

ring, or a row in $\mathbf{T}$, is worth $\frac{1}{\sin(\Phi)}$ and the following holds true[5]:

$$\int_{\Omega} g_{i_1}(\vec{\Omega})\mathrm{d}\vec{\Omega} = \int_{\Omega} g_{i_2}(\vec{\Omega})\mathrm{d}\vec{\Omega} = 1, \tag{2.6}$$

where $g_{i_1}(\vec{\Omega})$ represents the ith row in $\mathbf{T}$. Generally, simple backprojection, although fast and simple, results in a poor image and is often quoted to have a FWHM resolution of about 30°. Fig. 2.3 presents an SBP image from an experimental measurement exhibiting the limited performance.

[5]This is against the traditional definition of SBP ($\hat{\mathbf{f}}_{sbp} = \mathbf{Bf}$) as there is a normalization applied to $\mathbf{B}$. However, it is my opinion that since SBP is already biased and 'simple' in nature, we can augment (bias) the system with carefully chosen parameters to give us a sharper image, or one with better signal to noise. This does not hold true for advanced image processing techniques such as MLEM, FBP, or SOE.

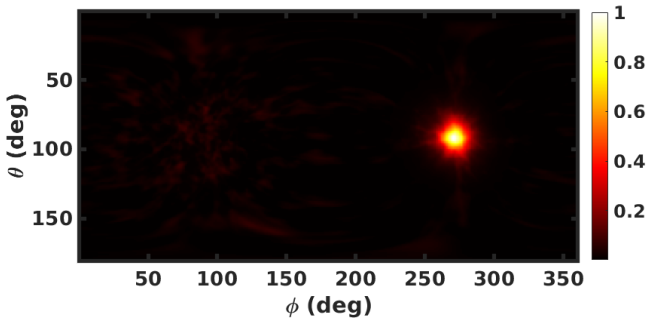

Figure 2.4: FBP image using experimental data of a ^{228}Th source consisting of only 15882 3-pixel events.

2.2.2 Filtered Backprojection

Filtered backprojection, or FBP, presents a computationally cheap alternative to SBP to provide a high resolution image [17]. It is designed to recover a signal by removing the blur introduced by the system [18]. However, it remains a challenge to design a filter with an appropriate point spread function model. The simplest filter is perhaps the inverse filter. Using the model described in (2.5), we can filter the SBP image as such:

$$\hat{\mathbf{f}}_{\text{fbp}} = \mathbf{B}^{-1}\hat{\mathbf{f}}_{\text{sbp}} = \mathbf{B}^{-1}\mathbf{T}^{\mathbf{t}}\mathbf{y} = \mathbf{B}^{-\mathbf{1}}\mathbf{T}^{\mathbf{t}}\mathbf{T}\mathbf{f} = \mathbf{f}, \tag{2.7}$$

where $\mathbf{B} = \mathbf{T}^{\mathbf{t}}\mathbf{T}$ and represents the $J \times J$ point spread function (PSF) matrix of the system. In practice, filtering with $\mathbf{B}^{-1}$ could develop significant noise when $\mathbf{B}$ has very small values. Therefore, an advanced filter is required to perform a more practical reconstruction. One filter, which will be the base filter of the work in Chap. VI, is the Weiner filter, which is designed to minimize the mean square error during the inversion process [19]. Fig. 2.4 presents a filtered image of the same data used to create Fig. 2.3 and has a FWHM resolution of 15°.

2.3 Iterative Reconstruction

Iterative algorithms, specifically maximum likelihood based techniques, are perhaps the more popular methods among the Compton-imaging community. The following have been explored in in the Orion group: Maximum Likelihood Expectation Maximization (MLEM) [20], Stochastic Origin Ensemble (SOE) [21], Ordered Subset Expection Maximization [22, 23], Energy-Imaging Integrated Deconvolution (EIID) [24] and later Energy Decremental Integrated Deconvolution (EDID) [14]. Another common algorithm, although not implemented in the Orion group, is Maximum Entropy estimation based techniques, which is more often used in astronomy [25].

Although iterative algorithms may provide higher resolution images, they are often computationally expensive, in both memory and speed [26]. To apply the necessary iterations, the system matrix must be held in memory, or recreated and then discarded every iteration. In addition, Compton imaging relies on list-mode techniques where the system matrix is created on-the-fly. The analytical model takes the form similar to what Wilderman et al. developed [27], but with some additional terms [22]. The current model [22], however, is lacking terms that are difficult to include, such as the probability of the escape of scattered gamma rays due to detector geometry.

2.3.1 Maximum Likelihood Expectation Maximization

Perhaps the most popular iterative techniques involve maximum likelihood (ML) estimations, a form of statistical inference [28]. The goal in ML estimations is to evaluate some parameters of a distribution (i.e. source distribution $\mathbf{f}$) by maximizing the likelihood function.

The principle ideology of ML estimation is to make an inference about the population given a sample measurement. From our generic imaging model, the measured sample is $\mathbf{y} = \{y_1, y_2, \ldots, y_N\}$ from some distribution $\mathbf{f}$ and the goal is to estimate

the source's distribution ($\hat{\mathbf{f}}_{ML}$), given the measurement $\mathbf{y}$:

$$\hat{\mathbf{f}}_{\mathrm{ML}} = \mathrm{argmax}_{\mathbf{f}}\ L(\mathbf{y}|\mathbf{f}) \tag{2.8}$$

where L represents the likelihood. In radiation detection, we can safely assume Poisson observations and therefore model the likelihood function as the joint probability of the sampled data:

$$\begin{aligned} L(\mathbf{f}) &= p(y_1|\mathbf{f})p(y_2|\mathbf{f})\dots p(y_N|\mathbf{f}) \\ &= \prod_{i=1}^{N} p(y_i|f). \end{aligned} \tag{2.9}$$

One way to find the ML estimate, or the maximum of the likelihood function, is by taking the first derivative and equating it to zero ($\frac{\mathrm{d}L}{\mathrm{d}\mathbf{f}} = 0$). However, taking the derivative of (2.9) can prove to be quite challenging. Therefore, we take the derivative of the log of the likelihood function, also called the log-likelihood, to simplify the maximization process. This is done as follows:

$$\begin{aligned} \mathcal{L}(\mathbf{f}) &= \ln L(\mathbf{f}) \\ &= \ln \prod_{i=1}^{N} p(y_i|\mathbf{f}) \\ &= \sum_{i=}^{N} \ln p(y_i|\mathbf{f}). \end{aligned} \tag{2.10}$$

Not only is the definition now simpler, but computation of the log-likelihood is simpler. There are several techniques to find the maximum of the log-likelihood, but the one we present here is expectation-maximization (EM).

EM is an iterative algorithm that is used to find the local maximum likelihood [29]. Its derivation can be found in Dr. Jiyang Chu's dissertation Sec. 4.1.2-4.1.3 [14]. Nevertheless, the bin mode MLEM algorithm is formulated as follows:

$$f_j^{k+1} = \frac{f_j^k}{s_j} \sum_{i=1}^{N} \frac{t_{ij}}{\bar{y}_i^k} \tag{2.11}$$

where j and i are the pixel and detection bin index, k is the iteration number, and the t_{ij} is known as the system matrix for bin i in image pixel j. The sensitivity of the detector is represented by s_j, which basically represents the probability of detecting a gamma ray if it were to originate from pixel j. It is formulated as the summation of

the system matrix for a given image pixel:

$$s_j = \sum_{i=1}^{N} t_{ij}. \tag{2.12}$$

As discussed in Sec. 2.1, the number of detection bins (I) is quite large. Therefore, we resort to list-mode analytical methods that create the system matrix for each event:

$$t_{ij} = e^{-\frac{(\Theta_i - \theta_j)^2}{2\sigma_i^2}} \prod_{K=1}^{N_{\text{interactions}}} \frac{\mathrm{d}\sigma(\Theta_i)}{\mathrm{d}\Omega} e^{-\mu(\mathbf{r}_{k+1} - \mathbf{r}_k)}. \tag{2.13}$$

The first element Gaussian blurs the ring with standard deviation σ_i. The terms that affect the blur include position and energy uncertainty. Next, in the product, the interaction cross section and the attenuation probabilities are calculated to weight the ring by the probability of the event occurring[6]. The final list-mode MLEM algorithm is available in (2.14).

$$f_j^{k+1} = \frac{f_j^k}{s_j} \sum_{i=1}^{N} \frac{t_{ij}}{\sum_{j'=1}^{J} t_{ij'} f_{j'}^k}. \tag{2.14}$$

The appropriate number of iterations required is dependent on factors such as statistics, size, shape, and distribution of the source, and other parameters. However, as a rule of thumb, 20 iterations tend to be appropriate for a point source with the Michigan CdZnTe system. It is worth noting that MLEM is considered an asymptotically unbiased estimator under certain regularity conditions [30]. However, generally the system model or the limited amount of statistics prevents one from reaching the asymptote. Fig. 2.5 presents the MLEM image that uses the same data shown in the previous section. This technique has a resolution of around 5° [22].

2.4 Coded Aperture Imaging

Coded aperture imaging is a more complex form of a pinhole camera. In a pinhole camera, a single aperture is placed between a light source and a detector. Light can therefore only pass through the aperture and an image is projected onto the detection plane. The amount of light that passes is naturally dependant on the size of the aperture. However, with an increased aperture size, the projection will become more

[6] In CdZnTe, we project all the possible sequences

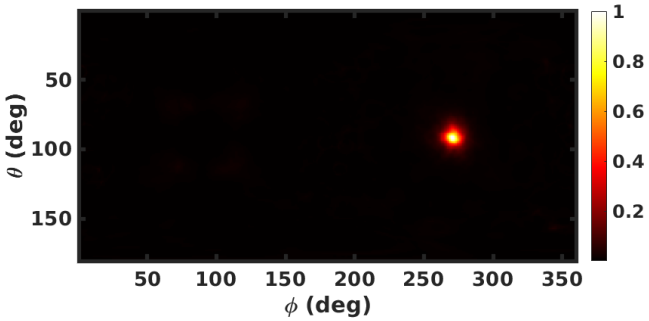

Figure 2.5: MLEM image using experimental data of a ^{228}Th source consisting of only 15882 3-pixel events. This reconstruction applied 15 iterations.

blurred. Therefore, the selection of the pinhole size has a large effect on the image due to the trade off of image resolution and projection intensity.

Another method of maintaining the image resolution without the loss of signal is to create multiple pinholes. With multiple apertures, a whole suite of projections are accumulated on the detection plane. A mathematical model of the observation matrix can be formulated as follows:

$$\mathbf{O} = \mathbf{F} * \mathbf{A} * \mathbf{D} + \mathbf{B}, \tag{2.15}$$

where $\mathbf{O}$ is the observation matrix, $\mathbf{F}$ is the source distribution, $\mathbf{A}$ is the mask transmission matrix, $\mathbf{D}$ is the detector response term, and $\mathbf{B}$ is the noise term. The mathematical operation $(*)$ represents a convolution operator. Correlation with a decoding function $(\mathbf{G})$ presents one of the more popular reconstruction techniques [31]:

$$\hat{\mathbf{F}} = \mathbf{O} \circledast \mathbf{G}, \tag{2.16}$$

with $\hat{\mathbf{F}}$ representing the estimated source distribution and $\circledast$ symbolizing the periodic cross-correlation operator. $(\mathbf{G})$ is chosen such that $\mathbf{G} * \mathbf{A} = \delta$. There exists a whole family of masks $\mathbf{A}$, including uniform redundant array (URA), hexagonal URA, Modified URA, and a random mask. The most popular patterns in the Orion group are MURAs as they are notable for their mask anti-mask symmetries [31]. The number of mask elements (rank) and pixel pitch should vary with different detector sizes and application spaces. Regardless of which mask is used, each source location should

project a unique mask projection vacant of degeneracy.

2.4.1 Time Encoded Imaging

Time-encoded imaging (TEI) is an extension of coded aperture imaging, in that it uses a coded aperture to spatially encode the source, but also contains a temporal encoding [32–34]. Several advantages exist. For one, the entire mask need not be recorded all at once. In traditional coded aperture, any mask element not recorded will distort the reconstruction. In the CZT detector family, there exists a some spacing between each detector module due to the design of the system. Those gaps translate to artifacts in the image in the form of a pound (#) or hash symbol [21, 33]. This also implies that a larger magnification could be applied which reduces the distortion by $\mathbf{D}$ in (2.15).

The current TEI system is named 'Mira' and was the main dissertation work of Dr. Steven Brown [33, 34]. It has two stepper motors to translate the mask horizontally and vertically in a manner such that the detector is in the umbra of the coded shadow. Figure 2.6 depicts the imaging detector system. The detector is mounted on an assembly that is held by two rails on which it can slide to vary the mask-to-detector distance. The current maximum mask-to-detector distance is 59 cm.

The coded mask is attached at the end of the horizontal arm. The mask itself is made of layered tungsten sheets, each 0.25 mm thick. The mask is a rank 79 modified uniformly redundant array (MURA) [31] with a total of 200×200 elements for a total size of 12 in $\times$ 12 in. The MURA pattern is repeated 2.53 times. Each element, or pixel pitch, is 1.4 mm wide. In this study, 4 mask sheets were used together totaling 1 mm of thickness as an optimized option for the trade-off between attenuation and collimation effects of thicker masks.

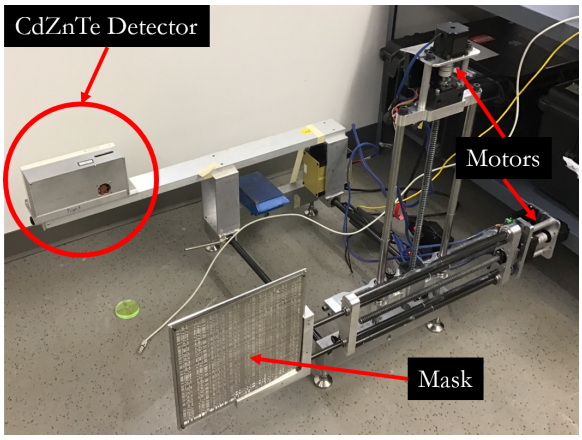

Figure 2.6: The OrionUM CdZnTe detector attached to the Mira system with the tungsten coded mask and the stepper motors labeled.

2.5 System Limitations for Imaging

Perhaps the major degradation to the image quality is the position resolution of the system, given that the system already has a good energy resolution performance [35]. Drs. Zhu and Wang, and Chap. VIII in this manuscript, have shown how the addition of sub-pixel information has improved the images, but there is still room for improvement. The task of increasing the position resolution will be complicated with the increased electron cloud size for higher energies. The increase in electron clouds also presents an opportunity for electron tracking. Tracking of the electron cloud will allow for the addition of kinematic knowledge into the reconstruction which will constrict the Compton cone to an arc.

Timing resolution is also quite low when compared to scintillator-based detectors [4]. Timing resolution is especially important for high flux applications such as proton therapy. There, the prompt gamma rays induced by protons are of interest and sit on a large background of neutron-induced gamma-ray background. In a recent study, it was declared that a 1.25 ns window was required to separate the neutron and proton-induced gammas [36].

Finally, the efficiency of the system is also of concern for higher energies. The

probability of detection, and imaging efficiency following that, are quite low, and decrease for larger energies. The low detector volume is also quite limiting for high energy applications.

CHAPTER III

Artifacts in High Energy Gamma-Ray Imaging

High energy gamma-ray imaging is an important technique with applications in homeland security and medical imaging. Recent advancements in the Cadmium Zinc Telluride (CdZnTe) OrionUM detector systems have enabled measurement of gamma-ray sources with energies up to 9 MeV. However, Compton imaging of photons above 3 MeV faces several challenges that degrade both spectroscopic and imaging performances in pixelated CdZnTe systems. These factors include the increase in pair-production events, incorrect event sequencing, and charge sharing from large electron clouds. They all result in shift-variant image artifacts that degrade the signal-to-noise ratio as well as create artifacts that might be mistaken for a hot spot. The degradation from artifacts is analyzed, discussed, and possible mitigation techniques are presented to allow for recovery of the Compton image signal. Simulation is compared with experimental measurements of 4.4 MeV gamma rays from a ^{238}PuBe source to investigate the artifacts.

3.1 Introduction

High energy gamma-ray detection, which is defined as any gamma ray above 3 MeV in this study, is used for active interrogation of special nuclear material (SNM) with the

Based on accepted published work: D. Shy, J. Xia, and Z. He, "Artifacts in High-Energy Compton Imaging with 3D Position Sensitive CdZnTe," IEEE Transactions of Nuclear Science

energy range of interest between 2.5 and 6 MeV [37]. Detection of high explosives also employ active interrogation with neutrons by measuring the de-excitation of nitrogen instigated by the thermal capture on the nitrogen $\{^{14}\mathrm{N}(n,\gamma)^{15}\mathrm{N}^*\}$ with the emission of several gamma rays ranging from 4.48 to 10.82 MeV [38]. In nuclear medicine, 4.4 and 6.1 MeV gamma rays, from the de-excitation of $^{12}\mathrm{C}^*$ and $^{16}\mathrm{O}^*$ respectively, are used to verify the range of the proton beam in proton therapy [2].

With 3D position sensitive detectors, such as a pixelated CdZnTe, both the position ($\mathbf{r}_i$) and energy deposited (E_i) of the i^{th} interaction in the sequence of the measured multi-interaction event can be recorded. This information allows for backprojection of a Compton cone to estimate the direction of the incident gamma ray, which is known as simple backprojection (SBP) imaging. For Compton imaging, the photon must interact at least twice. The vector created from the second to the first interaction location creates the "Compton axis", or "lever arm", and with that, a cone is created with an opening angle derived from the Compton scattering formula, and is illustrated in Fig. 3.1. The opening angle (Θ) between the lever arm and generatrix is represented by:

$$\cos(\Theta) = 1 - \frac{m_e c^2 E_1}{E_0(E_0 - E_1)}, \tag{3.1}$$

where the electron rest energy is represented by $m_e c^2$, E_1 is the deposited energy in the first interaction, and the incident energy, E_0, is either known *a priori* or assumed to be the summation of the observed interactions. Superimposing multiple Compton cones reveals the estimated source location.

Compton scattering interactions, followed by a photoelectric absorption, form the basis of Compton imaging. Pair-production, however, does not preserve directional information unless the trajectory of the electron and positron can be tracked [39], which currently cannot be accomplished with the OrionUM detector system. Therefore, events with pair production as the first interaction cannot be used for imaging.

This work explores image artifacts associated with Compton imaging high-energy

gamma rays, which can originate from either charge sharing, pair-production, or incorrectly sequenced events. Image artifacts are important to identify as they are errors in the image not present in the original object. They are a misrepresentation of information as they are false image structures, thereby degrading the analysis especially when no *a priori* knowledge is known. These artifacts can apply to other Compton imaging systems that are semiconductor or scintillator based. This manuscript also presents several techniques to mitigate some of the symptoms.

3.2 Overview of Terminology, Methods, and Experimental Setup

3.2.1 Terminology and Coordinate System

An "interaction" describes a single gamma-ray interaction, while an "event" refers to a collection of interactions that originated from a single incident gamma ray. The number of "pixel events" refers to the number of anode pixels triggered in an event. Therefore, the number of pixel events may not match the number of interactions due to the pixelated nature of the detector. A "side-neighbouring event" refers to any event where two recorded pixel-interactions occur in adjacent pixels. This could be a result of a gamma ray that scattered into the neighbouring pixel, or a "charge sharing" event where a single interaction produced an electron cloud that is collected by multiple anode pixels.

Fig. 3.1 sketches the 3×3 crystal OrionUM detector with a coordinate system that is consistent throughout this chapter. In the schematic, the normal of the cathode is in the $\hat{y}$ direction and the source is located in coordinate (ϕ, θ). Additional detail on the OrionUM system is available in Sec. 3.2.2.

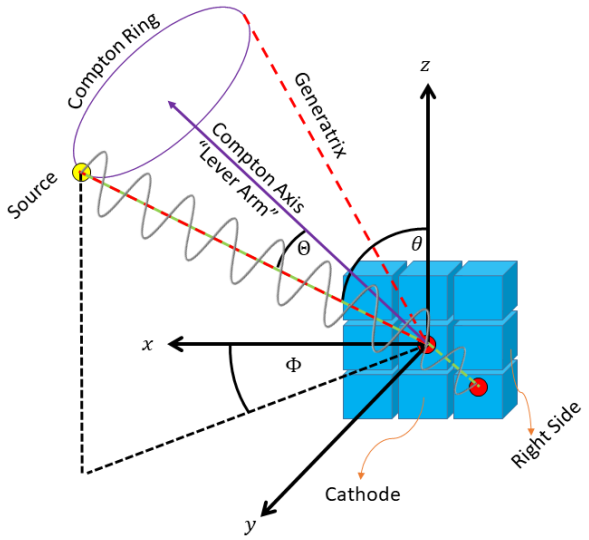

Figure 3.1: Sketch of the $3 \times 3 \times 1$ OrionUM CdZnTe system where the array is placed in the $x - z$ plane. The yellow circle represents a source which emits a gamma ray (grey), then Compton scatters off the red circle and photoabsorbs in the next location. A Compton cone (red) with opening angle of Θ is backprojected onto a spherical image space which intersects it in what is known as a Compton ring (purple). The cathode plane has a normal vector of $\hat{y}$ and the anode plane has a normal vector of $-\hat{y}$.

3.2.2 Simulation of the Electron Cloud in CdZnTe

The simulation package was used in [40], which features a description of the GEANT4 simulation configuration. The simulation model also took electron thermalization into consideration and the track of the electron recorded. Therefore, a single interaction could trigger multiple pixels if an electron travels into other pixel regions. The physics libraries implemented are pair-production, Compton Scattering, photoelectric effect, all from the Livermore low energy physics package as well as electron-matter interaction libraries [41].

Fig. 3.2 presents the electron cloud size as a function of deposited energy as simulated in GEANT4 by tracking the electron after a gamma-ray interaction. In this study, electron cloud diameter was defined as the largest separation between two ionized electrons produced along the thermalization of the recoiled electron [42]. The horizontal dashed blue line represents the pixel pitch. The average electron cloud size

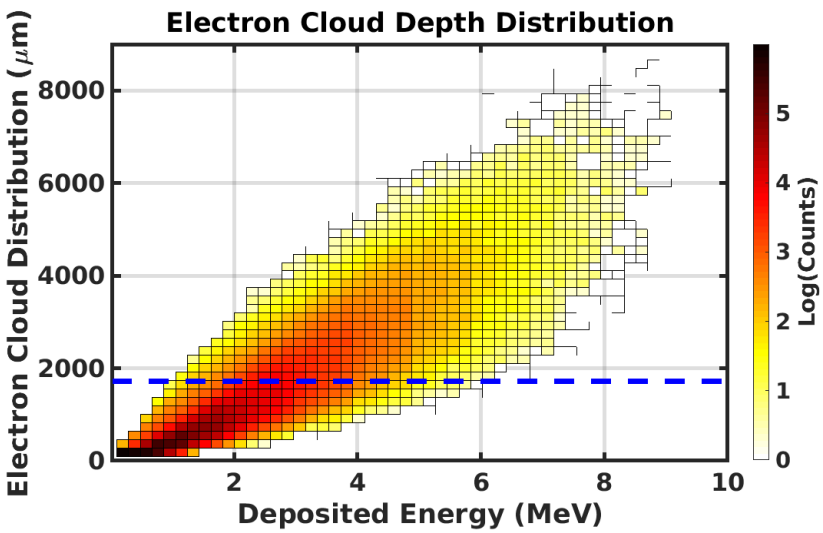

Figure 3.2: Simulated electron cloud size as a function of deposited energy. The pixel pitch is represented by the horizontal dashed blue line at 1720 μm.

at 511 keV is about 220 μm while a 2 MeV event results in 1180 μm cloud. The energy where the electron cloud is the size of the pixel pitch is about 2.75 MeV. The mean free path of a 511 keV photon in CdZnTe is about 2.2 cm, which includes scattering and photoelectric cross section.

3.2.3 Sequence Reconstruction of Gamma-ray Interactions

Interactions in an event must be sequenced before any image reconstruction can take place in CdZnTe due to its poor time resolution. The specific sequencing algorithm implemented depends on the number of observed interactions in an event.

For two-pixel events, the applied sequencing method is known as simple comparison, which compares the energies of each interaction with the Compton edge and amongst themselves [26]. Three-or-more pixel events are sequenced with the "Mean Squared Difference" method [22, 43], where each possible permutation is assigned a figure-of-merit (FOM), and the sequence with highest FOM is selected. Unless stated otherwise 'Simple Comparison' and 'MSD' are the two algorithms used in the study.

The final sequencing algorithm investigated, also for three-or-more interaction

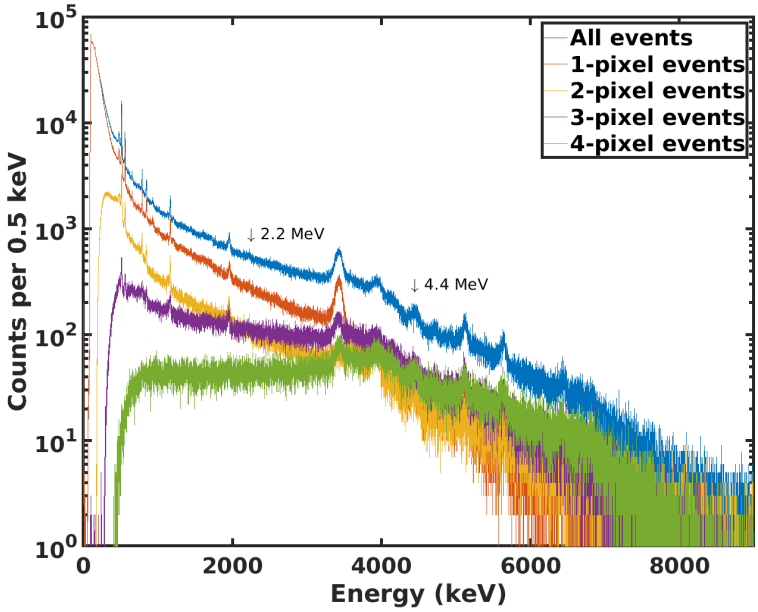

Figure 3.3: Gamma-ray spectrum of a PuBe source in a PVC target for the different number of interactions. The data corresponds to the cathode irradiation discussed in Sec. 3.2.4.

events, is "FIL-MSD" (First Is Largest/FIL), which uses the same permutation-FOM technique as MSD [40]. However, the first interaction is fixed to be the largest energy deposited interaction in the event. This algorithm proved to be more effective than MSD for energies above 1 MeV range and will be discussed in Sec. 3.5.3 as possible artifact mitigation techniques.

3.2.4 Experimental Setup and Image Artifacts in High Energy Gamma-ray Imaging

Fig. 3.3 shows a gamma-ray spectrum using the OrionUM system for a PuBe source in a polyvinyl chloride (PVC) target. The PVC was placed in order to produce higher energy gamma rays from the neutron capture on ^{35}Cl, which were not used in this study, but added noise in the image through its continuum. Two measurements were completed, one cathode irradiation and one left side irradiation where the source was placed in the $+\hat{x}$.

The artifacts associated with high-energy gamma-ray imaging are of interest as they are shift variant and shape invariant. In other words, the artifact locations do not shift when the source changes location and the artifact's features, generally, do not change shape. Unless stated otherwise, measurements were done with a ^{238}PuBe source, which emits a characteristic 4.442 MeV gamma ray from an excited state of $^{12}C^*$ from the reaction $\alpha + \text{Be} \rightarrow \text{n} + {}^{12}C^*$ [44] with an energy spectrum available in Fig. 3.3. Only photopeak events were considered for imaging and wide energy bounds $[4.375, 4.589]$ MeV were chosen due to the Doppler broadening of the resulting 4.4 MeV gamma ray.

Fig. 3.4a shows a reconstructed image of a cathode irradiation which is compromised with significant artifacts that conceals the source hotspot completely. Placing the source on the left side of the detector ($+\hat{x}$), as shown in Fig. 3.4b, results in a faint hotspot at $(\phi, \theta) = (0°, 90°)$, but with significant background noise and a false hotspot at $(180°, 90°)$. Regardless of the source location, the images contain a checkered artifact centered at $(270°, 90°)$, which does not shift with the source location. The major contributor to this artifact are charge sharing effects which will be discussed in Sec. 3.4. Additional artifacts are present along the prime and 180^{th} meridian (all locations where $\phi = 0°$ and $180°$) of the image space which is mostly noise from pair-production interaction and incorrectly sequenced events, discussed in Sec. 3.3 and 3.4 respectively.

3.3 Artifacts from Pair Production Events

A pair-production interaction creates an electron-positron pair where the positron will thermalize and annihilate with an electron and produce two annihilation photons at 511 keV ($e^+ + e^- \rightarrow \gamma + \gamma$). The annihilation photons are generally emitted colinearly in anti-parallel directions. In a photopeak event, the gamma ray deposits all its energy. Therefore, under the photopeak, if the first interaction results in a pair production, both the annihilation photons must deposit their whole energies in the detector.

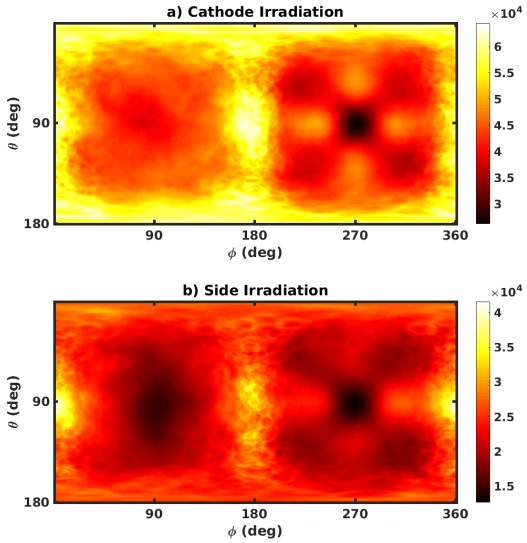

Figure 3.4: Raw SBP images of a PuBe source for a) cathode irradiation with source location $(90°, 90°)$ using 33,000 imaged counts, b) left side irradiation from $(0°, 90°)$ consisting of 16,000 counts. No events were discarded and the sequencing algorithms used were 'Simple Comparison' and 'MSD'. The data considers 2, 3, 4, and 5 pixel events. From the two images, there appears to be significant artifacts in the prime and 180^{th} meridian of the image along with a checkered pattern located around $(270°, 90°)$. The color scale represents intensity.

As this section aims to consider only pair-production artifacts, side-neighbouring events were not considered and removed from the datasets since charge sharing and pair-production event cannot be distinguished reliably. Fig. 3.5 plots the PuBe measurements with side-neighbouring events removed and the artifacts visible along the prime and 180^{th} meridian. This section explores this artifact and breaks it down into two components: distribution of the reconstructed Compton axes and the distribution of opening angles. The referencing of the axis, or lever arm, and opening angles of pair production events entails the reconstructed parameters computed by the imaging algorithm.

3.3.1 Distribution of Reconstructed Compton Lever Arm Axes

The distribution of reconstructed lever arms differs between pair-productions and Compton interactions. Fig. 3.6 plots the distribution on the image space for both

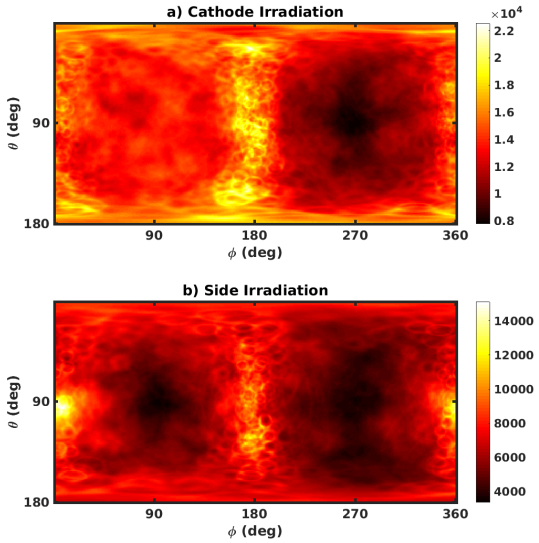

Figure 3.5: SBP images without side-neighbouring events of a PuBe source placed in a PVC tube of a) cathode irradiation $(90°, 90°)$ with 9,000 counts, b) left side irradiation from $(0°, 90°)$ with 4,200 counts. Both images present with severe contamination of pair-production events as observed by the small opening angle cones along the prime and 180^{th} meridian.

types of events. Fig. 3.6a-b plot the distribution of a ^{137}Cs cathode irradiation for simulated and experimental measurements. In an ideal infinitely large system, the distribution will follow that of the Klein—-Nishina differential cross section. However, since the detector is pixelated and finite, the locations of interactions are discretized and create fixed possible lever arms.

Pair-production does not, by definition, have lever arms so the 'Compton axis' is defined as the vector between the second to the first sequenced interaction that are falsely reconstructed by the Compton imaging algorithm.

The lever arms produced by pair-production events are biased to the prime and 180^{th} meridian of the image sphere, which are associated with the sides of the detectors, away from the anode and cathode direction. Their distribution, like the artifact themselves, are independent of source location. This is shown in Fig. 3.6c-d which plots the distribution of lever arm vectors on an image space for simulated 4.4 MeV gamma-ray sources with different irradiation locations. Although the annihilation photons have

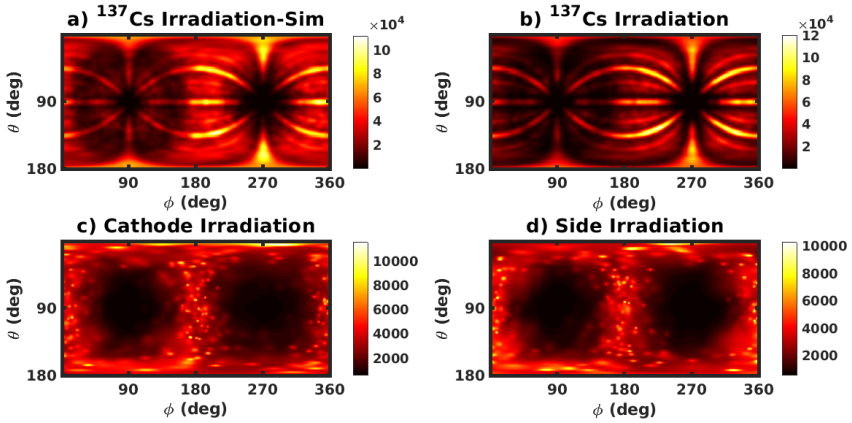

Figure 3.6: Distribution of the Compton axis lever arms projected onto the image space. A cathode $(90°, 90°)$ irradiation with a) simulated ^{137}Cs source and b) an experimental ^{137}Cs irradiation, which show the expected distribution of lever arms from Compton interactions and agreement between simulation and experiment. The concentric "eyelid" bands arise from the pixelation of the detector which discretizes the distribution of lever arms. The lever arms projected onto the image space for a simulated 4.4 MeV source given that the first interaction undergoes a pair-production is presented for c) cathode irradiation $(90°, 90°)$ and d) irradiation from $(180°, 90°)$.

a non-uniform distribution with respect to the momentum of the positron [45], they can be considered to be emitted isotropically, (where the two photons are emitted in opposite directions), as the positron has a nearly random walk towards the end of its track. It is therefore natural to conclude that the lever arm vectors from the events will also be isotropic in the image space. However, the system response creates a void in the space in front of the anode and cathode which is due to the pixelation of the detector. Any two interactions that occurs laterally in the y-axis will be summed into a single observed pixel or side-neighbouring event. However, if the events are separated in the $x - z$ axis, the system is then able to distinguish the different interactions.

Fig. 3.7 illustrates three possible events which aid in the understanding of the directional bias of pair-production produced lever arms. In the figure, "Event 1" shows a 3-pixel event where the resulting annihilation photons have interacted in the $x - z$ plane and have sufficient distance between them to distinguish the three separate interactions. "Event 2" results in side-neighbouring interactions which are discussed

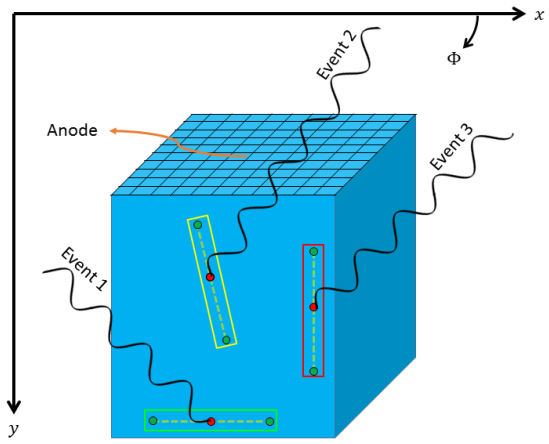

Figure 3.7: Three possible events where pair-production is the first interaction with full energy deposition. Event 1 demonstrates the two annihilation photons that have been separated sufficiently to be recorded as a three-pixel event. Event 2 results in a side-neighbouring event and therefore would not produce any lever arms in the cathode/anode direction. Event 3 would result in a single pixel event as the detector will not be able to distinguish between the different depths.

in Sec. 3.4. In the current section, they are removed from the data, adding to the void in the distribution. "Event 3" shows a 3 interaction event that will be concatenated into a single pixel event thereby not creating a lever arm in the anode or cathode direction.

3.3.2 Reconstructed Opening Cone Angle Distribution

For an infinitely large detector, the ideal distribution of Θ would resemble the Klein—-Nishina differential cross section distribution. However, system geometry, asymmetry, electronic threshold, and source location all affect the distribution of opening angles. In addition, incorrect event sequencing alters the distribution.

Fig. 3.8 plots the distribution based on the number of pixel events and interaction mechanisms. The simulated data models a 4.4 MeV gamma source and contains all the physics lists mentioned in Sec. 3.2.2, however, the simulated events are partitioned and shown separately. "Sim-Pair Production" only considers events where pair-production is the first interaction while "Sim-Scattering/Photoelectric" only considers events

when Compton scattering or photoelectric interactions occur first. The experimental data presents the cathode irradiation with the PuBe source (same data as Fig. 3.5a). Finally, the "True Scattering Distribution" represents a simulated distribution of Compton scatters with true sequencing for incident 4.4 MeV gamma rays while the other simulated dataset is processed as they would for standard SBP imaging with sequencing algorithms.

Several features are observed in the angle distribution in the experimental data set, including a peak in the low angle region, $\Theta = 7°, 10°$, and a peak near $\sim 83°$. These features contribute to image artifacts. Since there is no reliable experimental technique to differentiate between pair-production and Compton scattering on a CdZnTe detector, the experimental data contains both interactions and is analogous to the sum of "Sim-Pair Production" and "Sim-Compton Scattering/Photoelectric" data.

3.3.2.1 Two-Pixel Event Opening Angle Distribution

The large discontinuity for the sequenced two-pixel events in the Fig. 3.8a is a consequence of the sequencing algorithm. The nature of the simple comparison algorithm organizes the events into two regions. Events not in those regions will be incorrectly sequenced and placed into one of those regions. The two regions are characterized by energy of the first interaction (E_1): $E_1 = (0, \frac{m_e c^2 E_0}{m_e c^2 + E_0})$ and $E_1 = (0.5E_0, Compton\ Edge]$. The behaviour of the two regions are discussed in the following:

1. The first region consists of small angle scatters where the second deposited energy is larger than the Compton edge, or the first interaction deposits less than $E_1 = (m_e c^2 E_0)/(m_e c^2 + E_0)$, which the algorithms sequences correctly.

2. The second region is characterized when the first interaction has deposited energy greater than $0.5E_0$, which involves "large" scatters.

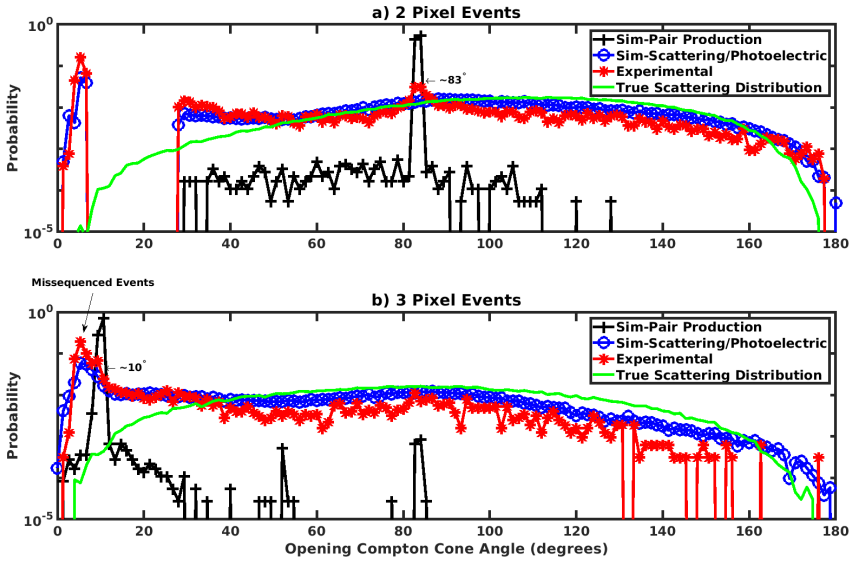

Figure 3.8: Distribution of opening angles for a) two interaction events and b) three interaction events. The simulated data models a 4.4 MeV gamma-ray source where the pair-production data represents simulated events where pair-production lead to the first interaction followed by any other possible interaction physics while the Compton scatter/photoelectric data (blue circle) only contain Compton scattering or photoelectric effect as the first interaction. The experimental data is from the cathode irradiation with the PuBe source. 'True Scattering Distribution' (green solid line) represents the simulated opening angle distribution for correctly sequenced events. The red asterisk present the experimental distribution.

Therefore, if the first interaction deposits in the range $E_1 = [\frac{m_e c^2 E_0}{m_e c^2 + E_0}, 0.5E_0]$, the event will be falsely sequenced and placed out of that region leaving a void in the distribution.

The small angle features in Fig. 3.8a are visible in both the experimental and the 'Sim-Scattering/Photoelectric' data. They represent events that have had bremsstrahlung or characteristic x-ray that triggered another pixel, events that have undergone charge sharing, and events that have multiple interaction under the same pixel.

Another significant feature peaks at ($\Theta \sim 83°$) and is visible in both the 'Sim-Pair Production' and experimental data, but not in the 'Sim-Scattering/Photoelectric' data. The peak is produced when one annihilation photon interacts at the same location as the pair-production event and the other interacts elsewhere in the detector. Therefore, the two recorded interactions for an incident 4.4 MeV gamma ray would be $\{0.511, 3.880\}$ MeV. The sequencing algorithm would choose the larger energy as the first interaction leading to a $\Theta \approx 83.3°$.

3.3.2.2 Three-or-More Pixel Event Opening Angle Distribution

Three pixel events naturally occur with pair production; the creation site and the two annihilation photons lead to the three observable interactions. If a pair production event leads to more than three interactions, it could indicate that one of the annihilation photons Compton scattered, or that charge sharing has occurred. This section only analyzes three pixel events, but could be extrapolated into 3+ pixel events.

Due to the sensitive behaviour of the MSD algorithm and the fact that it does not account for pair-production physics, either the pair-creation site or the annihilation photon may be sequenced first. If the annihilation photon is sequenced first, the calculated opening angle for a 4.4 MeV will result in $\Theta = 10°$ which is a visible artifact in Fig. 3.8b in the sim-pair production and experimental data. Like in

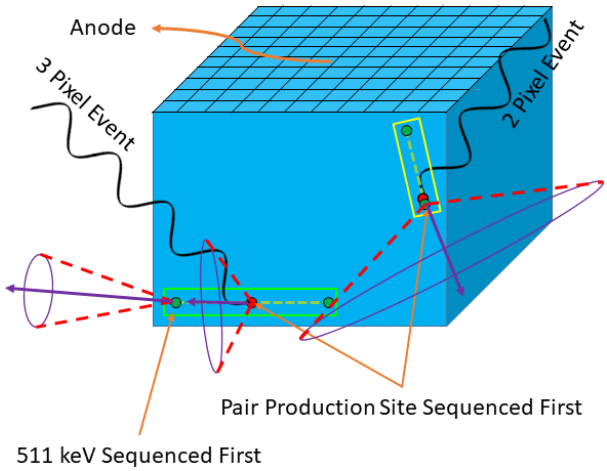

Figure 3.9: A graphic presenting 3 possible reconstructed cones of pair-production events. The green circles represent the annihilation photons undergoing a photoelectric event while the red circles represent the pair-creation site. Two pixel interactions are reconstructed with an opening angle of ($\Theta \sim 83°$) for a 4.4 MeV event while a three pixel event reconstructs 10° or 50° depending on how the event is sequenced.

the two-pixel data, there is a peak around ($\Theta \sim 83°$) which is also due to the pair-production+annihilation photon interaction site being sequenced as the first interaction. Although not visible in the experimental data, there is a peak at ($\Theta \sim 52°$) which corresponds to when the pair-creation site is sequenced first. There are additional events with opening angles less the 10.02° which represent incorrectly sequenced events and are discussed in Sec. 3.4.

3.3.3 Conclusion of Pair Production Artifacts

The artifacts observed from pair-production characteristically produce Compton cones with opening angle near 10°, 52° and 83° for an incident 4.4 MeV gamma ray. Two and three pixel events produce a cone with an opening angle of 83° for when the 511 keV interacts at the same location as the pair creation site, which is then sequenced first. Three pixel events produce an opening angle of 10° when the annihilation photon is sequenced first, 52° when the pair-creation site is sequenced first. Fig. 3.9 illustrate the different opening angles that might occur.

The resulting image artifacts from pair-production are isolated and plotted in

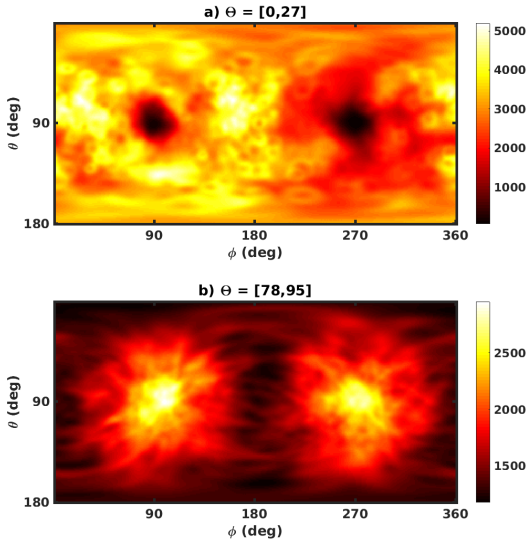

Figure 3.10: Isolated artifacts due to pair-production and incorrectly sequenced events in Compton images for cones reconstructed with an opening angle range of a) $\Theta = [0, 27]^\circ$, which represent mostly incorrectly sequenced events with some pair-production artifacts from $\Theta = 10^\circ$. b) Is an image using only $\Theta = [78, 95]^\circ$ which represent mostly pair-production events. Both images are from cathode irradiation and present in 2, 3, 4, and 5 pixel events.

Fig. 3.10. Although low opening angles can easily be identified as background, the large opening angles can give the illusion of a hot spot, when in actuality, are superimposed rings that added constructively.

3.4 Artifacts of Side-Neighbouring, Charge Sharing, and Incorrectly Sequenced Events

After a Compton scatter, an electron is ejected with energy proportional to the energy deposited by the gamma ray. The primary electron may lead to the creation of electron-hole pairs from Coulombic interactions and radiative processes. With an electron that has a larger initial energy, naturally, a larger "electron cloud" whose generated cross section may span multiple pixels. The induced charge is then shared between multiple pixels which degrades the induced signal due to weighting potential cross-talk (WPCT) and readout electronic noise [42].

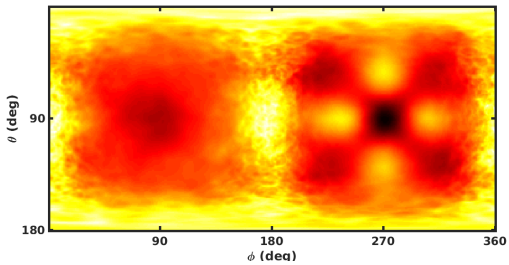

Figure 3.11: Raw SBP images of a PuBe source cathode irradiation $(90°, 90°)$ using 24,000 side-neighbouring events. The sequencing algorithms used were 'Simple Comparison' and 'MSD'.

The larger electron clouds lead to worse position resolution [13]. Combined with the energy blurring effects, like Doppler broadening, the event sequencing efficiency is reduced which adds significant image artifacts.

3.4.1 Artifacts from Charge Sharing and Side-Neighbouring Events

Fig. 3.11 is an image reconstructed using only side-neighbouring events from the PuBe measurement. As seen in the image, cones are biased to the prime and 180th meridians in the image. This is largely due to the side-neighbouring events being reconstructed in the $x - z$ plane without much separation in depth ($\hat{y}$). If an electron cloud is elongated in the $\hat{y}$ direction, the detector will reconstruct a single pixel event. However, interactions that expand in the $x - z$ plane will be recorded as a multiple pixel event. Since recorded multi-pixel events are distributed in the $x - z$ plane, reconstructed lever arms will be biased away from $\pm\hat{y}$.

Another charge-sharing artifact is a checkered pattern region centered at $(270°, 90°)$, a direction associated with the anode. The artifact is present in both the cathode and side irradiation and does not shift location when the source location shifts. This phenomena arises from large electron clouds that encompass multiple pixels where one pixels collects a majority of the electrons while the neighbouring pixel collects less charge. Due to WPCT, the triggered pixel that collects less of the electron cloud will reconstruct the event as closer to the anode. Therefore, what is a single interaction

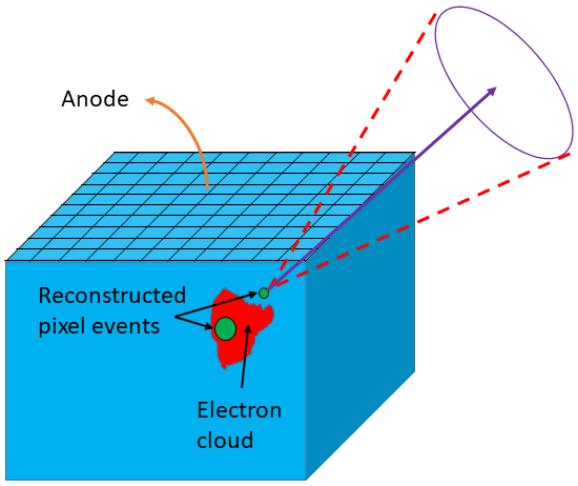

Figure 3.12: Presented is an example of weighting potential cross-talk that effects the reconstruction of a two pixel event. Illustrated in red is an electron cloud that spans two pixels. The electron cloud is then reconstructed to two events shown in green. Due to WPCT, the part of the cloud that is smaller, will be reconstructed closer to the anode. Finally, a Compton cone is sketch to show the final reconstruction.

is recorded as a two adjacent pixel event with one of the pixel event incorrectly reconstructed as being closer to the anode. This now creates a vector in the direction of the anode, as shown in Fig. 3.12. A more in depth discussion on WPCT can be found in [46].

3.4.2 Artifacts from Incorrect Event Sequencing

Incorrectly sequenced events have been characterized for a 662 keV source in Lehner *et al.* [15]. However, in high energy gamma rays, their mechanisms slightly differ. Referencing (3.1), a larger E_0 and a small E_1, which the incorrect sequence will infer, will lead to a small opening angle. This can be seen in Fig. 3.8b, where there are a significant number of events with opening angles under 10°, in both the experimental results and simulated data with only Compton scattering physics. In addition, the true distribution of scattering events does not show a large distribution of small angle scattering. The isolated artifacts can be seen in Fig. 3.10a.

3.5 Techniques for Artifact Mitigation in High Energy Gamma-Ray imaging

3.5.1 Discussion of Charge Sharing Events

Artifacts from side-neighbouring events are simple to identify as events with interactions in adjacent pixels are most likely charge-sharing. Removing these events results in a 75% loss in counts for either the side or cathode irradiation. These events can then in principle be clustered together, as done in [47] for two pixel events, but will require further research to optimize for high-energy gamma-ray events. Thought must be given to distinguishing between charge sharing, a true side-neighbouring events (a Compton scatter followed with a photoelectric event), and pair-production events. In addition, a high threshold was chosen to reduce noise and reducing the number of low-energy events readout during measurement as the detector has low efficiencies at that energy. Therefore, if the events were to be clustered, there will be missing energy from the pixels that did not record charge beneath the threshold.

3.5.2 Tagging of 511 keV Annihilation Photon

Since pair-production can organically be tagged by the detection of a 511 keV interaction, it is natural to conclude that omitting events that have an energy deposition of 511 keV will remove pair-production artifacts. The energy range that is chosen to be removed must be generous as the resulting 511 keV from annihilation are Doppler broadened. This implies that the energy range chosen must be larger than the measured energy resolution of the system. Removing those energies and applying an opening angle cut, as presented in Sec. 3.5.3 are practically identical. It is advised to review the opening angle distribution (or the energies of the first interactions) to observe the scope of the 511 keV contamination.

3.5.3 Opening Angle (Θ) Discrimination

The artifacts presented in sections 3.3-3.4 produce Compton cones with characteristic opening angles. The opening angles are summarized for each observed phenomena and are referenced by the different colour markers utilized in Fig. 3.13, which presents the reconstructed opening angle, Θ, as a function of incident energy for different sequenced events.

1. ***Red plus:*** These small opening angles are associated with three pixel events when the 511 keV interaction from pair-production is sequenced first and an opening angle $\Theta = \arccos\left(1 - \frac{[m_e c^2]^2}{E_0(E_0 - m_e c^2)}\right)$ is reconstructed. Other small opening cone artifacts are produced by incorrectly sequenced events, x-ray production and multiple interaction in the same pixel as seen in Sec. 3.4.

2. ***Green circle:*** Pair-production also results in opening angles near $\Theta = \arccos\left(1 - \frac{E_0 - m_e c^2}{2E_0}\right)$, when the pair-production site is sequenced first. This is most common in two pixel events but can occur in three pixel events as well.

3. ***Blue asterisk:*** Two pixel events should be cut at angles corresponding to the curve which sequences the pair-production+annihilation first, or when $\Theta = \arccos\left(1 - \frac{E_0 - m_e c^2}{E_0}\right)$.

4. ***Black triangle:*** Two-pixel events with opening angles below the black curves ($\Theta = \arccos\left(1 - \frac{m_e c^2}{E_0}\right)$) should be cut as well as they might represent contamination from X-ray triggers, multiple interactions under the same pixel and pair-production event. Detection of low angle scatters are less probable at high energies, seen in Fig. 3.8, as the photoabsorption cross section for those scattered energies is severely reduced. In this study, imaging of events below the black curve resulted in a poor image with no apparent hotspot.

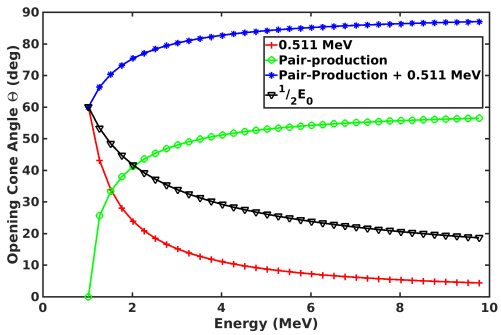

Figure 3.13: Opening angles for incident energies in the range $E_0 = [1.022, 10]$ MeV. The different curves correspond to different interactions that were sequenced first. Three pixel events mostly sequences the annihilation photon first (red). The most significant two-pixel pair-production artifact results from the "Pair-production + 0.511 MeV" (in blue). Two-pixel interactions with opening angles beneath that of $\frac{1}{2}E_0$ should be discarded as they most likely correspond to charge-sharing.

These cuts were applied to the PuBe measurement data and resulted in Fig. 3.14. They result in an additional loss of 50% of the image counts.

3.5.4 Mitigation Through the FIL-MSD Sequencing Algorithm

Three-pixel-events can either be sequenced with MSD or FIL-MSD by the calculation of a FOM. MSD will generally sequence the 511 keV deposition to be the first interaction in pair production event. FIL-MSD will also sequence the annihilation photons first for energies below $E_0 = 3m_ec^2$, as the pair-creation site will have less energy than an annihilation photon. However, at higher energy ranges, the pair-creation site will have more deposited energy than an annihilation photon. With the pair-creation site sequenced first (by FIL-MSD), the FOM calculation results in a low or zero value as the algorithm assumes that the gamma-ray scatters off the creation site in a 90° angle, then back-scatters depositing 511 keV. A 4.4 MeV source was simulated only considering pair-production events and shows that FIL-MSD will discard ∼3.5 times more pair-production events than MSD. A comparison of the two sequencing algorithms is shown in Fig. 3.15 using the PuBe cathode data where the FIL-MSD can produce a hotspot while the MSD algorithms still contains significant noise.

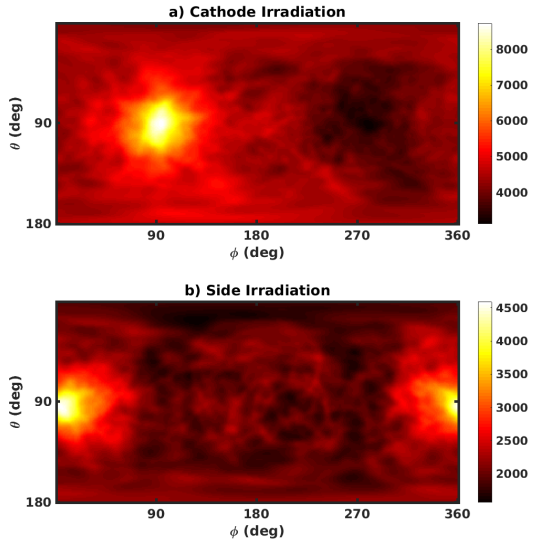

Figure 3.14: SBP images of the experimental PuBe measurements with the mitigation techniques discussed in Sec.3.5.3. a) Presents the cathode irradiation image with 4,500 counts while b) images the side irradiation with 2,150 counts all consisting of 2, 3, 4, and 5 pixel events.

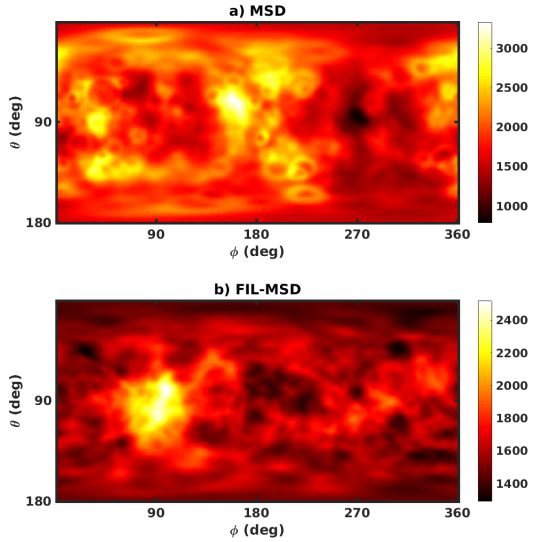

Figure 3.15: PuBe measurement sequenced with a) the MSD algorithm and b) the FIL-MSD algorithm. Using the MSD algorithm, it is clear that a hotspot is not reconstructed correctly while FIL-MSD reconstructs the source. The images consist of only three-pixel events and no opening angle cuts were applied.

3.5.5 Application of Analysis to More Advanced Imaging Algorithms

The analysis on image artifacts in this study was completed using simple back-projection. However, the analysis can be quickly applied to filtered backprojection (FBP) since SBP imaging forms the basis to FBP. The mitigation techniques are therefore transferable to inverse based reconstruction algorithms. However, identifying the artifacts in iterative based image algorithms, such as maximum likelihood expected-maximization (MLEM), would not be as trivial. Additional analysis must be completed if the system response does not account for pair-production or charge sharing to understand the behaviour of such artifacts. However, event cuts could be applied during construction of the system matrix to prevent the formation of the artifacts.

3.6 Conclusion

Gamma-ray imaging is an important technique with a wide variety of applications. With new systems, such as the OrionUM CdZnTe system, high energy gamma-ray imaging of up to 9 MeV is possible which results in additional challenges.

This work investigates the image artifacts resulting from high energy gamma rays and characterizes them. These artifacts generally originate from charge sharing or pair-production events and can apply to other Compton imagers that are CdZnTe or scintillator based. When imaging the 4.4 MeV gamma ray from the PuBe source, pair-production contamination created artifacts with cone opening angles of 83.3° when the annihilation and pair-creation site occur under the same pixel and is sequenced first. When the annihilation photon is sequenced first, a 10° opening angle is calculated. Charge sharing and incorrectly sequenced events produce small opening cone angles which contaminate the image away from the $\pm\hat{y}$ direction. Without using any mitigation techniques, image reconstruction is unsuccessfully, as it is not able

to reconstruct the source. With this analysis, several techniques to mitigate image artifacts were presented which results in SBP images with clearer hotspots.

CHAPTER IV

Interaction Sequencing for High Energy 3-or-More Interaction Events

Sequencing gamma-ray interactions within a detector system is an integral component of Compton imaging. In detectors with poor timing resolution compared to the time interval of successive interactions, algorithms which order gamma-ray interactions must be implemented using only energy and position information. This work examines previous algorithms and inspects interaction kinematics to increase the sequencing algorithm's speed and effectiveness. The proposed method, in which the first interaction is assumed to deposit the largest energy, has improved sequencing performance by greater than 20% for full energy gamma ray depositions larger than 1 MeV that do not contain pair-production. In addition, the algorithm shows a decrease in computational costs for sequence reconstruction to allow for better real time reconstruction. Experimental results show an almost twofold increase in the signal to noise ratio (SNR) for simple backprojection images of a ^{22}Na source. Additional measurements of the 2.2 MeV gamma rays from $H^1(n,\gamma)D^2$ neutron capture demonstrates the proposed algorithm's superior performance.

In smaller detectors, where the timing resolution prevents the sequencing of

Based on published work: D. Shy and Z. He, "Gamma-ray Tracking for High Energy Gamma-ray Imaging in Pixelated CdZnTe," Nuclear Instruments and Methods in Physics Research Section A: Accelerators, Spectrometers, Detectors and Associated Equipment, Volume 954, 21 February 2020

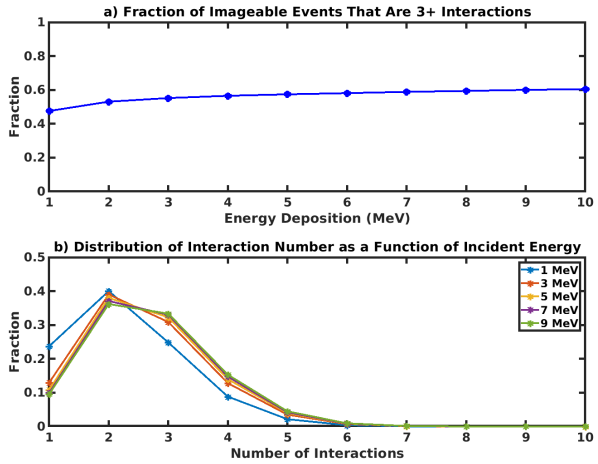

Figure 4.1: a) Fraction representing the number of 3+ interaction events with respect to the total number of imageable events (2+). b) Distribution of the number of interactions as a function of energy deposited due to kinematic interactions alone. Note that in reality, the distribution would be skewed to favor higher number of interactions due to detector charge sharing and physics effects such as bremsstrahlung.

interactions, "sequence reconstruction", or "gamma-ray tracking", algorithms must be implemented to sequence events [15]. This paper explores sequencing events that undergo three-or-more (3+) interactions. To illustrate the importance of sequencing 3+ interaction, a simulation was completed which kinematically models the number of interactions a gamma ray undergoes before being fully attenuated in the detector, neglecting pair-production. Fig. 4.1a plots the fraction of 3+ events with respect to the total number of imageable events. Already, at 1 MeV, the fraction is close to 50%. Fig. 4.1b plots the number of interactions as a function of full energy deposition which demonstrates that when exploring higher energies, the number of pixel events slightly increases.

4.1 Sequence Order Reconstruction

N represents the number of interactions a gamma ray has undergone in the detector; thus, there are $N!$ possible permutations for each event. For sequence order indexing, the bold numeric indexes represent the chosen sequence order. Capital Roman alphabet

designate an order based on decreasing energy and lower case alphabet represents some scrambled sequence. Combined with inferences that could be made from the kinematics of Compton scattering, the techniques presented in the following sections have been developed for events with different numbers of interactions.

The consequences of false sequencing depend on the number of interactions, incident energy, and detector geometry [15]. One artifact that incorrect sequencing will produce is a ring, or halo, around the true source location as well as a decrease in the signal to noise ratio (SNR) of the image, further discussed in 4.6.

There are several popular methods available to reconstruct three-or-more pixel events, among them, are the deterministic method and Minimum Squared Difference (MSD) technique [26, 48, 49]. The deterministic method simply chooses the sequence with the highest probability of occurrence by calculating the probability of the interaction for each possible sequence permutation with the Klein-Nishina differential cross section and attenuation probabilities. The MSD method, however, assigns a figure of merit (FOM) to each possible sequence by comparing the angle between three interactions ($\theta = \measuredangle \mathbf{r}_a\mathbf{r}_b\mathbf{r}_c$) [50], calculated using the physical locations of interactions and the Compton scattering formula with the following expression [22]:

$$\text{FOM} = \frac{1}{\sqrt{\sigma_{\theta_E}^2 + \sigma_{\theta_R}^2}} e^{-\frac{(\theta_E - \theta_R)^2}{2\left(\sigma_{\theta_E}^2 + \sigma_{\theta_R}^2\right)}}, \tag{4.1}$$

where θ_E is the angle calculated between the first three interactions using the Compton scattering equation while θ_R is the measured angle. The associated error of the angles is calculated by error propagating the position and energy information of the event and are denoted by σ_{θ_E} and σ_{θ_r} [43]. The sequence with the highest FOM is selected for imaging.

Both methods require calculations for all $N!$ possible sequence permutations. The MSD technique has been shown to outperform the deterministic method in both accuracy and computational cost [51]. This technique can be expanded to 3+

interaction events by summing the FOM for each triplet in the sequence.

4.2 Kinematics of Multiple Compton Scatters

The Compton-scattering differential angular cross section is described by the Klein-Nishina (KN) formula [52]. It computes the angular likelihood of scattering a photon into a solid angle $\mathrm{d}\Omega$ in scattering direction θ with the expression:

$$\frac{\mathrm{d}\sigma}{\mathrm{d}\Omega} = \frac{r_0^2}{2}\left\{\frac{1}{\left[1+\alpha(1-\cos\theta)\right]^2}\left[1+\cos^2\theta+\frac{\alpha^2(1-\cos\theta)^2}{\left[1+\alpha(1-\cos\theta)\right]}\right]\right\}, \tag{4.2}$$

where $r_0 = e^2/m_e c^2$ represents the classical radius of the electron and $\alpha = E_0/m_e c^2$.

4.2.1 Probability of Electron Recoil Energy Calculation using Klein—-Nishina Cross Sections

To explore the differential cross section for a Compton scatter to produce a recoil electron in an interval $[T,\ T+\mathrm{d}T]$, the following Jacobian coordinate transform is applied:

$$\frac{\mathrm{d}\sigma}{\mathrm{d}T} = \frac{\mathrm{d}\sigma}{\mathrm{d}\Omega}\left[\frac{\mathrm{d}\Omega}{\mathrm{d}\theta}\frac{\mathrm{d}\theta}{\mathrm{d}T}\right], \tag{4.3}$$

The expression, $\mathrm{d}\Omega/\mathrm{d}\theta = 2\pi\sin\theta$, is obtained from the definition of the solid angle differential. The electron recoil energy is defined as $T = E_0 - E_1' = E_0\frac{\alpha(1-\cos\theta)}{1+\alpha(1-\cos\theta)}$, where E_1' represents the energy of the photon after the first scatter. It can be rearranged and differentiated to result in $\mathrm{d}\theta/\mathrm{d}T$. The final expression in terms of (4.2) is:

$$\frac{\mathrm{d}\sigma}{\mathrm{d}T} = \frac{2\pi m_0 c^2}{[E_1']^2}\frac{\mathrm{d}\sigma}{\mathrm{d}\Omega}. \tag{4.4}$$

The shape of the KN cross section changes as a function of incident energy which shapes the Compton continuum [53]. Fig. 4.2 shows the shape of the continuum for different incident energies. Note that in practice, the shape of the continuum is affected by the geometry of the detector and is blurred by detector response. When comparing the different continua, the curves become more asymmetric and biased towards higher electron recoil energies as the incident gamma-ray energy increases. This can be

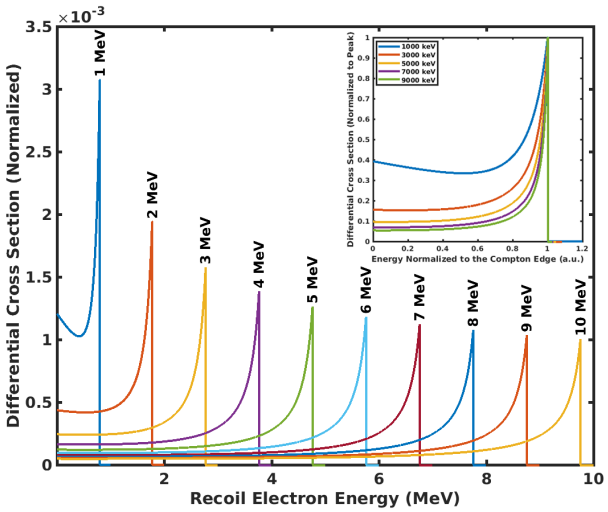

Figure 4.2: Klein-Nishina differential cross section as a function of recoil electron energy (T) for different incident energy gamma rays. The curves are normalized with the total cross section for scattering at that incident energy. Inset are the cross sections for different incident energies with the Compton continuum normalized to the Compton edge.

seen in the graph inset in Fig. 4.2, which shows the cross sections normalized to the Compton edge. In other words, as the incident gamma-ray energy enlarges, the distribution of the produced recoil electrons will be skewed left, where the median is greater than the mean.

4.2.2 Probability that the 1st Interaction Deposits the Largest Energy in the Sequence

The shape of the Compton continuum, as shown in Fig. 4.2, can explain the fraction of two-interaction events in which the first interaction has a larger deposited energy than the second interaction, ($E_1 > E_2$). The fraction of events in which the first interaction deposits the most energy in the sequence is represented by the First-Is-Largest (FIL) fraction. The FIL fraction for a two-interaction event within an infinitely large detector is described in (4.5), where KN(ϵ) represents the Klein–Nishina differential cross section for energy ϵ, and CE is the Compton edge for incident energy

E_0. The lower limit ($\frac{E_0}{2}$) in (4.5) is chosen, since the event must be FIL if the first interaction deposits an energy $\frac{E_0}{2}$ or higher.

If an interaction deposits less than $E_1 = \frac{E_0}{N}$, where N is the number of interactions, it could never be a FIL event. Therefore, (4.5) is used to describe the lower bound of the FIL ratio. For 3+ interaction events, $E_1 = \frac{E_0}{N}$ is used for the lower integral limit of the FIL upper bound ratio since it may still produce an FIL event. This can be proven by first defining the variable f_i, which is the deposited energy in the i^{th} interaction as a fraction of E_0, ($E_2 = f_2 E_0$), and note that $\sum_{i=2}^{N} f_i = 1 - f_1$. Next, the fraction f_1 is found where $E_1 > E_i \ \forall \ i \in \{2, \ldots, N\}$, or where $\frac{E_i}{E_1} = \frac{f_i E_0}{f_1 E_0} = \frac{f_i}{f_1} < 1$. Then, the summation of $\frac{f_i}{f_1}$ is taken, which yields $\sum_{i=2}^{N} \frac{f_i}{f_1} = \frac{1}{f_1} \sum_{i=2}^{N} f_i < \sum_{i=2}^{N} 1 = N - 1$. Solving for f_1 yields $f_1 > \frac{1}{N}$ for the fraction of E_0, or $E_1 > \frac{E_0}{N}$, to deposit in the first interaction and still result in an FIL event. Therefore, (4.6) is defined as the upper bound for the FIL fraction, or $P(E_1 > E_i) \ \forall \ i \in \{2, \ldots, N\}$. Fig. 4.3 plots both the bounds for the FIL fraction in an infinite detector for different number of interactions.

$$\mathrm{FIL}(E_0)_{lower\,bound} = \frac{\int_{\frac{E_0}{2}}^{CE} \mathrm{KN}(\epsilon)\mathrm{d}\epsilon}{\int_{0}^{CE} \mathrm{KN}(\epsilon)\mathrm{d}\epsilon} \tag{4.5}$$

$$\mathrm{FIL}(E_0)_{upper\,bound} = \frac{\int_{\frac{E_0}{N}}^{CE} \mathrm{KN}(\epsilon)\mathrm{d}\epsilon}{\int_{0}^{CE} \mathrm{KN}(\epsilon)\mathrm{d}\epsilon} \tag{4.6}$$

We therefore modify the standard MSD algorithm to assume that the first interaction is the largest (FIL) followed by the standard MSD figure of merit calculations for the subsequent interactions. This technique is referred herein as the "FIL-MSD" algorithm.

It is natural to conclude from the FIL fraction that the subsequent interactions will deposit the next highest energies. This is what is referred to as ABC sequencing, but our results have shown it to be inferior to FIL-MSD as the ABC sequence does not have a high probability of occurrence. After the first interaction, the gamma ray loses a significant amount of energy where the scattered gamma-ray does not have enough energy to continue to produce an FIL event. Instead, a "Complex Comparison"

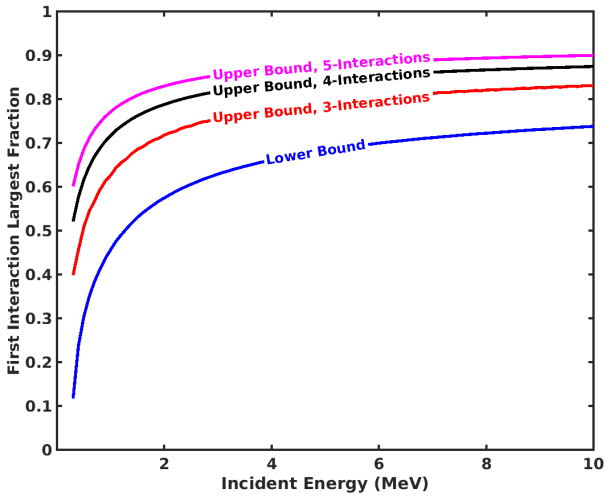

Figure 4.3: FIL fraction limits for events in which the first interaction deposited the largest energy in the sequence for various incident energies in an infinite detector.

method was developed where an ABC or ACB sequence is chosen based on the energy of the scattered gamma-ray ($E_1' = E_0 - E_1$), where the first interaction is assumed to be FIL. The next two interactions are sequenced using the simple comparison technique. This technique has shown better results than MSD but lower efficiency than FIL-MSD. Nevertheless, Complex Comparison is useful for detector systems that have poor position resolution which degrades the MSD performance.

4.3 Monte Carlo Simulation

4.3.1 Simulation Parameters

Simulations using GEANT4 were performed to model the behaviour of the Orion prototype [54]. Multiple gamma-ray interactions under the same pixel anode were treated as a single site interaction. Since it is not possible to Compton image an event if the first interaction results in a pair-production, the pair production physics package was not included in the program physics lists for computational considerations. The fraction of events that have a pair production event following a Compton scatter

interaction is negligible for full energy deposition events. Presenting pair production data may be misleading. Data generated for the sequencing studies did not include electron thermalization, or the loss energy of the electron in the medium, and therefore did not include the triggering of multiple pixels by a single interaction. Another simulation was performed to study the movement of the recoil electron traversing the material to quantify the associated position blur from the electron cloud size. The simulated data that was created for the sequencing study modeled 1e8 gamma rays that were randomly produced in various directions.

4.3.2 Production of Realistic Data by Estimating Position Resolution

A major factor in position resolution is the size of the electron cloud produced by the recoiled electron. Since larger deposited energies produce larger electron clouds, the induced signal on each pixel will significantly change and affect the position reconstruction. The electron clouds were modeled in GEANT4 by tracking the electron paths. The cloud's size is defined as the distance between the largest separation between two electrons as done by Kim *et. al* [42]. Fig. 4.4 shows the electron cloud distribution as a function of deposited energy with a log-log fit shown in (4.7).

$$\begin{aligned} Y &= 1.8X + 2.6, \\ Y &= \log_{10} \text{diameter } (\mu\text{m}), \\ X &= \log_{10} \text{energy (MeV)}. \end{aligned} \tag{4.7}$$

The model does not show the decrease of position resolution of low-energy depositions caused by the decrease in induced transient signals, compared to the readout electronic noise, and is not considered in this study.

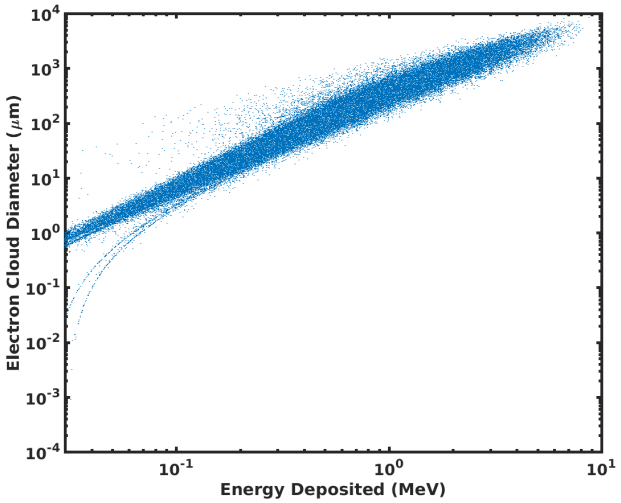

Figure 4.4: Electron cloud size as a function of single-site deposited energy in CdZnTe. Note that the log-log fit could be simplified to $Diameter = 398.1E_{dep}^{1.8}$.

4.4 Results and Discussion

4.4.1 Simulated Algorithm Performance

The simulated data were analyzed using the different algorithms. The FIL-MSD algorithm is compared to the standard MSD algorithm in Fig. 4.5 and shows the percentage increase in accuracy as a function of the incident gamma-ray energy. The evaluation of the algorithm only considered events in which the gamma rays deposited all their energies in the crystal. The results show a greater than 20% increase in accuracy for FIL-MSD over standard MSD for 3+ interaction events that have energies higher than 1 MeV. The FIL-MSD algorithm is also more accurate for energies lower than 1 MeV and does better than MSD down to energies as low as 350 keV. Therefore, in cases where the incident gamma ray deposits less than 350 keV, the standard MSD could be implemented rather than FIL-MSD. The exact threshold for which FIL-MSD is inferior depends on detector shape.

A ^{22}Na source was simulated with GEANT4, modeling the source 1 meter away from the detector, and with no background. To show the benefit of the algorithm,

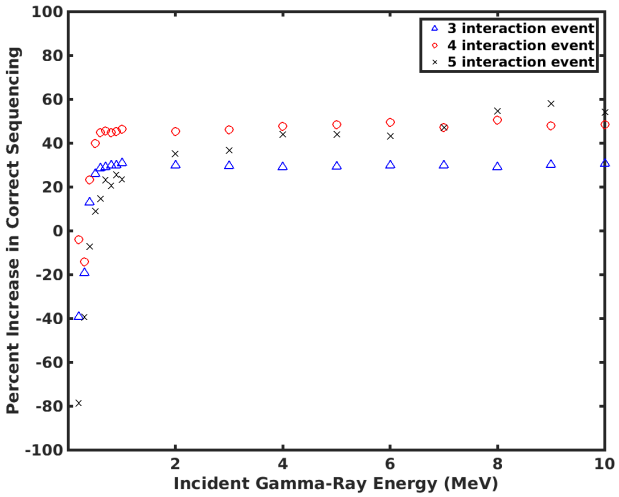

Figure 4.5: Percentage increase in accuracy when comparing the FIL-MSD and MSD algorithms for simulated events.

pair-production physics were not considered in this section. Fig. 4.6a-c present simple backprojection images using the a) true sequence, b) MSD, and c) FIL-MSD algorithms with a total of 100,000 events consisting of 3, 4, 5 interactions. From the figure, it is obvious that the image acutance has increased in the FIL-MSD algorithm and that the halo around the hotspot arises from false sequenced events. Table 4.1 displays the signal-to-noise (SNR) ratios of the images as well as characteristics of the point spread function (PSF). The SNR grew by a factor of 1.76 when comparing FIL-MSD with standard MSD. The increase in FWHM of the PSF is discussed in greater detail in Sec. 4.4.4.

4.4.2 Computation Cost Comparison

The computational cost is of interest, especially for higher energy gamma rays, as they are likely to have a larger number of interactions. The MSD algorithm requires a FOM to be calculated for every $N!$ permutation. However, by assuming FIL, the number of FOM calculations is decreased to $(N-1)!$ calculations, theoretically decreasing the computation by a factor of N. Table 4.2 shows the performance of

Table 4.1: Table of the associated FWHM and SNR of each SBP image using the two different algorithms. FWHM was measured by fitting a double Gaussian to the axial image slice. The SNR was calculated by (I/σ) with max value in the ROI (I) and the (σ) representing the standard deviation of the image outside the ROI. Data within 3σ was chosen as the ROI for the image. The SNR calculation for 'True' was omitted as it is not appropriate to calculate the noise of an image with no sequencing noise.

Algorithm	θ FWHM	ϕ FWHM	SNR (I/σ)
Simulated Data			
True	34.3	34.3	$\sim$
MSD	26.7	31.1	24.2
FIL-MSD	30.8	30.1	42.7
Experimental Data			
MSD	25.6	31.5	23.9
FIL-MSD	31.7	32.5	45.8

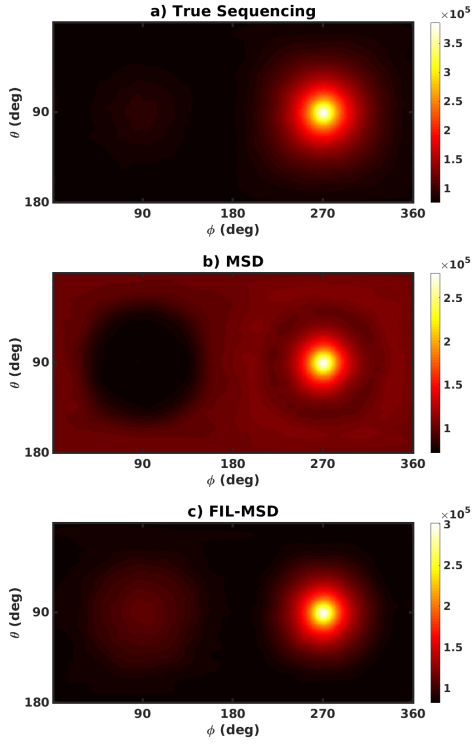

Figure 4.6: Simple backprojection images of a simulated ^{22}Na source using the a) true, b) MSD, and c) FIL-MSD sequencing algorithm. The image uses only 3, 4, and 5 pixel for a total of 100,000 events. The simulation consisted of an isotropic source defined to be 1 meter away from the detector.

each algorithm by analyzing the average time needed to reconstruct each event. It can be seen that the FIL-MSD computes the sequence faster than the standard MSD.

Table 4.2: Average computational time to sequence an event.

N	MSD (μs)	FIL-MSD (μs)	$t_{FIL-MSD}/t_{MSD}$
Three	12.5	6.5	2.1
Four	49.9	15.1	3.3
Five	492.1	106.6	4.9

4.4.3 Compton Image Reconstruction with Experimental Results

The University of Michigan Orion Prototype system measured and imaged a 45 μCi ^{22}Na gamma-ray source from 85 cm away using one CdZnTe Crystal. A simple backprojection (SBP) image using the standard MSD algorithm is displayed in Fig. 4.7a which used 8,600 photopeak events of only 3, 4, 5 interaction events. The visible ring and halo background artifacts in Fig. 4.7b arise from incorrectly sequenced events. Some artifacts may arise from background. However, since imaging was done using the photopeak, room return would have down scattered and not added to the image. Fig. 4.7b displays the reconstructed image using the FIL-MSD algorithm. It has a signal-to-noise ratio (SNR) 1.92 times better than that of the MSD image.

The FIL-MSD method creates an image artifact 180° from the true source location. This is due to the point spread function of scatters nearing 90° as well as missequenced events. The SNR and the associated FWHM of the point spread function (PSF) are tabulated in Table 4.1. The table shows an increase in the FWHM when comparing the FIL-MSD with the MSD reconstruction, which is most likely a result of the event type reconstructed.

4.4.4 Discussion on the Angular Resolution (FWHM) Calculation

The increase of the FWHM in the PSF for FIL-MSD may raise some concerns, but could also provide a positive indicator of the sequencing efficiency of the algorithm.

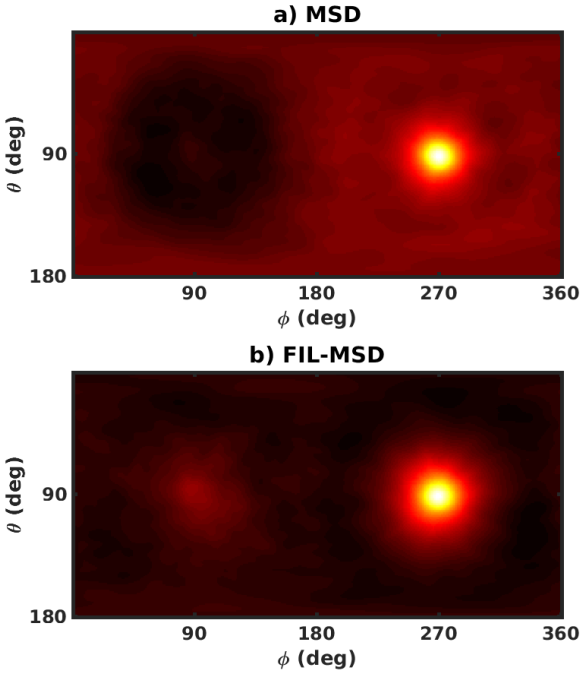

Figure 4.7: Simple backprojection images using only 3,4, and 5 pixel events of a ^{22}Na at 85 *cm* away from the detector, (a) using the standard MSD sequence reconstruction, (b) using FIL-MSD algorithm. Both the images were normalized to the peak of the MSD reconstruction.

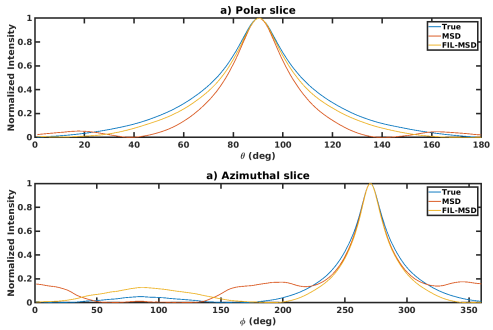

Figure 4.8: Point spread functions (PSF) of different sequencing algorithms using the simulated ^{22}Na data. a) The polar slice along the hot spot while b) plots the azimuthal. All curves were baseline subtracted with the minimum value. Note the two humps created from missequenced events by MSD left and right of the hotspot.

First, since different types of events have different responses (the PSF changes for different scatter angles), one can select events that produce high resolution images regardless of sequencing methods which produce a smaller FWHM. Using simulated data and the correct sequencing (Fig. 4.6a), a larger FWHM was reconstructed when compared to MSD and FIL-MSD. As all events are sequenced and used in the 'True' image, both high and low resolution events contribute to the image. The MSD/FIL-MSD algorithms produce a slightly smaller FWHM as they correctly sequence more high resolution events. In other words, MSD/FIL-MSD correctly sequences a subset of all events that are high resolution which artificially decreases the FWHM. We can further explore these phenomena by plotting the azimuthal and polar slices of the images (Fig. 4.8). The figure clearly shows that the 'True' sequencing image has the widest PSF. FIL-MSD sequences a broader range of events with higher efficiency, so event cuts could be implemented to isolate high resolution events.

4.4.5 Imaging the 2.2 MeV Gamma Rays off Neutron Capture on Hydrogen

It was also useful to image the 2.2 MeV gamma rays from the neutron capture on hydrogen and investigate the imaging performance of the new algorithm. This is

especially of interest for security and astronomical applications as it could indicate the presence of hydrogen when searching for explosives [55], or water on locations such as the moon [56]. In the experiment, using a 3×3 crystal Orion detector system, a 2.8 mCi ^{252}Cf, emitting 1.2e7 neutrons/s, was set in the middle of a $1^{\varnothing}$ ft $\times$ 1 ft polyvinyl cylinder tube. The source was placed 105 cm away from the cathode with all other detector faces shielded with lead and borated polyethylene to prevent contamination from room return.

Events that have a combination of interactions that sum up to a deposited energy of 511 ± 4 keV were removed as a means to discard pair-production events. Since electron-positron annihilation emit two photons near 511 keV gamma rays, it is a good indication that a pair-production event occurred. Fig. 4.9a-b present images of a 2 hour measurement of the source using only 3, 4, and 5 pixel events with the MSD and FIL-MSD algorithm respectively. All the possible opening cone angles (Θ from (2.1)) were used in those reconstructions. Fig. 4.9a shows significant artifacting from small angle cones, which do not backproject onto the true source direction. This is probably due to incorrectly sequenced events. Events that were reconstructed with an opening angle of less than 25°, sequenced with the MSD algorithm, are shown in Fig. 4.9c, where a hotspot is not clearly visible. Using that same data set, Fig. 4.9d was produced with the FIL-MSD algorithm, which shows a clear hotspot that was not visible in the MSD sequenced image. This shows that FIL-MSD has a higher sequencing efficiency than standard MSD. Re-sequenced and incorrect sequencing are discussed in 4.6.

4.5 Conclusion

The proposed FIL-MSD algorithm has shown at least a 20% increase in correct sequencing of events with full energy deposition. The increased in performance was analyzed for incident gamma rays above 1 MeV in simulated events that produce 3+

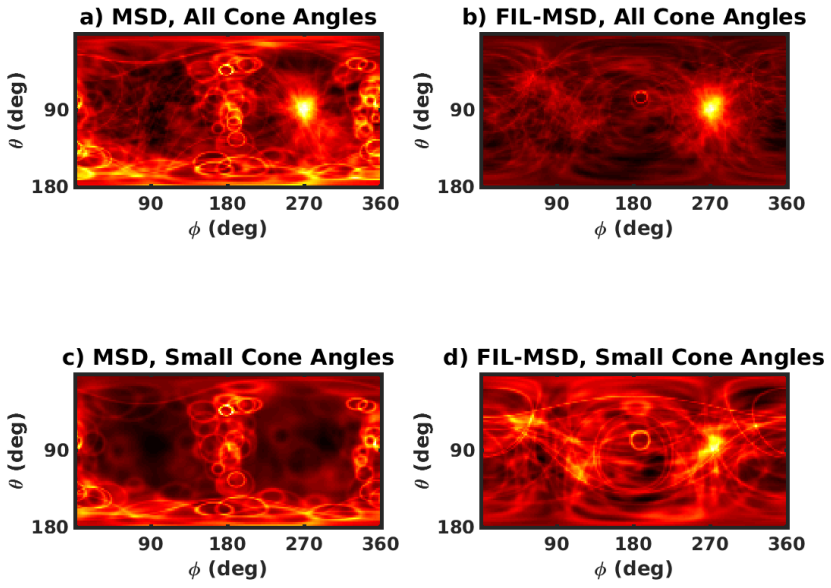

Figure 4.9: Simple backprojection image of a 2.2 MeV source using (a) the standard MSD sequence reconstruction and (b) FIL-MSD algorithm. The images use all possible cone opening angles. An opening angle upper threshold of $\Theta < 25^{\circ}$ was set for (c) and the same dataset was used with the FIL-MSD algorithm for (d).

pixel events with omitted pair-production. By choosing the first interaction to be the largest in the sequence, the computational time required to reconstruct events has also decreased substantially.

This technique has also increased the signal-to-noise ratio of the reconstructed Compton images. Experimental results, using a ^{22}Na source, show an almost two-fold increase in SNR. The new sequencing technique did, however, reconstruct images with a higher FWHM. This is due to the fact that FIL-MSD has a broader range of events that is correctly sequenced. Therefore, FIL-MSD sequences both high and low quality events whereas MSD tends to correctly sequence fewer low quality events. This discrepancy can be resolved by applying event cuts that artificially improve the angular resolution of the PSF.

4.6 Additional Image Analysis on Incorrect Sequencing

This appendix illustrates the image artifacts generated by incorrect sequencing and the advanced sequencing efficiency of FIL-MSD. This is done by reconstructing some of the MSD's sequenced events with FIL-MSD to yield an image with higher signal to noise. Similar to Fig. 4.9, where the small angle components reconstructed by MSD were isolated and re-sequenced with FIL-MSD, the same was completed with the ^{22}Na measurement and presented in Fig. 4.10. Fig. 4.10a-b are images that make use of all the data, whereas (c) displays the isolated low opening angle components which is then re-sequenced with FIL-MSD to produce (d). Opening angles above 25° using MSD are shown in (e) and re-sequenced with FIL-MSD in (f). The same is presented in Fig. 4.11 for a 2.2 MeV source.

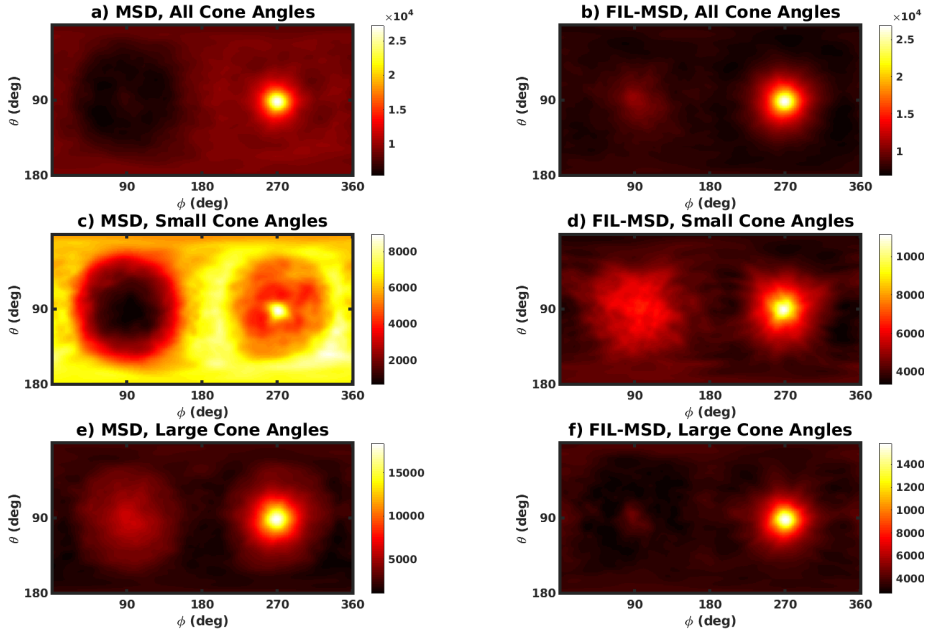

Figure 4.10: The left column represents events sequenced using the MSD algorithm for an ^{22}Na while the right column is sequenced with FIL-MSD . Different event cuts were performed on each row regarding the reconstructed scattering angle. The right column displays the re-sequenced events imaged by the left column. Therefore, the left and right columns display the same data just sequenced with different algorithms.

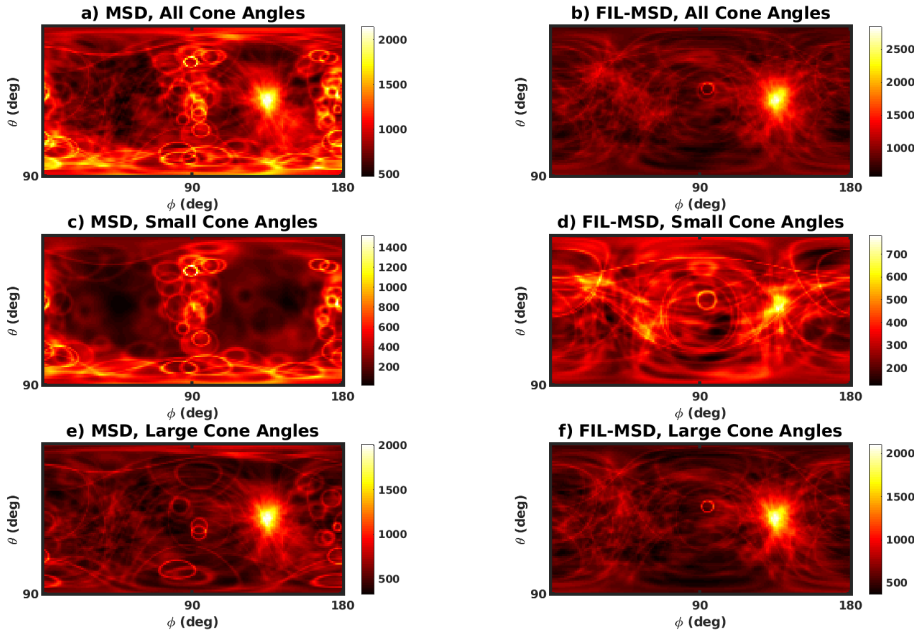

Figure 4.11: Experimental measurement, as displayed in Fig. 4.10, using a 2.2 MeV source.

CHAPTER V

Filtered Backprojection I: Deblurring in Spherical Harmonics With a Wiener Filter

Filtered backprojection offers an alternate image reconstruction technique to simple backprojection and is advantageous in scenarios where high resolution is desired while remaining computationally cheap. Since it is a linear process, it offers additional capabilities such as differential imaging, which is especially useful in high energy gamma-ray imaging, where continuum noise and artifacts are desired to be subtracted out. This chapter formalized the filtering process in spherical harmonics when using a Wiener filter. Chap. VI then discusses the development of a point spread function for 3-interaction events and applies it to simulated and experimental data.

5.1 Filtered Back Projection in Spherical Harmonics

This section serves as a continuation of Sec. 2.2.2. In reality, noise exists in the system and therefore the SBP image should be viewed as follows:

$$\hat{\mathbf{f}}_{\Omega}^{\text{sbp}} = \mathbf{B}\mathbf{f} + \boldsymbol{\nu}, \tag{5.1}$$

where $\boldsymbol{\nu}$ represents the noise term. We begin with the general FBP form:

$$\hat{\mathbf{f}}_{\Omega}^{\text{fbp}} = \mathbf{B}^{-1}\hat{\mathbf{f}}_{\Omega}^{\text{sbp}}. \tag{5.2}$$

If $\mathbf{B}^{-1}$ is a shift-invariant operation, then this can be seen as convolution of a filter with the SBP estimation:

$$\hat{f}_{\Omega}^{\text{fbp}} = g_{\Omega} \circledast \hat{f}_{\Omega}^{\text{sbp}}, \tag{5.3}$$

where g is a filter designed to deconvolve the detector blurring effects[1]. It is natural to use spherical harmonics[2] (SH) and their ability to define functions on a sphere, as introduced in the next section. To facilitate the convolution, we transform it to SH[3]:

$$\hat{F}_{lm}^{\text{fbp}} = \text{SHT}\left\{ g_{\Omega} \circledast \hat{f}_{\Omega}^{\text{sbp}} \right\} = \sqrt{\frac{4\pi}{2l+1}} G_{l,m=0} \hat{F}_{lm}^{\text{sbp}}, \tag{5.4}$$

where G_l is some filter in spherical harmonic space of degree (l). Capital symbols indicate the spherical harmonic transform of the spacial domain function. We note that there is a loss of order and one element becomes 'zonal' with all $m \neq 0$ components lost. This implies that convolution in SH is not commutative due to the properties of convolution on a sphere. Therefore, an assumption must be made that one of the elements is zonal and is rotational symmetric over north pole.

We use a Wiener filter [19] and takes the following form in SH:

$$G_l^{\text{Wiener}} = \frac{H_l^*}{\frac{(4\pi)^3}{2l+1} |H_l|^2 + \frac{N_l}{S_l}} = \frac{H_l^*}{\frac{(4\pi)^3}{2l+1} |H_l|^2 + R_l}, \tag{5.5}$$

where * denotes a complex conjugate and H_l is some impulse response, the PSF in this case. N_l and S_l represent the power spectral density of the noise and signal. Therefore, the fraction $\frac{N_l}{S_l}$, represented by R_l describes the inverse of the signal-to-noise ratio. Note that if zero noise is present, R_l will fall to zero and the Wiener filter will simplify to something that resembles the inverse of H_l, to within some constant factor. On the other hand, if R_l is very large, the Wiener filter will attenuate the frequency as such. Fig. 5.1 provides a high level simple block model of the entire process.

[1] Which can be b^{-1}, making g an inverse filter. However, this will result in a noisy image.
[2] There are also Fourier based techniques [57, 58].
[3] A derivation of convolution in SH is available in Theorem 1 in [59] and the appendix of [60]

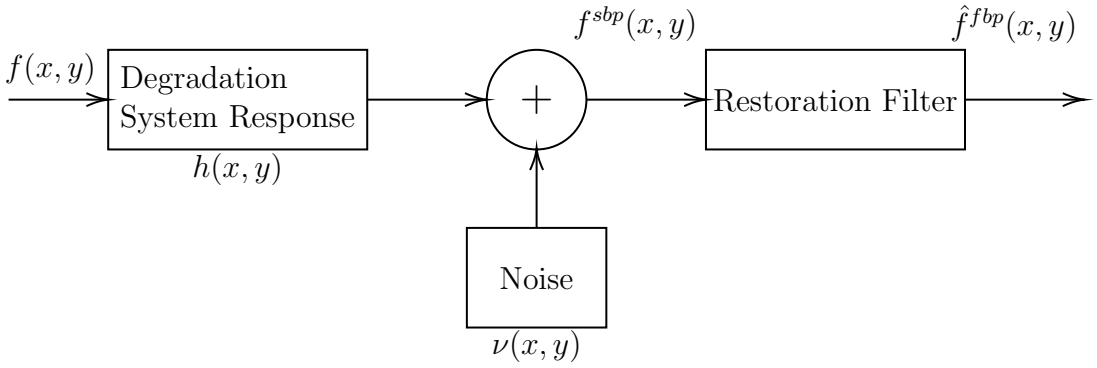

Figure 5.1: Block diagram representing the degradation and addition of noise due to the system, followed by a filter to restore the original signal.

5.1.1 Spherical Harmonics

Spherical harmonics are analogous to Fourier transforms in that a function $f(t)$ can be described with a Fourier series comprised of a set of orthogonal function. SH, on the other hand, describes a function $f(\Omega)$ defined on a 4π spherical surface with a set spherical harmonics. It can be described as such:

$$F_l^m = \int_\Omega \mathrm{d}\Omega f(\Omega) Y_l^{m*}(\Omega), \tag{5.6}$$

where Ω is in the $\Omega = (\theta, \phi)$ domain on a sphere. The inverse can be reconstructed as:

$$f(\Omega) = \sum_{l=0}^{\infty} \sum_{m=-l}^{l} F_l^m Y_l^m(\Omega), \tag{5.7}$$

where $Y_l^m(\Omega)$ represents the spherical harmonic basis functions, given in (5.8), with its complex conjugate represented by $Y_l^{m*}(\Omega)$. It is worth noting that there exists many different normalization [61], each with different properties.

$$Y_l^m(\Omega) = \sqrt{\frac{(2l+1)}{4\pi} \cdot \frac{(l-m)!}{(l+m)!}} P_l^m(\cos\theta) e^{im\phi}. \tag{5.8}$$

There are three main components to the SH. First, the square root term represents some normalization term[4]. The second part is the associated Legendre polynomials represented by $P_l^m(\cos\theta)$. The last component represents a complex exponential.

[4]To normalize the SH, we start with a generic SH: $Y_l^m(\Omega) = aP_l^m(\cos\theta)e^{im\phi}$. We normalize it to some desired factor I as $I = \langle Y_{l'm'} | Y_{lm} \rangle = \int_0^{2\pi} Y_{l'm'} Y_{lm}^* \sin\theta \mathrm{d}\theta \mathrm{d}\phi$ and solve for a, which is the normalization constant. a in this text represents the orthonormalized SH such that $I = \delta_{ll'}\delta_{mm'}$.

This gives us an opportunity to present $f(\Omega)$ on a sphere in terms of Legendre polynomials. Therefore, the PSF, which is the function of interest denoted by $h(\cos\omega)$, can be expanded to the sum of Legendre polynomials as such[5]:

$$f(\Omega) = h(\cos\omega) = \sum_{l=0}^{\infty} G_l P_l(\cos\omega), \tag{5.9}$$

where C_l represents the SH coefficient, which can be calculated by [62]:

$$G_l = \frac{2l+1}{2} \int_{-1}^{1} \mathrm{d}(\cos\omega) h(\cos\omega) P_l(\cos\omega). \tag{5.10}$$

In principle, the coefficients can be pre-calculated and stored in memory for quick deconvolution rather than requiring the calculation for each deconvolution instance.

5.2 Derivation of the Wiener Filter for Spherical Harmonics

This section derives the Wiener Filter [19] for deconvolution in spherical harmonic space. We begin with the following definitions:

$$\begin{aligned} o(\Omega) &= (x * h)(\Omega) + n(\Omega), \\ \hat{x}(\Omega) &= (o * g)(\Omega), \end{aligned} \tag{5.11}$$

where $x(\Omega)$ is the signal being measured, $h(\Omega)$ is the blurring impulse function, $n(\Omega)$ is noise[6], and $y(\Omega)$ is the observed spectra. The goal is to recover the signal via deconvolution with some filter $g(\Omega)$. The order of convolution is chosen such that the zonal spherical harmonic assumption of one of the elements is acceptable. This means that everything revolving around the filter is zonal, including the point spread function.

The Spherical Harmonic Transform (SHT) of a variable is denoted with capital

[5]We assume that the PSF is circularly symmetric around $\overrightarrow{Z}$.

[6]In Wiener filtering, we assume stationary signal and noise spectra. This is most definitely a false assumption to make in Compton imaging. See Fig. 9.1.

letters. Therefore, the SHT[7] of (5.11) is as follows

$$\begin{aligned} O_{lm} &= 2\pi\sqrt{\frac{4\pi}{2l+1}}H_l X_{lm} + N, \\ \hat{X}_{lm} &= 2\pi\sqrt{\frac{4\pi}{2l+1}}G_l O_{lm} = 2\pi\sqrt{\frac{4\pi}{2l+1}}G_l\left[2\pi\sqrt{\frac{4\pi}{2l+1}}H_l X_{lm} + N\right]. \end{aligned} \tag{5.12}$$

The objective of the Wiener filter is to estimate the original ($\hat{X}_{lm}$) with a filter that minimize the mean squared error:

$$MSE = \mathbb{E}\left[|x(\Omega) - \hat{x}(\Omega))|^2\right]. \tag{5.13}$$

Next, we utilize Parseval's Theorem [63] in SH [64],

$$\int_{\Omega} |f(\Omega)|^2 \, \mathrm{d}\Omega = \sum_{l=0}^{\infty} Q_l \sum_{m=-l}^{l} |F_{lm}|^2, \tag{5.14}$$

where Q_l is a factor that is dependant on the normalization of the spherical harmonics. In this work, we use the orthonormalized[8] SH and therefore $Q = 1$. A derivation of (5.14) is found in Sec. 5.3. For the steps to follow, we will use the following to reduce the variable traffic in this derivation:

$$T_l = 2\pi\sqrt{\frac{4\pi}{2l+1}}. \tag{5.15}$$

Therefore, the MSE in terms of (l, m) is:

$$\begin{aligned} &= \sum_{l=0}^{\infty}\left[Q_l\left|\sum_{m=-l}^{l} X_{lm} - \hat{X}_{lm}\right|^2\right] \\ &= \sum_{l=0}^{\infty}\left[Q_l\sum_{m=-l}^{l}|X_{lm}|^2 - X_{lm}\hat{X}_{lm}^* - X_{lm}^*\hat{X}_{lm} + |\hat{X}_{lm}|^2\right] \\ &= \sum_{l=0}^{\infty}\left[Q_l\sum_{m=-l}^{l}|X_{lm}|^2 - X_{lm}\left[T^2GHX_{lm} + TGN_{lm}\right]^* - X_{lm}^*\left[T^2GHX_{lm} + TGN_{lm}\right]\right. \\ &\qquad \left. + |T^2GHX_{lm} + TGN_{lm}|^2\right] \\ &= \sum_{l=0}^{\infty}\left[Q_l\sum_{m=-l}^{l}|X_{lm}|^2 - X_{lm}\left[T^2GHX_{lm} + TGN_{lm}\right]^* - X_{lm}^*\left[T^2GHX_{lm} + TGN_{lm}\right]\right. \\ &\qquad \left. + |T^2GHX_{lm}|^2 + TGHX_{lm}[TGN_{lm}]^* + [TGHX_{lm}]^*TGN_{lm} + |TGN_{lm}|^2\right] \end{aligned}$$

[7]The derivation of the SHT of a convolution is available in [59]

[8]The orthonormalized SH was chosen as it is the form chosen in the SHT library used in this study [65]. The orthonormalized SH has the following property: $\int_{\Omega} Y_{l'm'}^*(\Omega)Y_{lm}(\Omega)\mathrm{d}\Omega = \delta_{ll'}\delta_{mm'}$

we assume that the noise is independent of the signal,

$$\mathbb{E}\left[X_{lm}N_{lm}^*\right] = \mathbb{E}\left[X_{lm}^*N_{lm}\right] = 0,$$

and continue with the MSE derivation:

$$= \sum_{l=0}^{\infty}\left[Q_l\sum_{m=-l}^{l}|X_{lm}|^2 - X_{lm}\left[T^2GHX_{lm}\right]^* - X_{lm}^*\left[T^2GHX_{lm}\right] + |T^2GHX_{lm}|^2 + |TGN_{lm}|^2\right]$$

$$= \sum_{l=0}^{\infty}\left[Q_l\sum_{m=-l}^{l}\left[X_{lm} + [T^2GHX_{lm}]\right]\left[X_{lm} + [T^2GHX_{lm}]\right]^* + |TGN_{lm}|^2\right].$$

Let $S_l = Q_l\sum_{m=-l}^{l}|X_{lm}|^2$ and $V_l = Q_l\sum_{m=-l}^{l}|N_{lm}|^2$ represent the power spectrum for the signal and noise respectively. We remind ourselves that the objective of Wiener filter is to minimize the MSE. In this case, we will want to derive G_l such that it minimizes the MSE for a given l. This operation becomes tricky as several variables might be complex, including G_l. We therefore define the complex function $G_l = G_l^r + iG_l^i$ and take the derivative of the MSE derivation with respect to the real and complex parts set them equal to zero:

$$G_l^r = \frac{S_l\ \mathrm{Re}\left\{H_l\right\}}{T^2H^2S_l + V_l},$$
$$G_l^i = -\frac{S_l\ \mathrm{Im}\left\{H_l\right\}}{T^2H^2S_l + V_l}.$$

We therefore can solve for the final Wiener filter in spherical harmonics by adding the real and complex component:

$$G_l = \frac{H_l^*}{\frac{2(2\pi)^3}{2l+1}|H_l|^2 + \mathrm{SNR}_l^{-1}}, \tag{5.16}$$

with $\mathrm{SNR}_l = \frac{S_l}{N_l}$.

5.3 Parseval's Theorem in Spherical Harmonics

Parseval's theorem proves that the energy in Fourier space is equivalent to the energy in time domain:

$$\int_{-\infty}^{\infty}|g(t)|^2\,\mathrm{d}t = \int_{-\infty}^{\infty}|G(f)|^2\,\mathrm{d}f, \tag{5.17}$$

where $g(t)$ is some signal and $G(f)$ is its Fourier transform. This, however, slightly differs for SH and the chosen normalization. Lets start with the integral of the square

of the function divided with the area it spans and calculate to find the SH equivalent:

$$\frac{1}{4\pi}\int_{\Omega}|f(\Omega)|^2\,\mathrm{d}\Omega \tag{5.18}$$

We use (5.7) for the following derivation:

$$\begin{aligned}
&\frac{1}{4\pi}\int_{\Omega}|f(\Omega)|^2\,\mathrm{d}\Omega = \frac{1}{4\pi}\int_{\Omega}\left|\sum_{l=0}^{\infty}\sum_{m=-l}^{l}F_{lm}Y_{lm}(\Omega)\right|^2\mathrm{d}\Omega\\
&= \frac{1}{4\pi}\int_{\Omega}\left|\sum_{l=0}^{\infty}F_{l,-l}Y_{l,-l}+F_{l,-l+1}Y_{l,-l+1}+F_{l,-l+2}Y_{l,-l+2}+\cdots+F_{l,l}Y_{l,l}\right|^2\mathrm{d}\Omega\\
&= \frac{1}{4\pi}\int_{\Omega}\left|F_{0,0}Y_{0,0}+F_{1,-1}Y_{1,-1}+F_{1,0}Y_{1,0}+F_{1,1}Y_{1,1}+\cdots+F_{l,l}Y_{l,l}\right|^2\mathrm{d}\Omega.
\end{aligned}$$

Next, we expand the quadratic and remind ourselves of the following orthogonality identity

$$\int_{\Omega}Y^*_{l'm'}(\Omega)Y_{lm}(\Omega)\mathrm{d}\Omega = Q(l)\delta_{ll'}\delta_{mm'}, \tag{5.19}$$

where Q is a factor that depends on the chosen SH normalization. Therefore, for all elements $l' \neq l$ and $m' \neq m$ will be zeroed (as they are all orthogonal). All we are left with is:

$$\begin{aligned}
&= \frac{1}{4\pi}\left[QF^2_{0,0}+QF^2_{1,-1}+QF^2_{1,0}+QF^2_{1,1}+\cdots\right]\\
&= \frac{1}{4\pi}\sum_{l=0}^{\infty}Q_l\sum_{m=-l}^{l}|F_{lm}|^2\,.
\end{aligned}$$

Therefore, Parseval's theorem for SH is as follows:

$$\int_{\Omega}|f(\Omega)|^2\,\mathrm{d}\Omega = \sum_{l=0}^{\infty}Q_l\sum_{m=-l}^{l}|F_{lm}|^2\,. \tag{5.20}$$

As mentioned before, we use the orthonormalized SH[9] and therefore $Q = 1$.

[9]Attention needs to be given here, as some SH normalizations contain a frequency component i.e. the Schmidt semi-normalization where $Q = \frac{2\pi}{2l+1}$

CHAPTER VI

Filtered Backprojection II: Point Spread Function Modeling for 3-Interaction Events

Basko et al. developed an analytical inversion method to reconstruct Compton images via spherical harmonics [66]. Parra [60] then extended the model to use all possible scattering angles with the Klein-Nishina formula taken into account. This however did not consider that the Compton camera is unlikely to detect the entire set of scatter angles. Therefore, Parra's technique was augmented by Tomitani and Hirasawa [67] to limit the angles of the analytical point spread function (PSF). They then further developed the model by compensating for angular uncertainty due to energy uncertainty [68]. Later, Xu and He [62] modeled the missequencing effect for 2-interaction events into the analytical PSF. This is followed by Chu's [17] simplification which aimed to decouple the physics and mathematical effects by weighting each Compton cone by the probability of it occurring.

This work develops an analytical PSF for 3-interaction events with a specific application to high-energy gamma-ray imaging and formalizing an approach for filtering in spherical harmonics. First, the analytical PSF model is developed by analyzing the different missequencing components presented in Sec. 6.1. It is then applied in a Wiener filter that was derived in Chap. V using simulated and experimental data. The results are presented in Secs. 6.3-6.4.

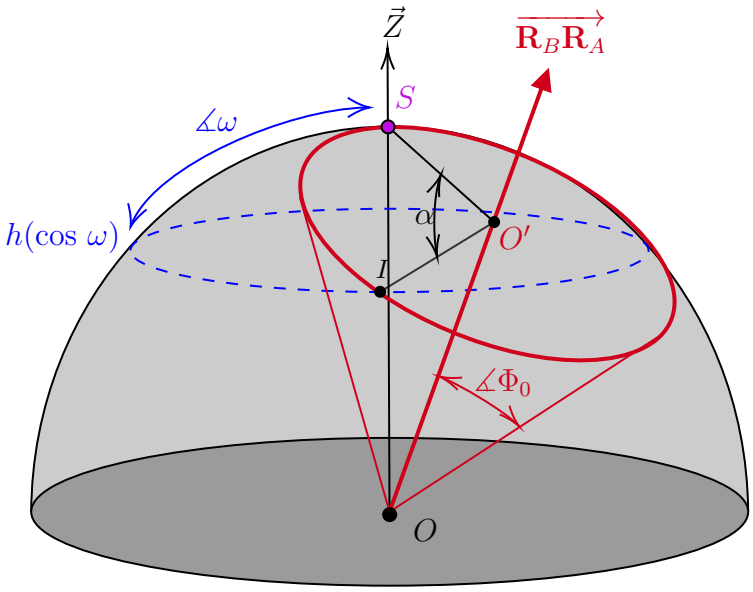

Figure 6.1: The contribution of the Compton cone (red) projected onto a spherical space with opening half angle Φ_0. The true source location is denoted by S and is set along Z.

6.1 Modeling of Point Spread Function

Modeling the PSF involves calculating the contribution of the Compton cone to the image space from a point source. In this section, we model the PSF for 3-interaction events when using the FIL-MSD sequencing algorithm. A visualization of the modeling process is presented in Fig. 6.1. There, a Compton cone (red) is projected onto a unit sphere. It can be assumed that the response is symmetric around $\overrightarrow{Z}$. Therefore, the PSF can be sampled with angle ω, which is the angle away from the true source location ($\overrightarrow{Z}$).

A cone with opening angle (Φ) that is normalized with $1/\sin\theta$ intersects the unit sphere on ω at angle α. Therefore, the contribution to the PSF at ω is proportional

to $\mathrm{d}\alpha/\sin\theta$. The summation of all opening cone angles to the PSF at $\omega + \mathrm{d}\omega$ is then:

$$\begin{aligned} h(\cos\omega)\mathrm{d}\omega\ 2\pi\sin\omega &= \int_0^{2\pi}\mathrm{d}\phi\int_0^{\pi}\mathrm{d}\theta\ \xi(\theta)K(\theta)\sin\theta\mathrm{d}\alpha \\ &= 2\pi\int_0^{\pi}\mathrm{d}\theta\ \xi(\theta)K(\theta)\sin\theta\mathrm{d}\alpha, \end{aligned} \tag{6.1}$$

where $\xi(\theta)$ is some weighting factor, $1/\sin\theta$ in this case[1]. The left hand side of the equation can be seen as the $h(\cos\omega)$ ring width ($\mathrm{d}\omega$) times the circumference of the ring ($2\pi\sin\omega$). On the other hand, we measure the Compton ring with opening angle θ that contributes to the $h(\cos\omega)$ PSF with $\xi(\theta)K(\theta)\sin\theta\mathrm{d}\alpha$.

(6.1) is then re-arranged to the following:

$$h(\cos\omega) = \int_0^{\pi}\mathrm{d}\theta K(\theta)\frac{1}{\sin\omega}\frac{\mathrm{d}\alpha}{\mathrm{d}\omega}. \tag{6.2}$$

The quantity $\frac{\mathrm{d}\alpha}{\mathrm{d}\omega}$ can be calculated by measuring the angle α, shown in Fig. 6.1, formed by the triangle $SO'I$. Using the law of cosines, we can calculate for the quantity:

$$\|SI\|^2 = \|O'S\|^2 + \|O'I\|^2 - 2\,\|O'S\|\,\|O'I\|\cos\alpha, \tag{6.3}$$

where $\|O'I\| = \|O'A\| = \sin\theta$ and $\|O'I\| = \sin\frac{\omega}{2}$. We can therefore calculate the expression for α and its derivative as follows:

$$\begin{aligned} \cos\alpha &= 1 - \frac{2\sin^2\frac{\omega}{2}}{\sin^2\theta}, \\ \frac{\mathrm{d}\alpha}{\mathrm{d}\omega} &= \frac{\cos\frac{\omega}{2}}{\sqrt{\cos^2\frac{\omega}{2} - \cos^2\theta}}. \end{aligned} \tag{6.4}$$

We insert this into (6.2) and result in the general form:

$$h(\cos\omega) = \int_0^{\pi}\mathrm{d}\theta K(\theta)\frac{1}{\sin\omega}\frac{\cos\frac{\omega}{2}}{\sqrt{\cos^2\frac{\omega}{2} - \cos^2\theta}}. \tag{6.5}$$

This models the contribution to the PSF by cones with all opening angles, weighted by the Klein-Nishina cross section, and forms the basic structure to model the PSF.

However, this model only accounts for events that are correctly sequenced. Due to the limited time resolution of the detector system, the timing between successive interactions cannot be resolved. When an event is missequenced, it augments the

[1]Chu models $\xi(\theta) = \frac{\sin\theta}{K(\theta)}$, and weights each ring as such, to decouple the physics from the filter [17]. Chu then models the PSF as a Newtonian potential, which is essentially Parra's model without the Klein-Nishina cross section. In the case of this work, the physics is modeled in the PSF.

point spread function. The next section investigates the distribution of missequenced 3-interaction events followed by the derivation of their PSFs using the notations in Table 6.1.

Table 6.1: Notation used in Chapter VI

Symbol	Description
ω	Angle to the true source location
$[0, \omega^*]$	Declared range of angles where FIL-MSD will fail
ν	Angle to the source's antipode $(\pi - \omega)$
α	Angle between points S, O', I
Φ_i	Reconstructed half angle of the cone opening for sequence i
i	Angle between points
$A, B, C...$	Alphabetic indexing to denote true succession in a sequence
$1, 2, 3...$	Numerical indexing to denote the succession for sequence index i
θ_A, θ_B	Scattering angle of interaction A and B respectively
$K(\theta)$	Differential Klein-Nishina cross section at scattering angle θ
E_O	Energy of the incident gamma ray
$m_e c^2$	Energy of an electron at rest (511 keV)
$h(\cos\omega)$	The point spread function (PSF) as a function of ω
FIL	First interaction is largest
$\overrightarrow{R}_A, \overrightarrow{R}_B, \overrightarrow{R}_C$	Location of interactions A, B, C

6.1.1 Distribution of Sequence Indices

Before diving deeper into modeling, we perform a Geant4 simulation to investigate the distribution of event sequences. Each sequence order is given an index, and since we limit this study to only 3-interaction events, the indices range from 0-5. Index 0 represents the correctly sequenced events, while index 1 missequences the first and second interaction, and index 2 missequences the second and third. The sequence indexing of interaction succession are presented in Table 6.2.

Fig. 6.2 shows the index distribution for a 2.6 MeV source using the MSD and FIL-MSD sequencing algorithms. Naturally, as presented in Chapter IV, FIL-MSD has a larger fraction of index 0. However, unlike MSD, index 1 presents the largest missequenced index followed by 2 then 3. MSD has a rather uniform distribution

Table 6.2: Table of sequence indices and their corresponding interaction order.

Sequencing Order Index	Reconstruction Order
0	ABC
1	BAC
2	ACB
3	BCA
4	CAB
5	CBA

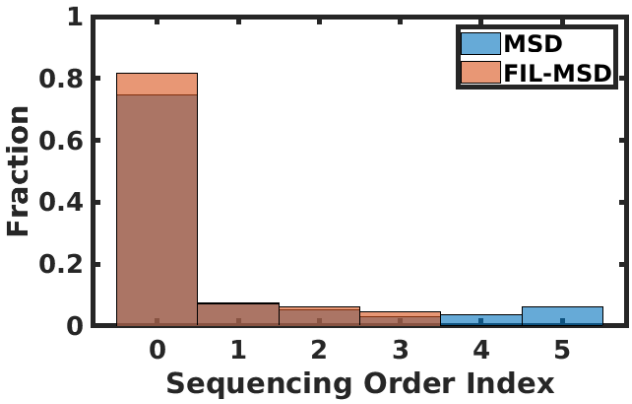

Figure 6.2: Simulated distribution

among the indices. However, the focus of this study revolves around the FIL-MSD algorithms and the following analysis is limited to such.

For the general interest to the reader, the distribution of sequenced opening angles is displayed in Fig. 6.3. The true distribution displays a semi-sinusoidal distribution centered at around 90°, while MSD creates a large number of small angle scatters. FIL-MSD keeps a very similar distribution to that of the true one, but missequences the small angle scattering events.

6.1.2 Sequencing Case Zero

This subsection discusses the contribution of the correctly sequenced events (with index 0) to the overall PSF. A toy model is presented in Fig. 6.4. FIL-MSD slightly simplifies the modeling process, as we know the majority of missequences arise from small angle scattering. These events are however in the minority as they have a smaller

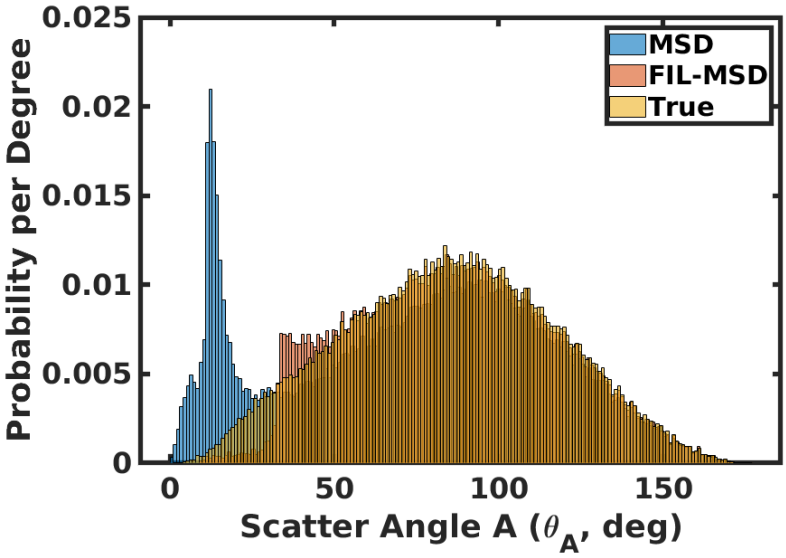

Figure 6.3: Simulated angle distribution

probability of detection as the scattered gamma-ray still has a large energy and is likely to escape the detector.

The critical angle of when FIL-MSD begins to fail, which we will define with ω^*, is of interest as it will dictate the bounds of integration for (6.5). Unlike 'Simple-Comparison' for two-pixel events, there is no direct method of calculating ω^* due to the complexity when dealing with the third interaction. When, $E_A \geq E_0/2$, the interaction is definitely FIL as there is not enough energy left in E'_A to create an FIL

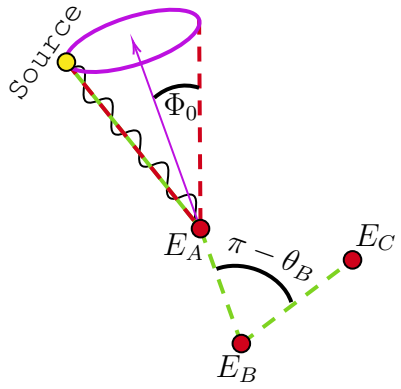

Figure 6.4: Index 0 toy model

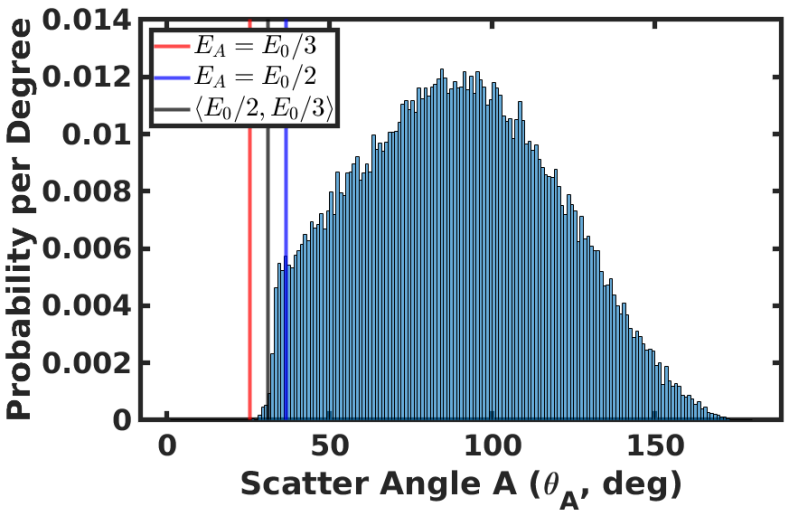

Figure 6.5: The distribution of scatter angles (Φ_0), or events that were correctly sequenced by FIL-MSD.

event. However, as shown in Sec 4.2.2, an FIL event can occur in lower energies down to $E_A \geq E_0/3$, although not guaranteed. For example $E_A = 0.4E_0$ can still be an FIL if $E_B = E_C = 0.3E_0$. However, it is not FIL if $E_B = 0.1E_0$ & $E_C = 0.5E_0$. Therefore, a quick simulation of the events which are missequenced is completed with the results presented in Fig. 6.5.

The plot is annotated with the angles as calculated when $E_A = E_0/2$ or $E_0/3$ and the angle calculated when the two energies are averaged. Looking at the distribution, the falloff is very close to the angle calculated by the average energy. Therefore, we define the critical angle as:

$$\omega^* = \frac{\Phi(E_0/2) + \Phi(E_0/3)}{2}, \tag{6.6}$$

where the opening angle $\Phi(E)$ is given by:

$$\Phi(E_{\text{dep}}) = \arccos 1 - \frac{m_e c^2 E_{\text{dep}}}{E_0(E_0 - E_{\text{dep}})}. \tag{6.7}$$

The model for the correctly sequenced components can then be created by extending Parra's model by limiting the bounds as follows:

$$h_{case\ 0}(\cos\omega) = \int_0^\pi \mathrm{d}\theta K'(\theta) \frac{1}{\sin\omega} \frac{\cos\frac{\omega}{2}}{\sqrt{\cos^2\frac{\omega}{2} - \cos^2\theta}}, \tag{6.8}$$

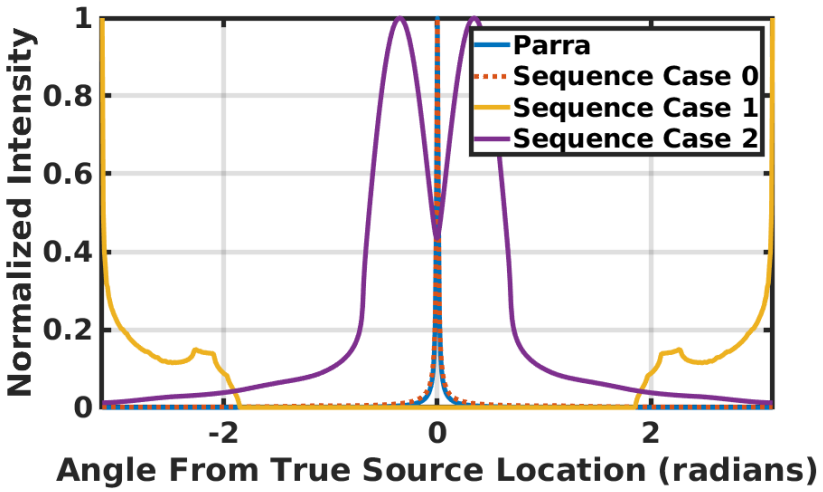

Figure 6.6: Plots of the different PSF components resulting from sequencing cases 0-2 compared to Parra's PSF which assumes no missequencing. All components were normalized to their max intensity.

where

$$K'(\theta) = \begin{cases} K(\theta) & \theta \in (\omega^*, \pi) \\ 0 & else \end{cases} . \tag{6.9}$$

The numerically calculated solution to (6.8) is plotted in Fig. 6.6, labeled by 'Sequence Index 0', and is compared to the 'Parra' derivation. The simulated simple backprojection of this can be seen in Fig. 6.7. A slight peak is seen in the antipode[2] of the peak. This is due to the events that scattered at 90° which results in Compton cones that are longitudinal-like, and therefore develops hotspots at the north and south pole. If only 90° scatters occur, one would not be able to differentiate the two hotspots to identify the true source location.

6.1.3 Sequencing Case One

Index 1 missequences the first and second interaction (BAC), which therefore sequenced interaction B first ($E_1 = E_B$). The simple backprojection is presented in Fig. 6.8.

[2]The antipode of point is a spot on a sphere that is diametrically opposite it. For example, the antipode of Shanghai, China is Los Charrias, Argentina.

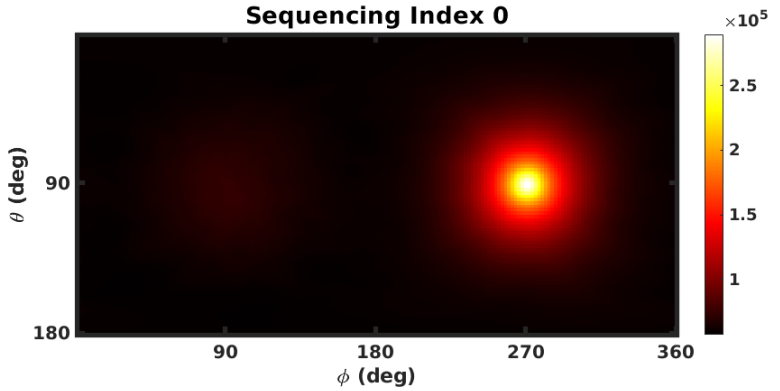

Figure 6.7: Simple backprojection of a simulated 2.6 MeV source, located at $(\phi, \theta) = (270, 90)$, when only using correctly sequenced events provided by FIL-MSD.

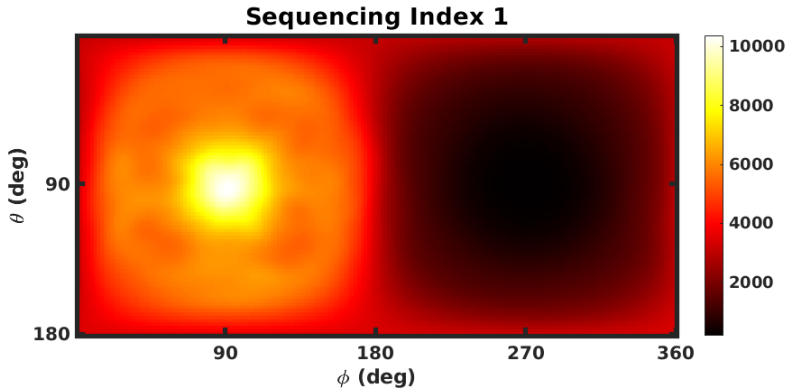

Figure 6.8: Simple backprojection of 2.6 MeV source, located at $(\phi, \theta) = (270, 90)$, when only using index 1 sequenced events provided by FIL-MSD. Note that the hotspot of the reconstruction is located at the antipode of the true source location.

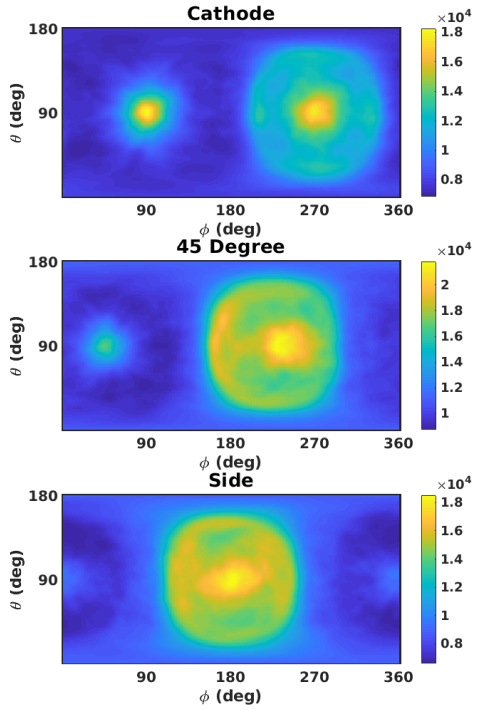

Figure 6.9: Different simple backprojection of 2.6 MeV source when the source is located at a) $(\phi, \theta) = (90, 90)$, b) $(\phi, \theta) = (45, 90)$, and c) $(\phi, \theta) = (0, 90)$, when only using incorrect sequenced events provided by FIL-MSD. The hotspot of the reconstruction is always located at the antipode of the true source location due to sequencing case 1. Note the coordinate change, in this plot, the cathode is located at $(\phi, \theta) = (90, 90)$.

What is interesting is that the hotspot is always located at the antipode of the true source location. In Fig. 6.9, simple backprojection images of different source location show the correlated shifting of the hotspot with the true source location. This is due to the physical kinematic nature of the gamma ray.

The toy model is illustrated in Fig. 6.10 in order to aid the reader with visualizing the event. There, the missequencing results in a lever arm of $\overrightarrow{R_A R_B}$ that is anti-parallel to Sequence 0's lever arm.

Next, the reconstructed opening angle Φ_1 is investigated with the following derivation:

$$\cos\Phi_1 = 1 + \frac{m_e c^2}{E_O} - \frac{m_e c^2}{E_A + E_C}. \tag{6.10}$$

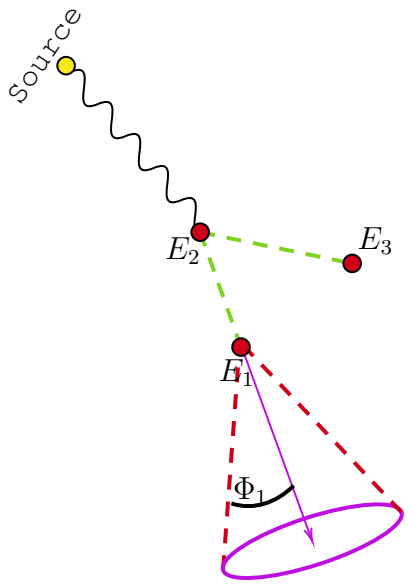

Figure 6.10: Index 1 toy model

Since we assume a full energy deposition, then $E_O = E_A + E_B + E_C$. Unlike Dr. Xu's derivation, we are negotiating a 3rd interaction that originated from interaction B where the gamma ray scattered there at an angle of θ_B. Therefore, the 3rd interaction will have an energy

$$E_C = E_O - E_A - \frac{E_A}{1 + \frac{E_A}{m_e c^2}(1 - \cos\theta_B)}, \tag{6.11}$$

where E_A has energy

$$E_A = E_O - \frac{E_O}{1 + \frac{E_O}{m_e c^2}(1 - \cos\theta_A)}. \tag{6.12}$$

So, inserting (6.11) and (6.12) into (6.10), the form for Φ_1 can be put into:

$$\cos\Phi_1 = \frac{E_O\cos(\theta_A)Q + (m_e c^2 + E_O)\left(\cos(\theta_B)\left(m_e c^2 - E_O\right) + 2E_O\right) + E_O^2\cos^2(\theta_A)}{2m_e c^2 + E_O\cos(\theta_A)Q + 2m_e c^2 E_O + E_O^2\cos^2(\theta_A) - E_O^2\cos(\theta_B) + 2E_O^2} \tag{6.13}$$

with $Q = (-2m_e c^2 + E_O\cos(\theta_B) - 3E_O)$. Now, the the opening angle of the misse-quenced event can be calculated in terms of θ_A and θ_B. We can investigate the effects that the scatter angels have on Φ_1 with Fig. 6.11. The region where case 1 occurs is bounded within the green horizontal lines. Upon closer inspection, the contour lines are very lateral near larger θ_B angles, which implies little variance in reconstructed

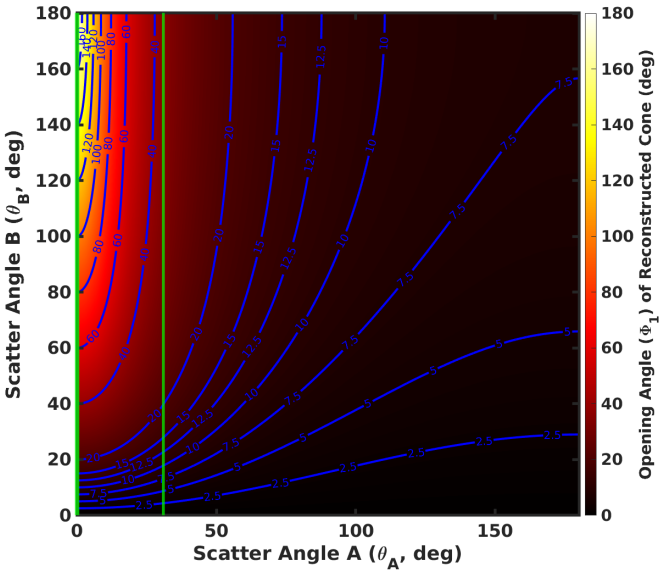

Figure 6.11: Φ_1 value for different θ_A and θ_B scattering with a contour plot overlaid. The green horizontal lines represents the bounds $\theta_A = (0, \omega^*)$, which is the region where FIL-MSD is most likely to fail.

opening angles due to the second scatter angle. Moreover, near the ω^* boundary, the reconstructed angle Φ_1 is very similar to θ_A, which is the true scatter angle. This results in the correct cone being reconstructed, just projected 180° from the true source location, resulting in a hotspot at the source's antipode as shown in Fig. 6.8 and 6.9.

6.1.3.1 Geometric Modeling of Case One Missequencing

Next, the contribution of the case 1 cones to the overall PSF can be accomplished by modifying Xu's missequencing solution [26]. First, a representation of the event is illustrated in Fig. 6.12. There, the cone is projected with a lever arm in direction $\overrightarrow{\mathbf{R}_A\mathbf{R}_B}$ with an opening angle Φ_1, in the opposite direction of that in case 0. To simplify the modeling process, a new variable[3] is defined that represents the angle from the source's antipode $\nu = \pi - \omega$.

[3]I believe that Xu et al. [26, 62] have made an error in defining the bounds here. They chose to model the missequenced cone relative to the correctly sequenced lever arms, which results in a distribution that is $\pi - \omega$.

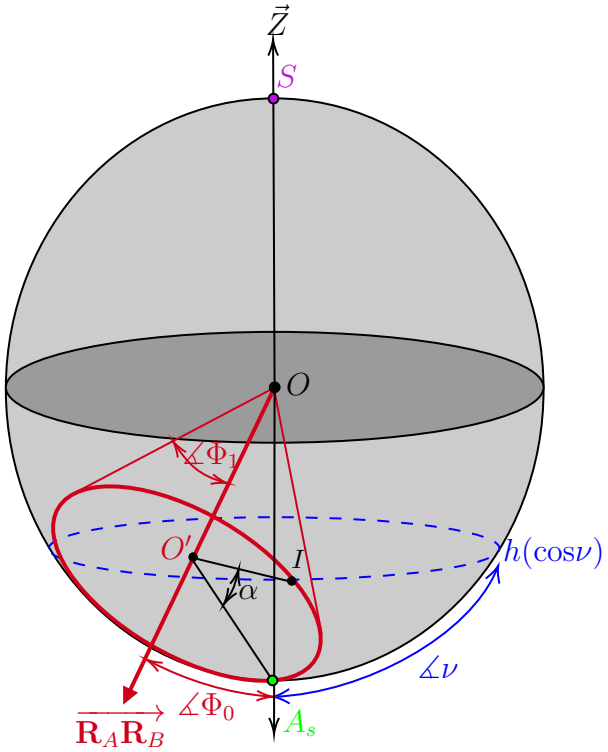

Figure 6.12: Missequenced cone projection

Similarly to Sec. 6.1.2, the contribution of the ring will be symbolized by $\frac{\mathrm{d}\alpha}{\mathrm{d}\nu}$ and will then be used in the base model (6.5). To calculate the contribution, we use the points A, O', I, which is the intersection of the ring and $h(\cos\nu)$ at angle ν. The source's antipode is represented by A_S. In that triangle, $\|O'I\| = \sin\Phi_0$, $\|O'A_S\| = \sin\Phi_1$, and $\|IA_S\| = 2\sin\frac{\nu}{2}$. Using the law of cosines:

$$\|A_SI\|^2 = \|O'A_S\|^2 + \|O'I\|^2 - 2\,\|O'A_S\|\,\|O'I\|\cos\alpha, \tag{6.14}$$

we can arrive at an expression for α:

$$\cos(\alpha) = \frac{\sin^2(\Phi_0) + \sin^2(\Phi_2) - 4\sin^2(\frac{\nu}{2})}{2\sin(\Phi_0)\sin(\Phi_2)}. \tag{6.15}$$

Next, a differential with respect to ν is taken:

$$\frac{\mathrm{d}\alpha}{\mathrm{d}\nu} = \frac{2\sin\nu}{\sqrt{4\sin^2\Phi_0\sin^2\Phi_1 - \left(\sin^2\Phi_0 + \sin^2\Phi_1 - 4\sin^2\frac{\nu}{2}\right)^2}}. \tag{6.16}$$

In this model, $\Phi_0 = \theta_A$, and $\sin^2(\Phi_1)$ can be expressed as $1 - \cos^2(\Phi_1)$.[4,5] Inserting

[4] $\cos^2(\Phi_1)$ is defined in (6.13)

[5] We use the identity $\sin^2(\Phi_1) + \cos^2(\Phi_1) = 1$ here.

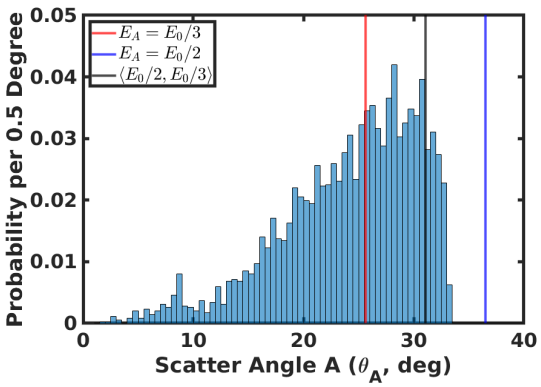

Figure 6.13: Distribution of the true scatter angles ($\Phi_0 = \theta_A$) which are missequenced to case 1 by FIL-MSD. The vertical lines represent the angles which sequence E_A first. $\langle E_0/2, E_0/3 \rangle$ represents the average of the two values, or ω^*, and is plotted in black.

(6.16) into (6.5) results in the expression for the case 1 PSF:

$$\begin{aligned} h_{\text{case 1}}(\cos\omega) &= \int_0^{\omega^*} \mathrm{d}\theta_a K(\theta_a) \int_0^{\pi} \mathrm{d}\theta_b \frac{1}{\sin\nu}\frac{\mathrm{d}\alpha}{\mathrm{d}\nu} \\ &= \int_0^{\omega^*} \mathrm{d}\theta_a \; 2K(\theta_a) \int_0^{\pi} \frac{\mathrm{d}\theta_b}{\sqrt{4\sin^2\theta_a f(\theta_a,\theta_b) - \left(\sin^2\theta_a + f(\theta_a,\theta_b) - 4\sin^2\frac{\nu}{2}\right)^2}}, \end{aligned} \tag{6.17}$$

where $f(\theta_a, \theta_b) = \sin^2\Phi_1$. Justification for using ω^* in the $\mathrm{d}\theta_A$ integral is given in Fig. 6.13, which plots all the true scatter angles Φ_0 which were missequenced to case 1. Naturally, FIL-MSD will fail with small angle scatters, but the upper limit is not hard bounded, as discussed in Sec. 6.1.2. In the plot, ω^* (outlined in black) proves to be a good approximation for the distribution's fall off.

There is also an opportunity to add the Klein-Nishina cross-section for scatter θ_B when integrated over that angle. However, experimentation with the addition of cross-section resulted in a poor model. This is due to effects such as detector geometry that augments the distribution of detected scatter angles from the Klein-Nishina. Fig. 6.14 plots the interaction cross section for any given two scatter set, which presents the most probable event resulting from two small angle scatters. This however, does not represent the detector response as two small angle scatters would result in a gamma ray that has most of its original energy, and therefore most likely escape the detector.

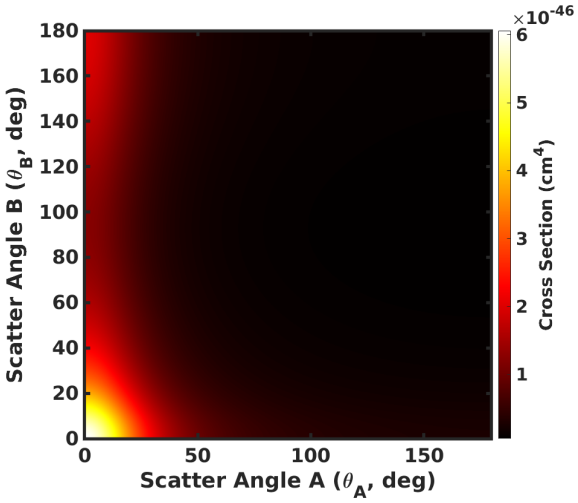

Figure 6.14: Heat map representing the interaction cross section for an event with scatters θ_A and θ_B.

This can be seen in Fig. 6.15 which plots the detector distribution with their respective scatter angles showing that the small angle scatter region has a low probability of occurrence. Comparing Fig. 6.14 and 6.15 demonstrates the mismatch in model and therefore a decision was made not to include the distribution of the scatter angle.

(6.17) can now be numerically solved and results in a distribution plotted in Fig. 6.16. In the figure, the modeled PSF is compared to the PSF from a simple backprojection image, or the azimuthal cross section through the hotspot of Fig. 6.8. The two curves contain similar features in that they present a peak near the source's antipode and a shoulder near $|\omega| = 2$. The case 1 PSF is plotted along with the other components in Fig. 6.6.

6.1.4 Sequencing Case Two

Case two missequences the 2nd and 3rd interaction (ACB) and presents an interesting case as the first interaction is sequenced correctly thereby resulting in a correctly calculated opening angle ($\Phi_0 = \Phi_2 = \theta_A$). This is illustrated in Fig. 6.17.

Moreover, when only case two sequences are projected, as done in Fig. 6.18, a

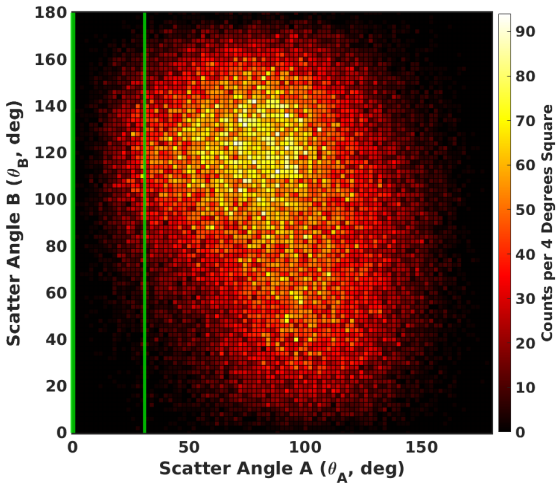

Figure 6.15: Distribution of events with scatters θ_A and θ_B. The vertical green lines bound the region which FIL-MSD fails and results in sequencing case 1.

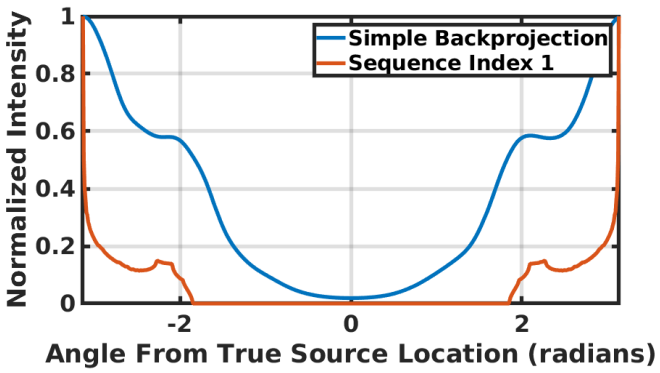

Figure 6.16: Point spread function of sequencing case 0 for a simple backprojection and a modeled PSF. Note that the modeled PSF is not Gaussian blurred, while the SBP is.

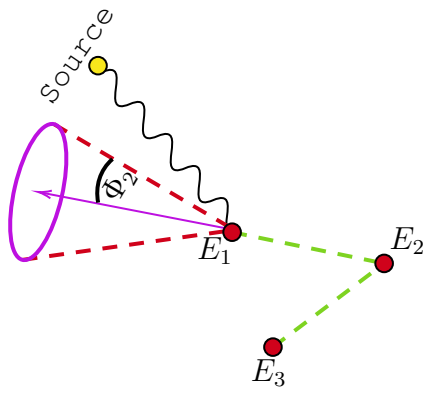

Figure 6.17: Index 2 toy model

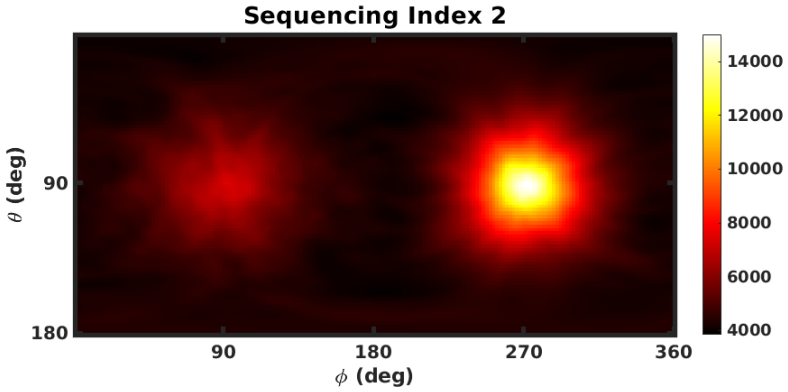

Figure 6.18: SBP of events sequenced as case 2. The true source location is located at $(\phi, \theta) = (270, 90)$. Therefore, the hotspot is located at the true source location.

hotspot in the true source's location is developed. To verify that this is not an artifact of some tertiary nature, a simulation of sources in different location is completed to display the shift of the reconstructed hotspot with the true source location. This is shown in Fig. 6.19a where the hotspot is located at the true source location, shown in Fig. 6.19b.

The origin of this phenomena is related to the underlying kinematics occurring in the event. After the second scatter, on average, the resulting gamma ray has very little energy and tends to travel a very small distance. To illustrate the effect this has on the reconstruction, the distribution of angles measured between $\measuredangle R_B R_A R_C$ is histogrammed in Fig. 6.20 showing a centroid at around 20°. This implies that

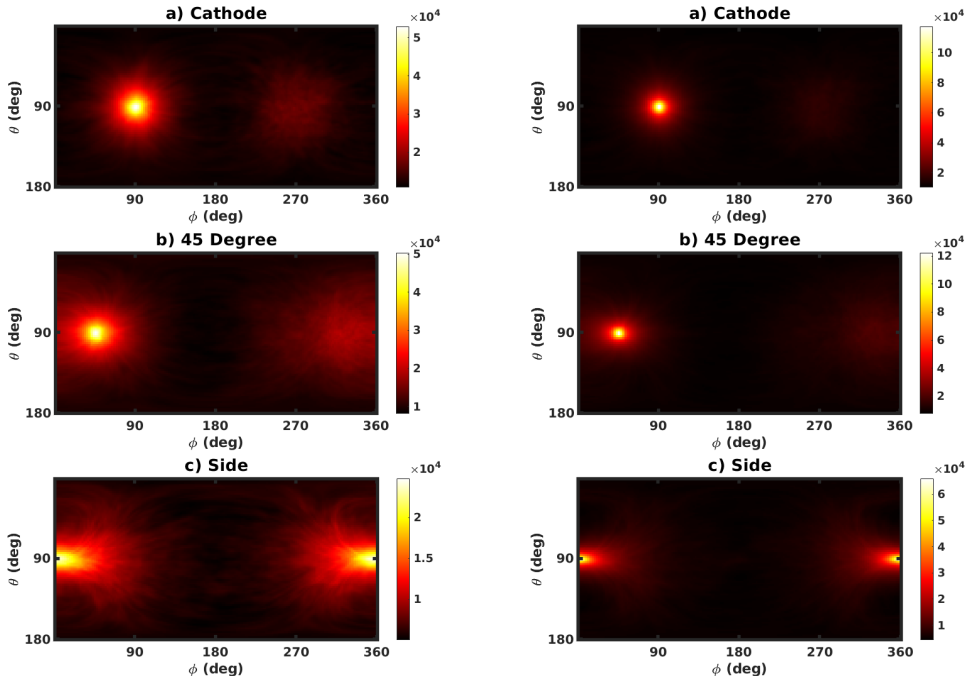

(a) Events sequenced as case two (b) Events in (a) re-sequenced to case 0

Figure 6.19: Two cases of sequencing using the same set of events: (a) when sequenced as case two while (b) sequencing them the correct order. This figure aims to demonstrate the nature of sequencing case 2 and how it is correlated with the true source location.

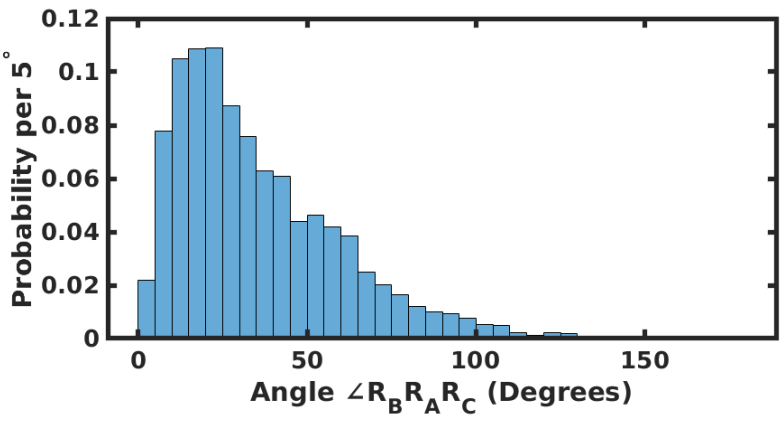

Figure 6.20: Distribution of angles $\measuredangle R_B R_A R_C$ for a simulated 2.6 MeV gamma-ray source. This distribution governs the deflection of the cone lever arms.

the correct cone projection will be affect by a deflected lever arm governed by that distribution. The fact that the distribution's mode proves to be a small number results in a cone that is correlated with the true source location, but with a slight blur rather than a cone that is directed in a random direction.

Therefore, the PSF for case two can be modeled by blurring the PSF of case zero with the distribution presented in Fig. 6.20. We expand the model presented in (6.8):

$$h_{case\ 2}(\cos\omega) = \chi(\omega) * \int_0^{\pi} \mathrm{d}\theta K'(\theta) \frac{1}{\sin\omega} \frac{\cos\frac{\omega}{2}}{\sqrt{\cos^2\frac{\omega}{2} - \cos^2\theta}}, \tag{6.18}$$

where the $K'(\theta)$ is the same as (6.9). No characteristics or correlation between the events missequenced case two could be found to narrow the integration. Therefore, the bounds remain similar to case zero as $\theta \in (0, \omega^*)$ results in case one. The convolution with χ aims to blur with the angle deflection response case 2. To simplify the process, a cosine fit was made to the distribution presented in Fig. 6.20 centered at 20° and a period of 160° to stand in for $\chi(\omega)$. The PSF in (6.18) results in a distribution plotted in Fig. 6.6. The binomial nature of the PSF is reduced when it is Gaussian blurred once more, which is discussed in Sec. 6.1.7.

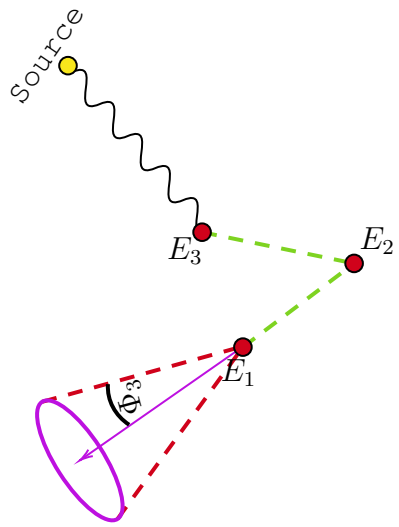

Figure 6.21: Index 3 toy model

6.1.5 Sequencing Case 3 and Other Cases

The other sequencing cases not addressed in this study consist of 3, 4, and 5. Case 3, as illustrated in Fig. 6.21, is sequenced in the order BCA. It rather difficult to model the vector $\overrightarrow{R_C R_B}$ with respect to $\overrightarrow{R_B R_A}$. Naturally, it could be done via simulation, but is disregarded here in the spirit of maintaining an analytical format. Cases 4 and 5 are neglected as they consist of less than 3% of the simulated events, as shown in Fig. 6.2

6.1.6 PSF for 3+ Interaction Events

For a given N-interaction sequence, there are $N!$ permutations, which complexifies any modeling effort. Case 1 sequencing of the modeling can be expanded to include more interactions as follows:

$$h_{\text{case 1}}(\cos\omega) = \int_0^{\omega^*} \mathrm{d}\theta_A K(\theta_A) \iint_{\mathbf{R}^{N-2}} \mathrm{d}T \frac{1}{\sin\nu} \frac{\mathrm{d}\alpha}{\mathrm{d}\nu}, \tag{6.19}$$

which extends (6.17) to include multiple dimensions of $\mathrm{d}\theta_i$ and $\mathrm{d}T = \mathrm{d}\theta_B \ldots \mathrm{d}\theta_N$.

However, sequence case 1 does not represent the most common missequenced case. Therefore further analysis is required to account for all $N!$ sequencing effects. Fig. 6.22

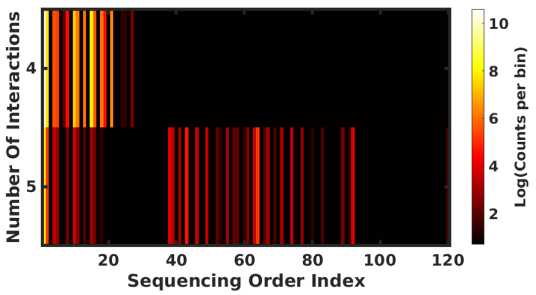

Figure 6.22: Sequence cases distribution for 4 and 5 interaction events using FIL-MSD. Note that the log of the frequency is taken to allow for better contrast between the different indices. This plot is meant to display the complexity of modeling the PSF for more than 3 interaction events.

plots the distribution of sequencing cases for 4 and 5 interaction events and the large number of different sequences[6].

6.1.7 Summary and Spherical Harmonic Transform of the 3-Interaction PSF Model

In Sec. 6.1, we aim to develop an analytical PSF for filtering 3-interaction images and take into account the different cases of sequencing. The model consists of the true sequenced case and two other cases, which were created via the inspection of the interaction mechanism. Events that scatter with $\theta_A \in (0, \omega^*)$ result in missequencing cases 1, 3, 4, and 5. As evident from Fig. 6.2, cases 4 and 5 are not likely. Case 1 orders events A and B incorrectly and results in the PSF $h_{\text{case }1}(\cos\omega)$ to have the form shown in (6.17). Case 3 is omitted in this study as no correlation with interaction A could be identified. Events with $\theta_A \in (\omega^*, \pi)$ result in cases 0 and 2. Case 0 can easily be modeled as an extension of Parra's model [60] by limiting the bounds of integration resulting in (6.8), or $(h_{case\ 0}(\cos\omega))$. Case 2 is modeled by convolving it with the kinematic behavior, resulting in (6.18). The different components are then Gaussian blurred further with a 30° to result in a more realistic PSF shown in (6.20).

$$h_{3\ interaction}(\cos\omega) = g * \left[c_0 h_{case\ 0} + c_1 h_{case\ 1} + c_2 h_{case\ 2}\right], \tag{6.20}$$

[6] $4! = 24,\ 5! = 120$

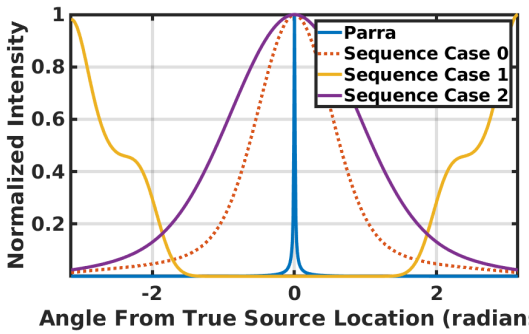

Figure 6.23: Each of the sequencing cases are blurred with 30° Gaussian function and are compared to the Parra's derivation.

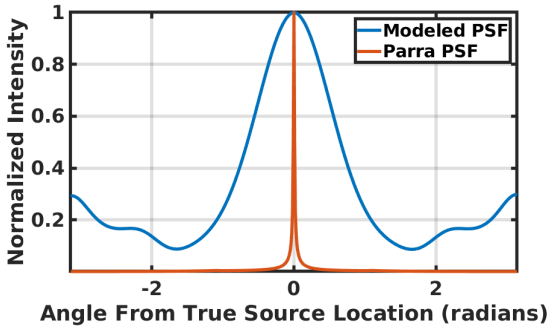

Figure 6.24: Final form of the analytical PSF for 3-interaction events compared to Parra's derivation.

where g, represents the Gaussian blur function and the coefficients c_i are meant to weigh each case with the probability of them occurring. Each of the components are blurred in Fig. 6.23 and their summation is available in Fig. 6.24. Next, using (5.10), we can convert the PSF into spherical harmonics (SH) space and display it in 'frequency' space. The response in high frequency is quite low indicating that a direct inverse filter may produce high frequency noise.

6.2 Application of the Filter

The Spherical Harmonic Transform for numerical simulations (SHTns) [65] library was used to facilitate the spherical harmonic transform of the Compton images. The SH coefficients of the simulated PSF were pre-calculated using MATLAB with (5.10).

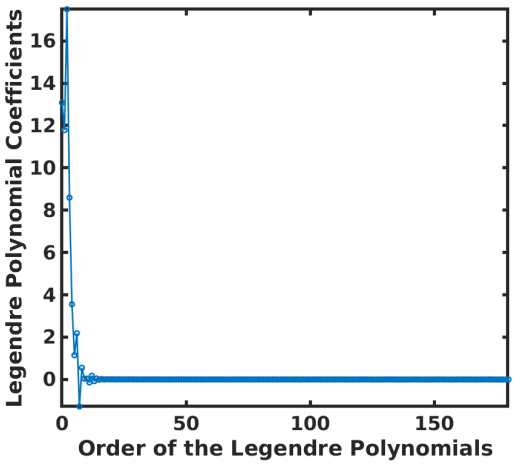

Figure 6.25: Spherical harmonic transform of the modeled PSF plotted in Fig. 6.24.

Following the SH transform of the Compton image, a convolution with the filter is applied as described in (5.4).

The resulting filtered images were compared to Chu's method [14, 17], which is similar to Parra's derivation [60], but with the physics components removed and accounted for in a different stage of the reconstruction. Several image quality metrics were used in this study, including FWHM, mean-squared error (MSE), and structural similarity (SSIM) [69]. To calculate the MSE and SSIM, a synthetic reference image was developed that makes use of delta point sources at the locations where the gamma-ray sources should be. The reconstructed images were normalized by the area underneath the hotspot. FWHM was calculated via a double Gaussian fit for the two source system.

When implementing the filter, some knowledge of the spectral composition of the noise and signal is required. Chu has done some work on creating an adaptive parameter to maximize the backprojected SNR with parameter $R(l)$ and developing a best fit model. This was not implemented in this study as the fit is sensitive to energy and location of the source relative to the detector. In addition, it does not account for multiple or extended sources. As discussed in Sec. 5.1, the $R(l)$ will affect on the reconstructed image. Fig. 6.26 plots different parameters using a simulated

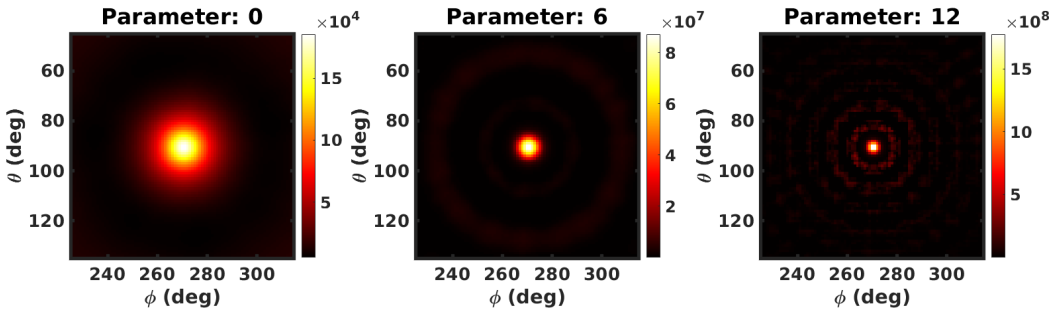

Figure 6.26: Different regularizer parameters $R(l)$ used to filter the Compton image. a) Represents what would be an under estimated SNR. b) Is a representative of an appropriately chosen SNR while c) over estimates the parameter resulting in noise and artifacts.

dataset. The different images demonstrate the importance of choosing an appropriate regularizer parameter. Rather than empirically deciding $R(l)$, the parameter values were looped through, and the MSE calculated for each reconstructed image. The reconstruction with the minimum MSE was chosen as the output.

6.3 Results From Simulated Data

This section applies the filter for 3-pixel events from a simulated 2.6 MeV gamma-ray source. The simulation accounted for the pixelation of the detector, but did not include subpixel information. As usual, side neighbouring events were omitted.

This study modeled 2 sources placed a meter away and 35.3 cm (20°) apart relative to a 3×3 detector. Using 600k events, an SBP image was constructed and available in Fig. 6.27. Next, filtering using the Newtonian and modeled PSF took place with different regularization parameters. The MSE and SSIM was then calculated with a reference image modeled with a Dirac delta located at $(\phi, \theta) = (270°, 80°)\&(270°, 100°)$. The results of the two metrics is presented in Fig. 6.28.

Next, the images between the two PSF models were compared using the R parameter that minimizes the MSE for the respective reconstructions. To quantify the image resolution, a double Gaussian fit was applied to the cross sectional mid-line along the

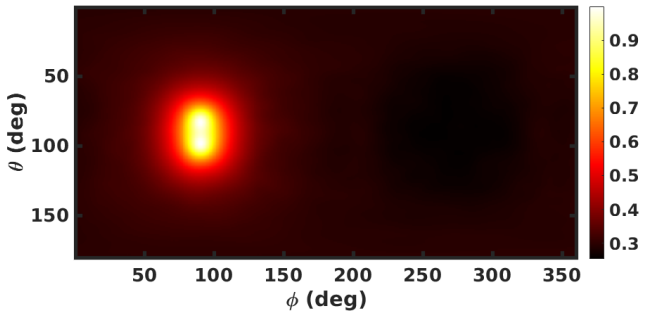

Figure 6.27: Simple backprojection of a two simulated 2.6 MeV source, (20°) apart. The colorscale represents a normalized intensity with respect to the peak value.

two sources. The reported FWHM is the average of the two fitted Gaussians and the trend vs. R is plotted in Fig. 6.29.

Table 6.3: FBP results from a two source simulation

PSF	R - Parameter	FWHM (deg)	MSE ($\times 10^{-4}$)	SSIM
Newtonian	10.6	7.20	0.3048	0.9980
Modeled	7.0	6.95	0.3053	0.9979

Finally, the images between the two PSF models were compared using the R parameter that minimized the MSE for the respective reconstructions. The 'best' images are presented in Fig. 6.30 and a cropped image in Fig. 6.31. From a qualitative perspective, the peak to valley ratio is superior for the modeled PSF when compared to the Newtonian PSF. This is better seen in the cross sectional view along the mid-line presented in Fig. 6.32.

The results of the reconstruction is available in Table 6.3 showing an improvement in the FWHM from 7.2° to 6.95°, however, at a cost of a poorer SSIM. The lower SSIM value could be attributed to the 'ringing' structures arising concentrically around the true source location. The ringing is exaggerated when an inappropriately large R parameter is chosen, as seen in Fig. 6.26c. These artifacts are reminiscent of 'zonal' latitudinal spherical harmonics, which are SH with $m = 0$ [61]. Further discussion on the artifact is available in the conclusion of this chapter (Sec. 6.5).

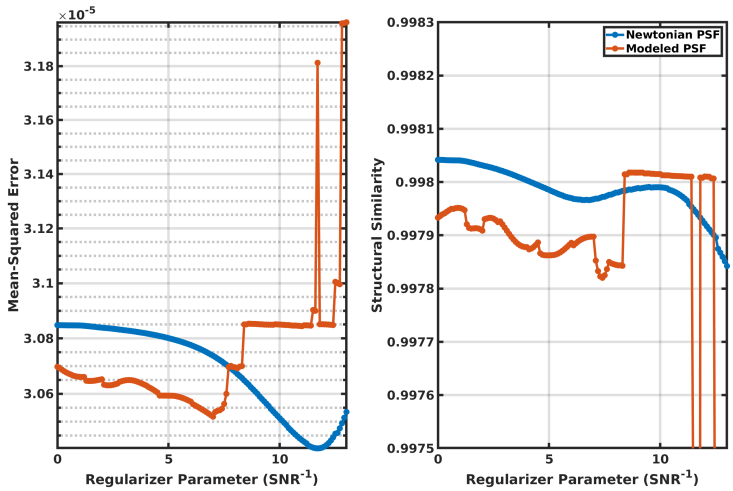

Figure 6.28: Plot different image quality metrics for a two-source simulation with different R parameters for a) mean square error and b) structural similarity. For the modeled curve, values over 7.1 are not reliable as the image are plagued with high frequency noise.

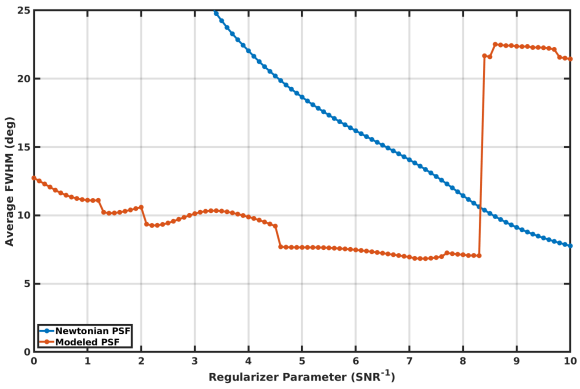

Figure 6.29: Average FWHM vs. R of the simulated two sources for the two different PSF models. For the modeled curve, values over 7.1 are not reliable as the image are plagued with high frequency noise.

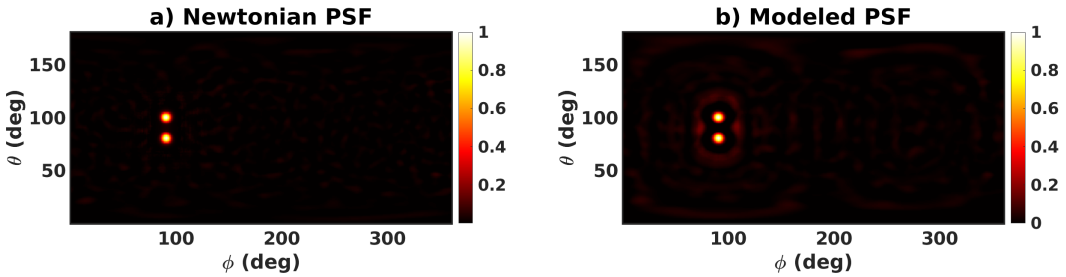

Figure 6.30: Filtered images using the respective regularizer that minimized the MSE for a PSF model that is a) Newtonian or b) modeled. Note the two rings formed concentrically around each hotspot.

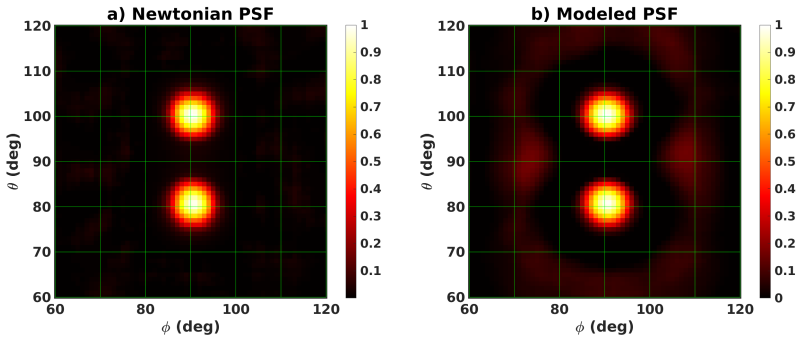

Figure 6.31: Cropped images of Fig. 6.30 using a) Newtonian or b) modeled PSF. The grid spaced with 10° intervals.

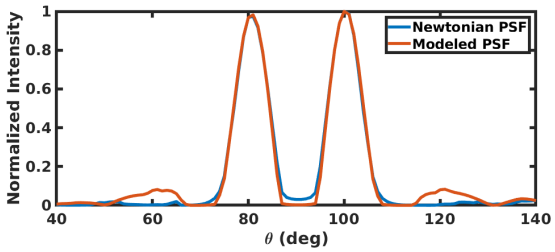

Figure 6.32: Cross section of the Fig. 6.30 PSF model result using Newtonian or modeled PSF.

6.4 Experimental Results from Applying the Modeled Filter

This section presents experimental results when using the OrionUM system and a 20 μCi ^{228}Th source, emitting a 2.6 MeV gamma ray. No subpixel estimation was included, however, 'trigger+8' was enabled to allow for weighting potential cross talk compensation to take place. Once again, only 3-pixel events were used with a deposited energy of 2.55-2.69 MeV. In addition, under the guidance set in Chap. III, side-neighbouring as well as events with opening angle $\Phi = 42° - 50°$ were cut from the image as they might present pair-production events.

As two sources of equal intensity were not available, the same source was placed 85 cm away from the iso-center and offset 22.8 cm from it at two different times. This implies that there is a 30° separation between them. Each location culminated in a 6 day measurement, and the two data sets were concatenated to emulate a two source system. A setup of the experiment is available in Fig. 6.33.

The SBP image, consisting of 40k counts, is shown in Fig. 6.34. The image metrics for different R parameters is available in Fig. 6.35 while the summary of the FBP images using the MSE minimization criteria is organized in Table 6.4. Fig. 6.36 plots the change of the average FWHM and shows an decrease in the average FWHM from 9.53° to 8.67°. The MSE minimized images is available in Fig. 6.37.

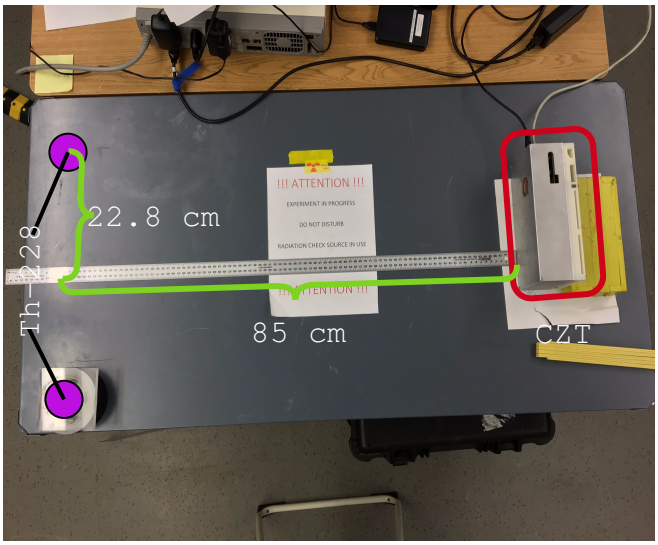

Figure 6.33: Setup of the two source experiment, where each source was placed 15° away from the detector's isocenter.

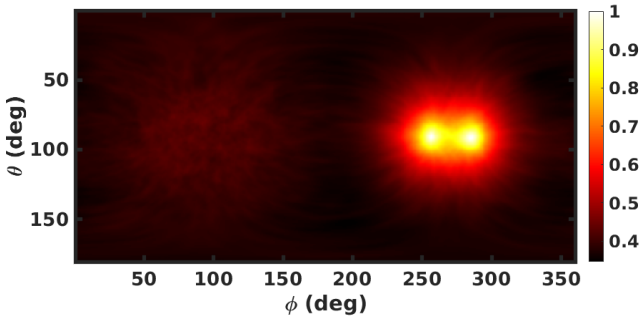

Figure 6.34: Simple backprojection of a two ^{228}Th source 30° apart. The colorscale represents a normalized intensity with respect to the peak value.

Table 6.4: FBP results from the two source experiment

PSF	R - Parameter	FWHM (deg)	MSE ($\times 10^{-4}$)	SSIM
Newtonian	8.3	9.53	0.3078	0.9978
Modeled	2.4	8.67	0.3078	0.9972

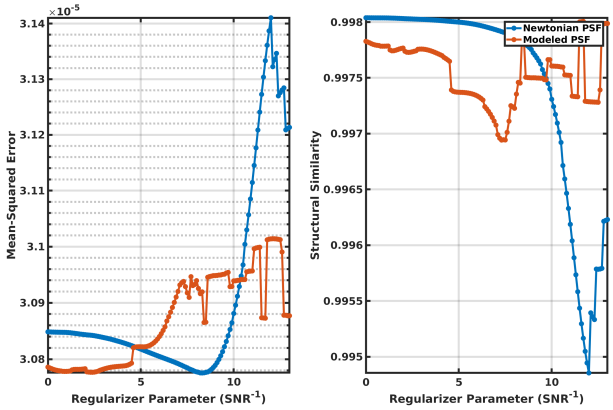

Figure 6.35: Different image quality metrics for a two-source experiment with different R parameters for a) mean square error and b) structural similarity.

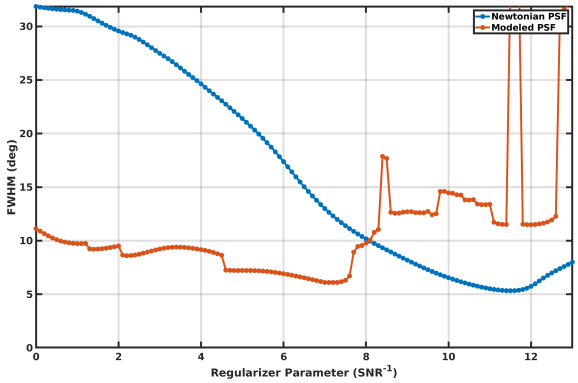

Figure 6.36: FWHM vs. R of the single source experiment for the two different PSF models. FWHM was calculated via a double Gaussian fit. Data above $R = 7.5$ for the modeled PSF is omitted as it yielded a noise image which made FWHM calculations unreliable.

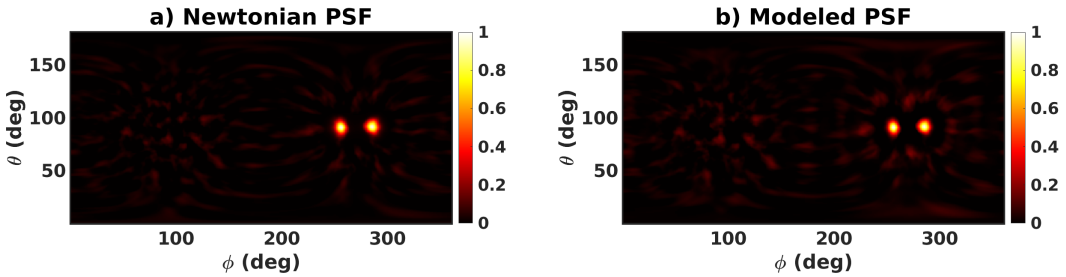

Figure 6.37: Filtered images of a two source experiment using the respective regularizer that minimized the MSE for a PSF model that is a) Newtonian or b) modeled. Note the two ring formed concentrically around each hotspot.

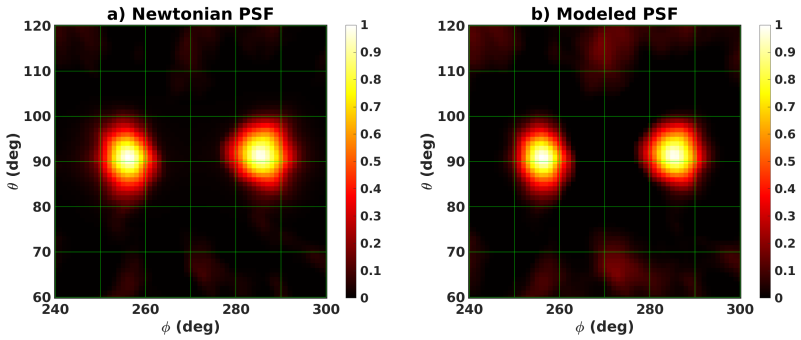

Figure 6.38: Cropped images of Fig. 6.37 using a) Newtonian or b) modeled PSF. The grid spaced with 10° intervals.

6.5 Conclusion on Filtering

This chapter developed an analytical point spread function model for high-energy 3 interaction events that includes detector effects such as missequencing and Gaussian broadening. During the development of the PSF, the filtering was revised to rigorously formulate the use of the Wiener filter for spherical harmonics, which can be applied to any number of interaction.

The image resolution has shown an improvement in the average FWHM from 7.2° to 6.95° for a simulated two sources and from 9.53° to 8.67° when using experimental data.

This all came at a cost of increase artifact in the form of rings that are concentric with the hotspot. The cause of this is unknown during the time this manuscript was composed. Several debugging steps were taken to attempt mitigation. This included increasing the number of image pixels, number of spherical harmonic basis, and augmenting the Gaussian blur of the modeled PSF, where as of yet unsuccessful. However, alleviation of the artifact was seen when the Gaussian broadening of the Compton rings themselves was fixed.

This segues to a discussion to the deficits of this work. When the PSF model is created, there is an opportunity to add an additional term to model the energy and position uncertainty of the imaging system, as done by Hirasawa [68]. This addition will result in a more accurate PSF model.

All the references to the Wiener filter uses $R(l)$ to signify the inverse of the signal to noise ratio. It also implies that it is a function of l. However, this work assumes a uniform noise in frequency, which is probably not true.

Finally, which is perhaps the most alarming deficit, is the assumption of stationary noise and signal. First, the PSF is not shift-invariant. Due to the geometry effects, it can be shown that the PSF will augment based on the source position. This also means that the noise is shift-variant as well as correlated with the signal and presents

a challenge in MLEM as it is not accounted for in the system response.

CHAPTER VII

Demonstration of 3D Gamma-Ray Imaging Using Pixelated CdZnTe and a Personal Odometry Unit

The ability to image in three dimensions allows for localisation and characterization of radioactive material in a 3D space. Compared to imaging on a 2D spherical or rectangular surface from a stationary location, 3D imaging can reveal attributes that are not apparent in 2D imaging such as 3D source extension, source activity, and its 3D location. To demonstrate this capability, sensor data fusion between a pixelated CdZnTe gamma-ray detector and an inertial measurements unit (IMU) based personal odometry system (attached to the footwear of the operator) is used to reconstruct 3D gamma-ray images. A simple comparison between 3D Compton imaging and inverse-square image-reconstruction algorithms is presented and demonstrates the advantage of 3D gamma-ray Compton imaging over traditional localization techniques.

7.1 Introduction

Gamma-ray source localisation is used in a multitude of fields such as emergency response, medicine, and astronomy. One application is search and identification missions, where reconnaissance in areas populated with radioactive material is required to be characterized [70]. This is done in a two step process: detection and localisation.

Detection can be accomplished by a radiation sensor such as a Geiger counter or spectrometers. Localisation can be achieved by several techniques and their effectiveness depends on the scenario complexity. Those include search pattern techniques that implement simple scalar counting methods as well as the use of stationary or mobile imaging systems.

Gamma-ray Compton imaging is one technique used to localise a radioactive source. With a stationary imager, the system can estimate the source distribution by backprojecting a Compton cone onto some image space estimating the direction of the incoming gamma rays [71]. Given enough parallax, 3D localisation could be accomplished via Compton imaging as shown in CdZnTe by Xu [26], who was able to reconstruct a near-field source in 3D space. The extent of the detector was sufficient to estimate the 3D location of the gamma-ray source in the near field but would fail at larger standoff distances.

In far field applications, where the extent of the detector is relatively small when compared to the source-to-detector distance, more advanced methods are required to estimate the 3D distribution. One such method uses the spectroscopic information from the detector to estimate the characteristics of signal attenuating material between the source and detector. In an algorithm developed by Streicher [72] and implemented by Goodman in Compton imaging [73], CdZnTe was shown to estimate the source distance using only spectroscopic and single-view imaging information in ranges over 200 meters. Another advanced method exploits the parallax information inherent to mobile imaging systems. Several systems have been proposed and implemented that use LiDAR or fixed beacons [74, 75]. Aerial measurements have demonstrated the ability to image the distribution of gamma-ray sources [21, 76–78]. Finally, robot mounted detectors have also shown great localisation ability [23, 79].

The proposed method seeks to simplify the 3D imaging process by reducing computation expense and streamlining the workflow by use of a pixelated CdZnTe

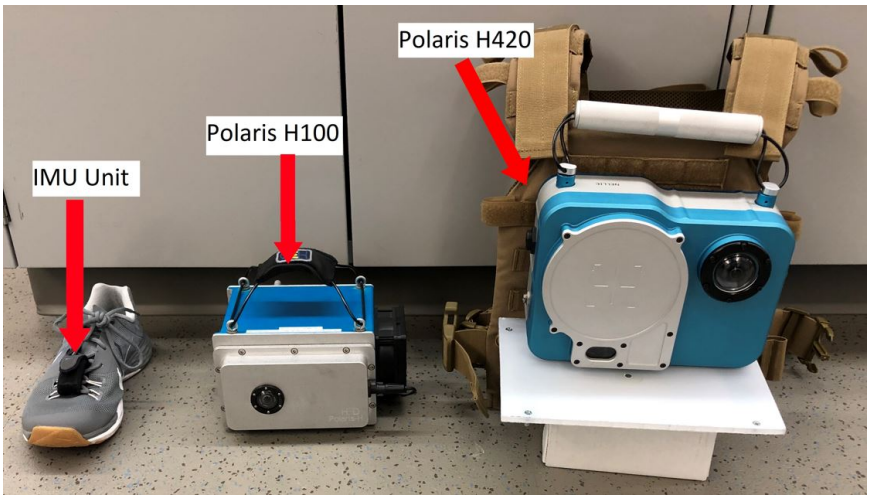

Figure 7.1: Image of the Polaris H100 and H420 CdZnTe detector, and the IMU placed in the footwear of the user.

gamma-ray imaging system and an IMU. The goal of this study is to present the method as a proof of principle and to compare the effectiveness of an imaging system to a spectrometer for source localisation. Section 7.2 summarizes the systems chosen to solve the particular problem and provides rationale behind the choices. Section 7.3 outlines the two imaging modalities explored in this study, while Sections 7.4 and 7.5 present experimental measurements of indoor and outdoor scenarios respectively.

7.2 Gamma-Ray Imager and Positioning Systems Employed

Imaging gamma-ray sources in 3D requires both a gamma-ray detector and a system to estimate the detector's location and orientation. To accomplish this, we use an IMU that is placed on the footwear of the user and a pixelated CdZnTe system for gamma-ray detection and imaging, all pictured in Fig. 7.1.

7.2.1 Pixelated CdZnTe Gamma-Ray Imaging System

A high resolution spectrometer is desired as it can provide an increased level of discrimination between terrestrial or cosmogenic background radiation and the various sources to be localized. The gamma-ray detector system used in this study,

manufactured by H3D Inc., consists of an array of $2 \times 2 \times 1.5\ cm^3$ CdZnTe crystals, each with an array 11×11 pixelated anodes with 1.72 mm pitch, and a single planar cathode [80]. This configuration allows for measurement of the 3D position of each gamma ray interaction within the detector and the corresponding energy deposited with a resolution of less than 1% full-width-at-half-max at 662 keV. If the interaction locations are not utilized, the system simply behaves as a standard gamma-ray spectrometer. Two detector models were used in the campaigns described here: a single-crystal Polaris H100 for the indoor measurement discussed in Sec. 7.4, and the four-crystal Polaris H420 for the outdoor measurement discussed in Sec. 7.5.

7.2.2 Personal Odometry Unit

Position was determined using a Navigation Solutions LLC model RT-BLE-001, a foot tracker chosen due to its ability to record both location and orientation in GPS denied areas and does not require any imaging based methods [81]. Simultaneous localisation and mapping (SLAM) based systems were disqualified to allow for potential system in restricted areas. SLAM also requires marking features in a scene. Therefore, measurements would suffer in large and open spaces where the features are beyond the range of the sensor, such as a desert.

IMU units are well known to suffer from non-stationary drift that leads to error growth over time. Several solutions have been proposed to account for the drift, but each with corresponding strength and weaknesses. The algorithm used in the implemented IMU assumes the foot will be at rest for some small time when it is in contact with the ground. Any readings at that time can be used to calibrate the IMU resulting in a more accurate measurement [82].

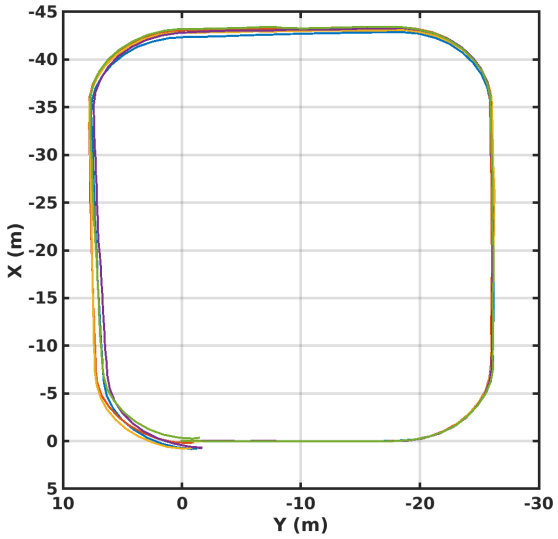

Figure 7.2: Plot of 5 different laps taken with the RT-BLE-001 IMU.

7.2.2.1 Personal odometry unit error quantification

The RT-BLE-001 IMU was tested to determine the error in position due to drift by walking on an indoor track. Each lap started and ended at the same point, any discrepancy is therefore due to error resulting from the unit. Fig. 7.2 plots the 5 different laps taken.

The average distance between the start and stop location was measured to be 1.36 m with a standard deviation of 0.26 m. The total measured distance by the IMU was 141.7 m. It is worth noting that the error in final position is highly path dependant.

7.2.3 Implementation of Systems

The system is configured to reconstruct 3D images in real-time. In the implementation, both the IMU and the detector system communicate to a computer via a TCP/IP connection, with the detector acting as the router. After every data-packet received by the computer, the imaging software constructs the system matrix, holds it in memory, and processes it through a maximum likelihood expectation maximization (MLEM) algorithm. Therefore, the IMU and gamma data are synchronized by the

Figure 7.3: Still image of the field experiment conducted at the Idaho National Laboratory. The detector can be seen mounted on the user via the use of a vest and the IMU placed in the foot ware.

time of reception. The algorithm is described in detail below in Sec. 7.3.

As a wearable device, the detector is mounted to a load bearing vest (a plate carrier in this case). Fig. 7.3 depicts the implementation of the mounted system on the operator. In this study, the detector's coordinate system is assumed to be that of the IMU. Although the IMU can provide the pose information (orientation in space), it was found that using the velocity vectors (calculated by taking subsequent positions) results in a more accurate direction estimation. The IMU pose reconstruction suffers from the variable gait of the user. The future work section discusses methods to correct for the discrepancy between the foot mounted IMU and imager.

7.3 Overview of Imaging Methods

Several methods exist to form a 3D image of gamma-ray sources, however, only two are utilized in this study. The first is the 'inverse-square localisation' which can be achieved with any simple gamma-ray counter or spectrometer. The second technique utilizes gamma-ray Compton imaging, which requires position sensing, supplied by an advanced detector such as pixelated CdZnTe. Both techniques are well established, but are summarized here for completeness and clarity.

Pixelated detectors can also produce images using the geometric self-attenuation of

the detector, or 'Centroid Method' [83]. Although effective at low energies, Compton scattering is dominant at higher energies and an attenuation profile in 3-D CdZnTe detectors is less observable as the gamma rays are more penetrating and will lead to poor image results. Coded aperture methods were not considered for a similar reason as they are mostly effective for energies lower than 250 keV. However, both techniques in principle can be used for 'low-energy' gamma-ray source localisation.

7.3.1 Inverse-Square Localisation

Detected count rates from a source are approximately proportional to the inverse of distance from the source squared ($1/r_d^2$), where r_d is the distance between the detector and the source. Therefore, the expected counts ($\hat{C}_{\mathbf{r}_d}$), in time ∂t, for a detector with intrinsic efficiency (ϵ_d) at position $\mathbf{r}_d$ from a source at position $\mathbf{r}_S$ with intensity A_0 is:

$$\hat{C}_{\mathbf{r}_d} \approx \frac{\epsilon_d A_0 \partial t}{\|\mathbf{r}_S - \mathbf{r}_d\|^2}, \tag{7.1}$$

where $\|\dots\|$ calculates the magnitude of the vector. This implies that source localisation can be achieved by constructing the following intensity map:

$$f(\mathbf{r}_j) = \frac{1}{S_j} \sum_{i=1}^{N} \frac{C_{\mathbf{r}_i}}{\|\mathbf{r}_{i,d} - \mathbf{r}_j\|^2}, \tag{7.2}$$

where j denotes the image pixel index, $\mathbf{r}_{i,d}$ is the location of the detector for event i, with total time bins N, and $\mathbf{r}_j$ is the location of image pixel j. The S_j term is the sensitivity term dependent on the path and time bin size (∂T) of the detector, which was fixed at 10 μS in this study as it is small enough to eliminate position error due to binning the user movement. It is constructed as follows:

$$S_j = \sum_{i=1}^{N} \frac{\partial T}{\|\mathbf{r}_{i,d} - \mathbf{r}_j\|^2}, \tag{7.3}$$

7.3.2 3D Compton Imaging Localisation

Compton imaging is made possible by the 3D position sensitivity of the CdZnTe detector with pixelated anodes. If at least two interactions occur, a Compton ring with opening angle Θ_i, calculated via the Compton scattering formula, can be backprojected

onto the image space as follows:

$$t_{ij} = \frac{1}{\|\mathbf{r}_{i,d} - \mathbf{r}_j\|^2} e^{-\frac{(\Theta_i - \theta_j)^2}{2\sigma_i^2}} \prod_{k=1}^{N_{\text{interactions}}} \frac{\mathrm{d}\sigma(\Theta_i)}{\mathrm{d}\Omega} e^{-\mu(\mathbf{r}_{k+1}^{pos} - \mathbf{r}_k^{pos})}, \tag{7.4}$$

where t_{ij} is the system matrix, θ_j is the angle between the image pixel and lever arm, and σ_i represents the standard deviation of the ring blurring term derived from error estimations of the system [26, 27].The Klein-Nishina cross section is represented by $\frac{\mathrm{d}\sigma(\Theta_i)}{\mathrm{d}\Omega}$ [52]. The exponential terms add the attenuation probabilities calculated from interaction location $\mathbf{r}_k^{pos}$.

When constructing the t_{ij}, voxels within 20 cm of the detector ($\mathbf{r}_{i,d} < 20$ cm) were nullified to protect from the divergent behavior of the inverse-square in the system matrix. A simple backprojection image can be constructed by summing all the recorded interactions, $I_{SBP}(\mathbf{r}_j) = \frac{1}{S_j} \sum_{i=1}^{N} t_{ij}$. Using a more advanced algorithm, such as MLEM presented in (7.5), the maximum likelihood estimate of the source distribution can be calculated.

$$f_j^{k+1} = \frac{f_j^k}{S_j} \sum_{i=1}^{I} \frac{t_{ij}}{\sum_{j'=1}^{J} t_{ij'} f_{j'}^k}, \tag{7.5}$$

where f_j^k is the estimate of the source intensity for the k^{th} iteration. A mathematical based stopping criteria has not been developed for this study. Therefore, unless stated otherwise, 5 iterations were chosen as it has shown to not over-iterate in most experimentation.

7.4 Experiment in an Indoor Environment

Experiments in this section aim to show the effectiveness of using an imaging system for 3D imaging against a simple spectrometer. They are presented in order of increasing complexity and are meant to reflect real world scenarios. The conducted experiments used a 150 μCi ^{137}Cs point source placed in various locations with different shielding configurations.

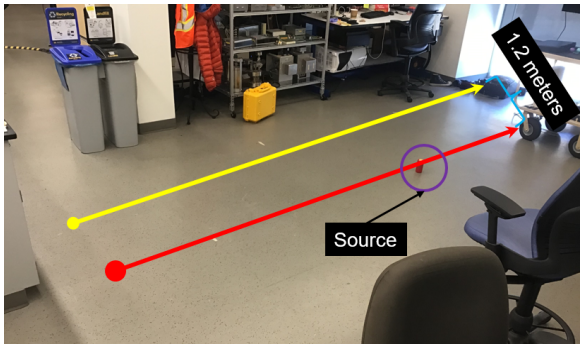

Figure 7.4: The experimental setup of a single source measurement where a straight trajectory was taken. The red and yellow lines illustrate the approximate path for sections 7.4.1 and 7.4.2 respectively. The yellow trajectory is 1.2 meters away from the source at its closest point.

7.4.1 Straight path over the source

A straight path was taken such that the trajectory passed directly over the source. Fig. 7.4 illustrates the approximate path in red relative to the source location. Naturally, it would be very simple for a counter or spectrometer to localize the source by monitoring count rates for a maximum that identifies the source position. This assumes that there is a simple single point source with no advanced shielding. The resultant image of this experiment using inverse-square reconstruction and 3D Compton imaging is available in Fig. 7.5a and b respectively. Both methods have localized the source very close to the true source location.

7.4.2 Parallel trajectory 1.2 meters away from source

To complicate the previous experiment, a straight trajectory was taken again, 1.2 meters parallel to the source. The path is illustrated in Fig. 7.4 with a yellow vector. Unlike the previous experiment, the inverse-square localization will not be able to localize the source, but will be able to find the perpendicular location as shown in Fig. 7.6a. Since imaging is not applied in the inverse-square localization, the detector cannot reconstruct the location perpendicular to the path. However, with Compton imaging applied, the general source location has been localized. The

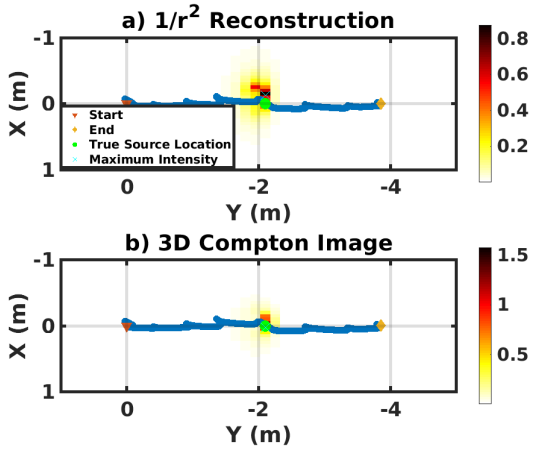

Figure 7.5: Reconstructed bird's eye view using a) inverse-square reconstruction b) 3D Compton imaging. The blue scatter plot represents the reconstructed position as measured by the IMU. The color scale of the graph presents the intensity of each pixel in the gamma-ray image.

maximum intensity spot of the distribution was found to be 1.2 meters away from the traveled path, however, 30 *cm* off along the path. The largest contribution to this error is due to the incorrect location estimation by the IMU and the error between the detector location and that measured by the IMU.

7.4.3 Complex shielding

A challenge to any localization effort is the placement of the source in a complex form of shielding. With the setup shown in Fig. 7.7, more specifically its inset, the source was collimated to allow only two emission streams from the source. An 'L-shaped' search pattern was in which two spikes in count rate were identified while passing alignment with the emission streams. Therefore, the inverse-square reconstruction estimates two sources as shown in Fig. 7.8a. With the use of imaging information shown in Fig. 7.8b, the reconstructed source distribution is more informative and indicative of the true source distribution.

This experiment demonstrates the main advantage of using an imaging system in a source localisation application. It is clear that the simple counter would fail without

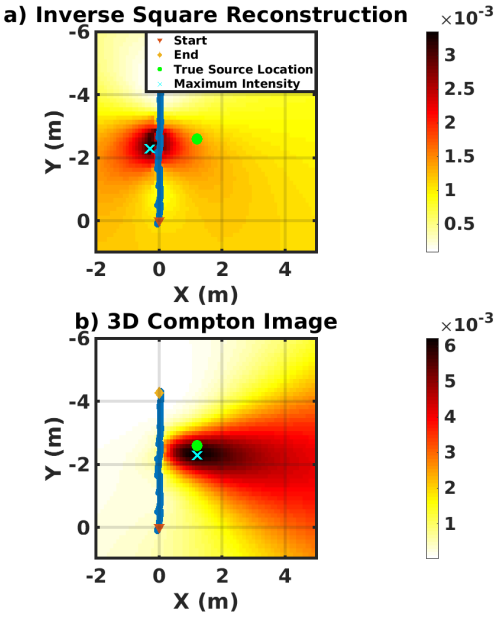

Figure 7.6: Reconstructed source distribution using a) inverse-square reconstruction and b) 3D Compton imaging from an experiment in which a straight line was walked 1.2 meters parallel to the source.

the addition of a priori knowledge of the source distribution.

7.5 Experiment in an Outdoor Field Environment

Field measurements were conducted at the Idaho National Laboratory's (INL) Critical Infrastructure Test Range Complex (CITRC). The specific structure, a former reactor building, is located at GPS coordinates [43°33′17.798″N, 112°52′1.473″W]. The building is structurally composed of cinder blocks and cement with a few windows and doors.

This experiment used a Polaris-H420 gamma-ray imager manufactured by H3D Inc. as shown in Fig. 7.1. Although the system was able to perform coded aperture imaging, this function was not used in the reconstruction as it would not have provided 4π imaging capabilities, and would be limited to events less than 250 keV.

A ^{192}Ir 0.153 Ci source was placed in one of the east-side window of the facility, shown in the magenta hexagram star symbol and a 0.013 Ci source on the west side

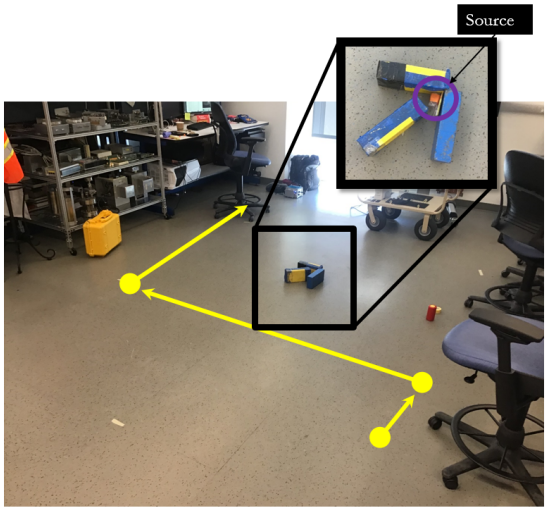

Figure 7.7: Experimental setup for the shielded source scenario with the yellow vectors presenting the approximate path.

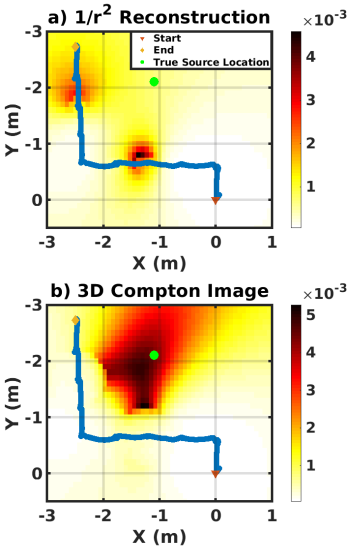

Figure 7.8: The estimated source distribution using a) inverse square and b) Compton imaging.

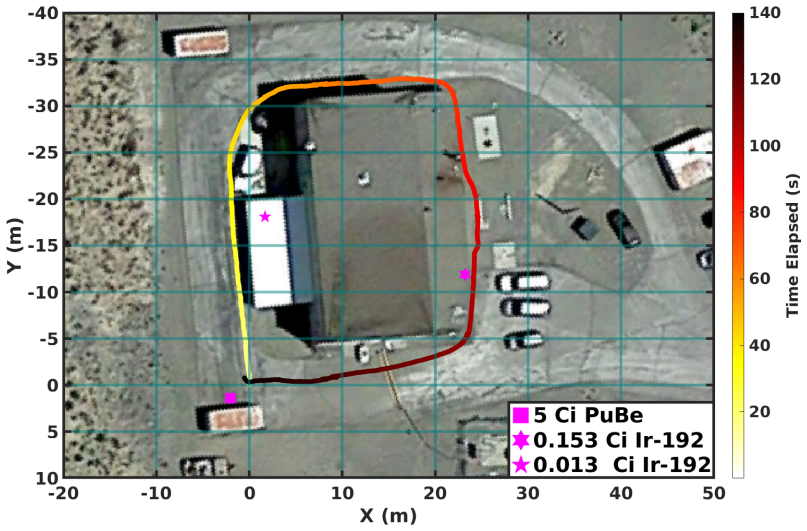

Figure 7.9: The trajectory reconstructed by the IMU overlaid satellite data provided by Google Maps. The position of the ^{192}Ir sources (magenta pentagram and hexagram) and the PuBe (magenta square) source are an estimated location as accurate source location could not be accomplished at the time of the measurement.

window, shown in the pentagram star, both plotted in Fig. 7.9. Minimal counts originated from the source were detected with the source positioned near the center of the building due to the shielding effects of the structure's concrete composition. The figure also presents the measured trajectory superimposed with a satellite image and layered with a color scale corresponding to the time elapse in the measurement. Nevertheless, Fig. 7.10a and b presents the reconstructed images using inverse-square and Compton imaging methods respectively. The inverse-square technique does show a concentration of count intensity near the 0.153 Ci ^{192}Ir source, however with poorer acutance than the Compton reconstruction. The weaker 0.013 Ci can easily be identified in the image while the inverse square shows a minor increase in counts in that area.

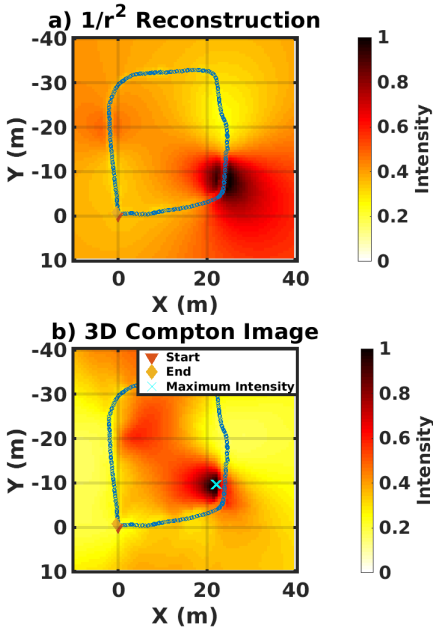

Figure 7.10: The estimated source distribution of the field measurement using a) inverse square and b) Compton imaging. This image presents the simple backprojection rather than an MLEM reconstruction as there were minimal counts recorded.

7.6 Conclusion of 3D Imaging and Future Work

Presented is a 3D gamma-ray imaging technique which uses a foot-mounted IMU and a pixelated CdZnTe imaging system. As discussed in the previous sections, the use of an imaging system results in a more efficient source localisation with higher fidelity as compared to a spectrometer system. The proposed technique hopes to simplify the process giving greater flexibility and increased ability to the operator in a multitude of scenarios and environments.

Some source search and characterization techniques require complex and laborious effort [70]. The addition of a imaging component to traditional spectroscopic concept of operations can potentially reduce exposure and effective dose to surveyors. This technique can be expanded to include a 4π coded aperture mask. With the added mask, higher resolution images could be created in addition to the ability to image low-energy gamma-ray sources. The system could be made more versatile if a second

IMU unit would be placed on the gamma detector itself. The purpose of this would be to measure the actual pose of the detector and not rely on velocity information. This is configured such that a user's torso would have the ability to twist freely, independent of pedestrian motion. Finally, further algorithm development could be envisioned to provide a user with on-the-fly corrections to a prescribed trajectory, further optimizing localization efforts.

CHAPTER VIII

Advancements in Time Encoded Imaging

Time encoded imaging is a technique to image gamma rays by using a time-varying coded aperture to modulate the gamma-ray signal spatially and temporally. The quality of the image is related to the size of the aperture and the reconstruction fidelity of the coded projection, among other factors. The major blurring in the projection recording occrs from the poor position reconstruction of the interaction location within the detector. Using the OrionUM pixelated CdZnTe digital-ASIC readout detector system, the 3D subpixel position of each gamma interaction can be estimated to a resolution of 500 μm full-width-at-half-maximum (FWHM) for a 120 keV gamma ray. With the addition of subpixel estimation, the FWHM of the image point spread function has improved by almost a 10% deduction. Next, the 3D distribution of gamma-ray source can be estimated via a depth refocusing technique and demonstrated on extended sources. The experimental measurement uses special nuclear material (SNM) from the Idaho National Laboratory is presented to demonstrate the 3D source distribution estimation capabilities of the system.

8.1 Introduction

Coded aperture imaging presents a technique to image radiation particles and has applications in astronomy [84], medicine [85], and homeland security [86]. It is

accomplished with the use of a coded mask and radiation detector. It also introduces an attractive approach to image low-energy gamma-rays ($< 250\ keV$) with pixelated CdZnTe [87]. As the main mode of gamma-matter interaction in that energy range would be photoelectric, traditional scatter-based techniques would fail. Coded aperture imaging allows for the spatial coding of the radiation source that can then be used to reconstruct an image from the projected shadow.

A mathematical model of the observation matrix can be formulated as follows:

$$\mathbf{O} = \mathbf{F} * \mathbf{A} * \mathbf{D} + \mathbf{B}, \tag{8.1}$$

where $\mathbf{O}$ is the observation matrix, $\mathbf{F}$ is the source distribution, $\mathbf{A}$ is the mask transmission matrix, $\mathbf{D}$ is the detector response term, and $\mathbf{B}$ is the noise term. The mathematical operation $(*)$ represents a convolution operator. Correlation with a decoding function $(\mathbf{G})$ presents one of the more popular reconstruction techniques [31]:

$$\hat{\mathbf{F}} = \mathbf{O} \circledast \mathbf{G}, \tag{8.2}$$

with $\hat{\mathbf{F}}$ representing the estimated source distribution and $\circledast$ symbolizing a periodic cross-correlation operator. $(\mathbf{G})$ is chosen such that $\mathbf{G} * \mathbf{A} = \delta$.

Time-encoded imaging (TEI) is an extension of coded aperture imaging, in that it uses a coded aperture to spatially encode the source, but also contains a temporal encoding as well [32–34]. This manuscript presents advancements in the University of Michigan's Mira time-encoded imaging system. The first improvement is accomplished by leveraging the digital OrionUM system, which can provide the subpixel location of each interaction and lessens the blurring effect of $\mathbf{D}$ in Equation 8.1. Next, improvements in image resolution are accomplished by application of depth of interaction correction that is verified with experimental collimation experiments. These additions are then utilized to estimate the 3D source distribution via a depth-refocusing technique. Finally, the 3D profile of special nuclear material (SNM) objects is presented from experiments conducted at Idaho National Laboratory (INL).

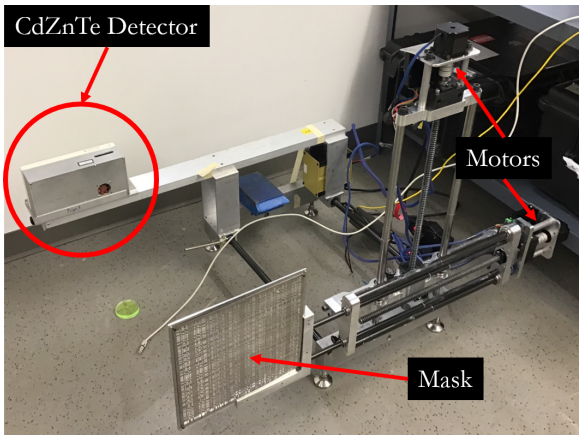

Figure 8.1: The OrionUM CdZnTe detector attached to the Mira system with the tungsten coded mask and the stepper motors labeled.

8.2 Mira, The Time Encoding Imaging System

The TEI system is comprised of a 3D position-sensitive CdZnTe gamma-ray detector as well as the 'Mira' system to translate the coded mask in a manner such that the detector is in the umbra of the coded shadow. Figure 8.1 depicts the imaging-detector system.

The Mira system has two stepper motors to translate the mask horizontally and vertically [33, 34]. The detector is mounted on an assembly that is held by two rails on which it can slide to vary the mask-to-detector distance. The current maximum mask-to-detector distance is 59 cm.

The coded mask is attached at the end of the horizontal arm. The mask itself is made of layerd tungsten sheets, each 0.25 mm thick. The mask is a rank 79 modified uniformly redundant array (MURA) [31] with a total of 200×200 elements for a total size of 12 in $\times$ 12 in. The MURA pattern is therefore repeated 2.53 times. Each element, or pixel pitch, is 1.4 mm wide. In this study, 4 mask sheets were used together totaling 1 mm of thickness as an optimized option for the trade-off between attenuation and collimation effects of thicker masks.

8.3 Implementation and Advancements in the Time-Encoded Imaging System

Resolution is tied to the pixel pitch of the apertures and how well the projection can be recorded, specifically, the resolving of the demarcation between different mask elements. This work makes use of the digital OrionUM system that is capable of superior position resolution when compared to its analog predecessor. Improved position resolution will therefore allow for a higher fidelity reconstruction of the projected mask pattern.

Blurring in the recorded pattern can be modeled as **D** in Equation 8.1. If the detector were able to record the pattern with infinite resolution, **D** can then be modeled as a Dirac delta function. If it were anything else, the point spread function will be modified by the behaviour of **D**. It therefore follows that the magnification of the projection will also have an effect on the image resolution as the recorded pattern will differ. The magnification M can be modeled as follows:

$$M_i = 1 + \frac{B_i}{A}, \tag{8.3}$$

where A and B represent the source-to-mask and detector-to-mask distances. If the projected pattern is magnified such that the pattern pitch is smaller or larger than the pixel pitch of the detector, the reconstructed mask pattern will be blurred which will translate to the final image. Therefore, the addition of subpixel information will increase the fidelity of the recorded pattern reducing the blurring of the image.

The projected mask pattern will also differ with different depths in the CdZnTe crystal as the crystal is extended (1.5 cm in depth to be exact). This is due to the magnification change in different detector depths as magnification depends on the B distance, as seen in Equation 8.3. We therefore apply a depth of interaction (DOI) correction factor, similar to that of Ziock et. al. [88].

Referencing Equation 8.3 once more, the magnification also depends on the A distance, or the source-to-mask distance. Sources at different distances will result in

different magnification. Therefore, the source-to-mask distance can be deduced from investigating the magnification in the system by observing the focusing effects of the system.

8.3.1 Implementation of Subpixel Estimation

Subpixel localisation of the gamma-ray interaction can be accomplished by comparing the transient charges induced in the neighbouring pixels of the triggered pixel anode [89]. This is accomplished by implementing a 'trigger plus 8' mode, where the triggered pixel is read out along with the eight surrounding pixels. Currently, the system has a 300 μm FWHM position resolution for 662 keV events and 500 μm FWHM at 120 keV.

To demonstrate the benefit of implementing subpixel estimation, a 63 μCi ^{57}Co source was imaged with and without subpixel approximation. The experimental setup is available in Figure 8.2. Since two sources of the same activity were not available, two measurements of the same source was taken at two different times. Following the two measurements, the data sets were added together to emulate two sources 1 cm apart. The source was placed near the iso-center of the detector with a source-to-mask distance of $A = 71$ cm. The detector-to-mask distance was set at $B = 30$ cm. For the second measurement, the source was moved 1 cm vertically with a micro-translation stage. Note that the true extent of the check source is unknown as the material is deposited in epoxy.

The final reconstructed images are shown in Figure 8.3. With the application of subpixel estimation, the FWHM has improved by almost 10% as presented in Table 8.1. By first inspection, the peak-to-saddle ratio, or the region between the two peaks, is lower and allows for superior separability of the two sources.

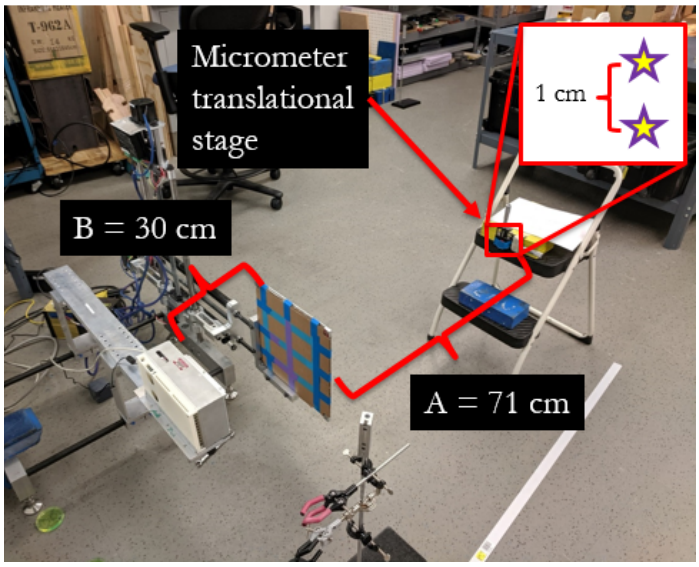

Figure 8.2: Setup of the experiment to demonstrate the improvements in image resolution when applying subpixel estimation. The arrangement of the sources is available in the inset image displaying the two sources positioned vertically 1 *cm* apart.

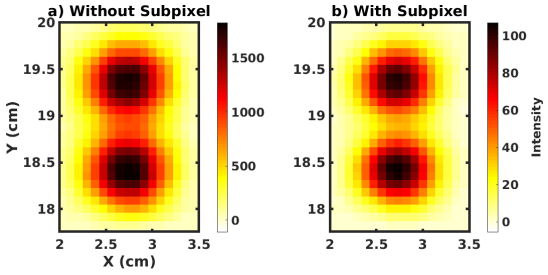

Figure 8.3: Reconstructed images of the two source experiment a) without and b) with subpixel estimation. Via quick observation, the peaks-to-saddle ratio is greatly improved with the use of subpixel estimation.

Table 8.1: Full-width-at-half-maximum values for the two source experiment as calculated via a double Gaussian fit of the lateral cross section. In addition, the percent decrease is also presented. All values are in *cm*

	FWHM Bottom	FWHM Top
Without subpixel	0.66	0.64
With subpixel	0.60	0.58
Percent decrease	9.9%	9.4%

8.3.2 Depth of Interaction Correction

The assumption that all events occur at the cathode side can lead to blurring, especially at the edges of the field of view. Due to the response of the system to magnification, the response will vary with different depths. In addition, the mask projection will be circularly shifted. Therefore, the image frames are zero-padded based on the different magnifications they experience. The cathode, with depth bin $(i = 0)$ and source-to-mask distance of B_0, is closest to the mask. It has the smallest magnification and largest field of view. Therefore, subsequent larger depth bins will result in greater magnification and will require more padding around the frame of the image.

The final image can be computed as the summation of images over different depth bins (i) as follows:

$$\hat{\mathbf{F}} = \sum_{i=0}^{N_d-1} \mathbf{P}_{M_i} * \left[[\mathbf{O}_i \circledast \mathbf{G}] \otimes \mathbf{K}_{M_i} \right], \tag{8.4}$$

where $\hat{\mathbf{F}}$ is the final image estimate, $\mathbf{P}_{M_i}$ is a Dirac delta matrix, or padding impulse function, which is of size $\left[(C \cdot R(1 - \frac{M_0}{M_i})) + 1) \times (C \cdot R(1 - \frac{M_0}{M_i})) + 1) \right]$. C is an arbitrary constant to increase the size of the matrix to avoid rounding effects, and R represents the rank of the mask. The observed pattern for a given depth index i is represented by $\mathbf{O_i}$ while $\mathbf{G}$ is the decoding matrix [31]. Therefore, $[\mathbf{O_i} \circledast \mathbf{G}]$ results in the reconstructed image for depth bin i. That image is then operated on by a matrix of ones $(\mathbf{K}_{M_i})$ to produce a Kronecker tensor product. $\mathbf{K}_{M_i}$ has a size $C \left[\frac{M_0}{M_i} \times \frac{M_0}{M_i} \right]$. Therefore, summing the appropriately zero-padded arrays for all N_d depth bins will result in the depth corrected image.

In the OrionUM CdZnTe system, the depth of interaction (DOI) is calculated via the cathode-to-anode ratio (CAR) for single triggered pixel events [90]. To verify the accuracy of the DOI reconstruction, a collimator experiment was performed where different depths of the crystal were irradiated. The calculated CAR versus the collimator location for three modules is histogrammed in Figure 8.4. The diagonal

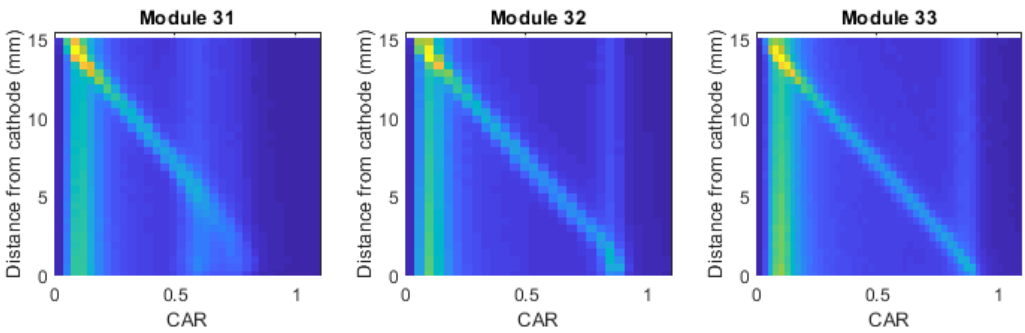

Figure 8.4: Collimator experiment to map cathode-to-anode (CAR) to the depth of interaction for three different modules.

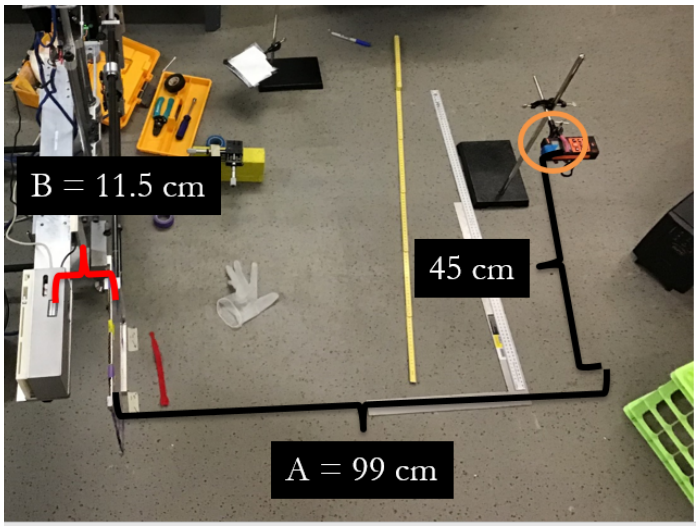

Figure 8.5: Experimental setup with the parameters $A = 99\ cm$ and $B = 11.5\ cm$. The ^{57}Co source, circled in orange, was placed 45 cm off the iso-center of the detector.

band represents the data of interest where the collimated beam interacts with the detector. A linear fit is made on the data of interest and represents the correction factor of the CAR to the depth of interaction. The artifacts in the reconstruction and the fact that CAR does not have an x-intercept of 1 are still under investigation.

To demonstrate the improvement of using the appropriate DOI correction, the following experiment was conducted with the setup shown in Figure 8.5. There, a 63 μCi ^{57}Co was placed $A = 99\ cm$ away from the mask and the detector-to-mask distance was set to $B = 11.5\ cm$. Next, the source was translated 45 cm off the iso-center of the detector.

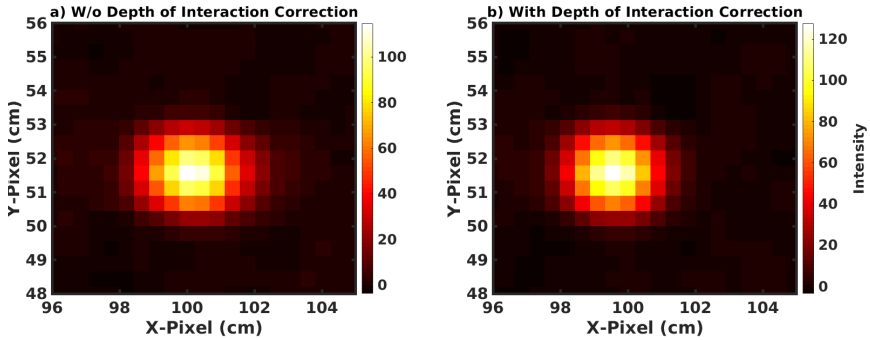

Figure 8.6: Reconstructed images a) without (w/o) the use of DOI correction and b) with DOI correction.

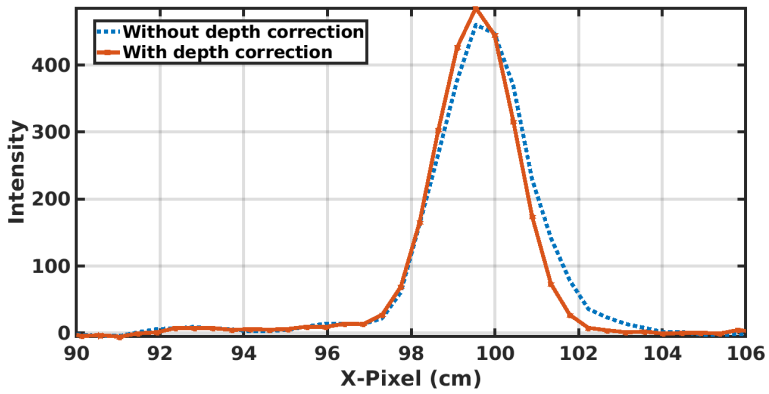

Figure 8.7: Horizontal cross-section of a summation over the verticle y-axis of the source hotspot with and without applying depth correction.

Reconstructing the image without the use of the DOI correction results in Figure 8.6a, where a slight tail is visible that drags to larger X-pixel values. This is suppressed when the correction is applied, shown in Figure 8.6b. This is further visible in the horizontal cross-sectional sums that is shown in Figure 8.7. The FWHM and the full-width-at-tenth-maximum (FWTM) values, along with the percent decrease in those figures when the DOI correction is applied, are presented in Table 8.2.

8.3.3 3D Estimation of Gamma-Ray Sources via Depth Refocusing

Estimation of depth in the image space via the use of coded aperture has been accomplished in optical and gamma-ray cameras [33, 34, 91–93]. Due to the extent of the detector, some parallax exists to estimate depth. When different focal depths

Table 8.2: Full-width-at-half-maximum and full-width-at-tenth-maximum (FWTM) values for the point spread function without and with DOI correction. In addition, the percent change is also calculated. Width values are presented in cm.

	FWHM	FWTM
Without DOI Correction	2.4	4.55
With DOI Correction	2.22	3.99
Percent decrease	7.5%	12.31%

are assumed, where A values are varied to reconstruct different depth planes, the gamma-ray source will focus and de-focus based on the magnification-parallax effects observed by the detector.

This effect is shown in Figure 8.8 where a simulated gamma-ray source is placed in the detector's iso-center, 25 cm away. Figure 8.8a displays cross-sectional slices through the horizon of the image for the different assumed depth. When plotting the intensity of the central pixel, as shown in Figure 8.8b, the intensity is maximized when the focal plane is equal to the true source location (25 cm). Therefore, the most intense spot can be assumed to be the depth location of the source. Section 8.4 presents experimental data with an extended SNM source distributed in 3-dimensions. As the sources may extend away from the iso-center of the detector, DOI corrections are required.

8.4 Imaging of Special Nuclear Material in 3D at the Idaho National Laboratory

This section presents results from an experiment conducted at the Zero Power Physics Reactor (ZPPR) located in Idaho National Laboratory. Measurements of plutonium fuel plates [94] were completed to demonstrate the depth estimation capability and eventual 3D evaluation of the source distribution. Each plate has the dimensions of $7.62 \times 5.08 \times 0.3175$ cm^3. The main elemental composition of the plates include

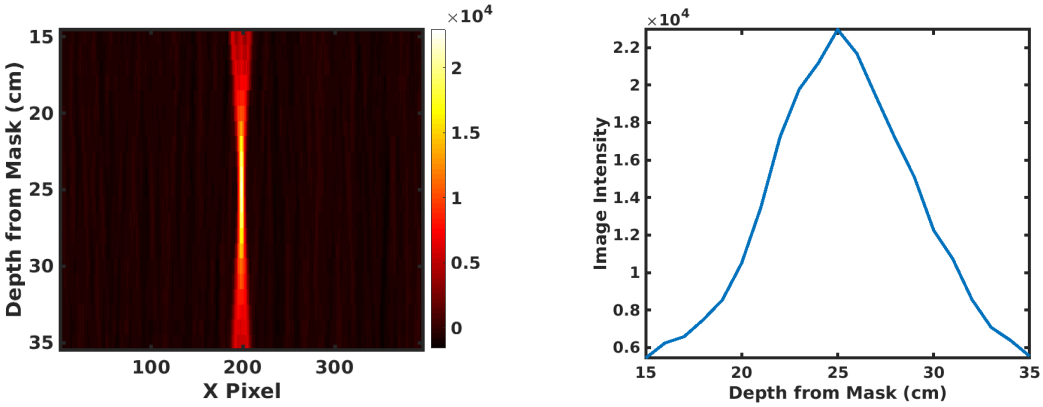

Figure 8.8: Figure presenting depth estimation of a simulated gamma-ray source placed 25 *cm* away from the mask with detector-to-mask distance of 30 *cm*. The image in a) presents a cross-sectional slices along the horizon of the image for different focal depth. b) Intensity of pixels along the iso-center of the image plane with the distribution peaking at 25 *cm*, the true source-to-mask distance.

$\sim$75% ^{239}Pu and $\sim$22% ^{240}Pu, for a total mass of $\sim$111 *g*.

Two plates were sandwiched together with a 2.9 *mm* carbon steel plate in between them. The top and bottom of the Pu plates were covered with aluminum plates. A diagram of the experimental setup is available in Figure 8.9a which shows the plutonium plates angled $\sim$41° away from the detector plane with the closest point of the plate to the mask measuring $\sim$17 *cm*. The 5.08 *cm* face was shielded with a 2 *mm* aluminum plate, as shown in the inset of Figure 8.9b. The measurement values are reported as approximations due to the author's inability to complete the measurements themselves per facility policy.

The reconstructed gamma-ray images are available in the left column of Figure 8.10. In (a) the raw gamma-ray image is presented, while an intensity cut of 125 is applied in (b). Next, using the same method presented in Section 8.3.3, the focal plane is varied. Next, the most intense pixel is located, and its focal plane recorded resulting in Figure 8.10c. Figure 8.10d presents the depth estimate with the mask used in (b). A clear gradient along the plates is clearly visible indicating the source is distributed in 3-dimensions and not in a single depth plane. The measured angles for the top and bottom plates are 24.8° and 30.8° respectively, which is an underestimation of the

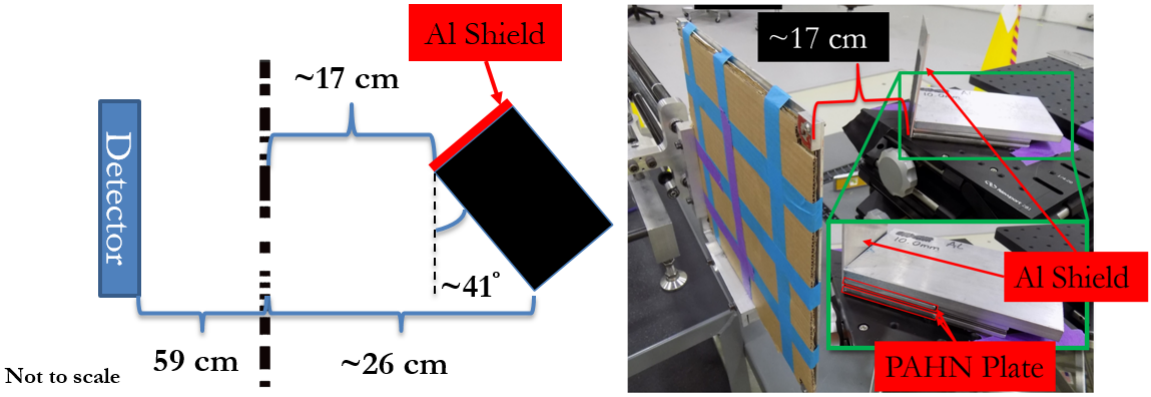

Figure 8.9: a) Diagram of the experimental setup at INL. b) Optical images of the setup with an inset image zooming into the setup of the plates.

$\sim 41^{\circ}$ measured physically during the experiment.

8.5 Conclusion

Via application of subpixel estimation, the pixelated CdZnTe system is able to achieve better than 0.6 mm FWHM for a ($A = 71\ cm,\ B = 30\ cm$) configuration using a ^{57}Co check source. The resolution can be substantially improved if different magnification is chosen. The performance could be improved with application of maximum likelihood expectation maximization (MLEM), but was not explored in this study due to the difficulty with determining a mathematically justified stopping criteria. With the application of depth-of-interaction and the proposed 3D imaging technique, the 3D distribution of special nuclear material from a stationary imager has been accomplished. This technique can assist with qualitative analysis of the objects as well as quantitative estimation of the radioactive material, such as holdup. As plutonium is very dense and highly attenuating to gamma rays, the technique will not be able to deduce the extent of the source beyond the superficial face of the material. Therefore, higher energy gamma-rays or neutron tomographic techniques will be more informative in those scenarios.

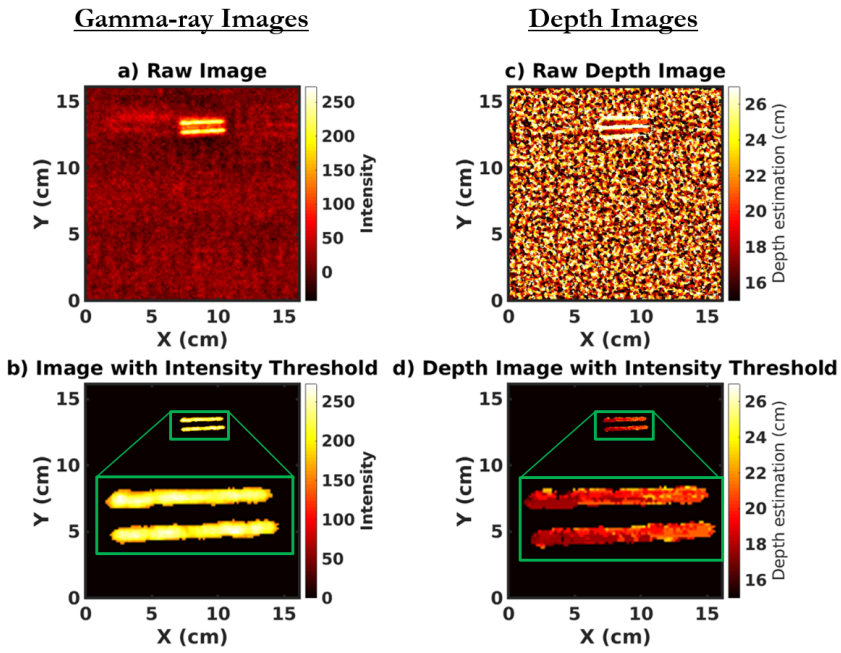

Figure 8.10: The left column presents the reconstructed gamma-ray images with with a) the raw gamma-ray image and b) image with the intensity cut. The right column presents the depth image, or the estimated source to mask distance with the c) the raw image and d) with the intensity cut mask from sub-figure (b) of this figure.

CHAPTER IX

Closing Remarks

9.1 Summary of Accomplished Work

The main topic of this dissertation revolves around super-MeV gamma-ray imaging. Chap. III discusse the various artifacts that could arise during the imaging process. One of the major artifacts in 3-or-more interaction events stem from missequenced events. To mitigate that, a sequencing algorithm, which fixes the largest deposited energy in an event chain as the first interaction in the sequence (FIL-MSD), was developed and presented in Chap IV. FIL-MSD displayed an increase of 20% in correctly sequenced events in simulated data and displayed an increased signal-to-noise ratio of nearly a factor of two in experimental images.

Next, work was completed on filtered backprojection for 3-interaction events. This was accomplished by developing an analytical point spread function that took missequencing into account. Next, attention was given to the Wiener deconvolution process in order to formulate it for spherical harmonics. The work on FBP is summarized in Chap. VI.

Finally, some effort was given to further demonstrate the detector's 3D imaging capabilities, summarized in Chap. VII. Next, 3D imaging of extended objects using time encoded imaging was also shown along with the improvements in the image resolution when using sub-pixel estimation. The work on TEI is elaborated in Chap. VIII.

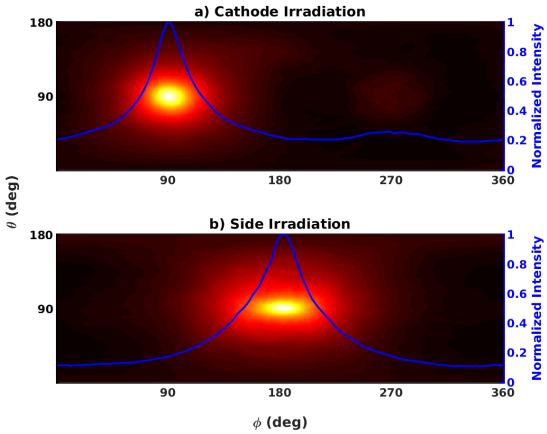

Figure 9.1: Simple backprojection images of a Cs-137 source located in a) $(90°, 90°)$ and b) $(180°, 90°)$ to demonstrate the shift-variant nature of the PSF. The blue line trace presents an azimuthal cross section along the polar 90° slice.

9.2 Closing Remarks and Future Work

It is fascinating that improvements via innovation and invention are still possible by the Orion Group on a such a 'mature' piece of technology. The Orion group saw 30 previous graduate students[1], several post-doctoral researchers, a spin-off company[2], and of course Dr. He. What makes it more captivating is that there is still a lot of work to do.

9.2.1 Compton Imaging

Compton imaging using CdZnTe still has room for improvement. FBP has been an under-explored asset in the Orion group. Its computationally cheap and high resolution advantages are not fully studied. The major obstacle in its advancing is the shift-variant nature of the point spread function of the imager, as shown in Fig. 9.1. The Wiener filter assumes a shift-invariant system and therefore might not be ideal.

In this work, we assume white (Gaussian) noise, which is not a fair assumption. The assumption of constant SNR in frequency must be mitigated or removed.

[1] I include the TlBr group and Drs. Wen Li and Daniel Lingenfelter in this count.
[2] H3D Inc.

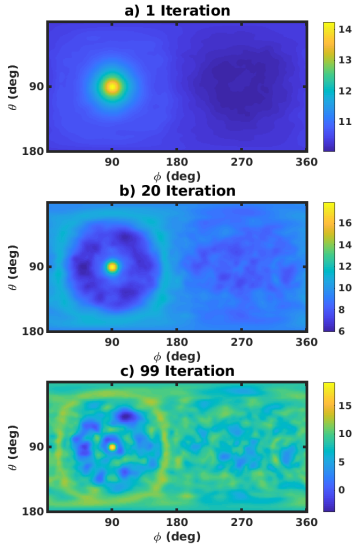

Figure 9.2: The logarithm of MLEM images with different iterations of a simulated 1.2 MeV source. Only correct sequences and photopeak events were considered. No pair-production or charge-sharing was added and pixelation of the detector was removed.

Next, using MLEM in high-energy gamma-ray imaging produces several artifacts. This is possibly due to the system response that is not adequately modeled for gamma-detector interactions. This can be seen in Fig. 9.2, which displays a concentric ring around the true source location. I currently attribute them to the edges of large scatter angle rings. Perhaps better modeling of the system response will alleviate some of these artifacts.

Electron tracking will also be a superb asset to the detector imaging resolution. Electron tracking will allow for a highly directionalized event reconstruction using the momentum of the electron. That is however, unlikely with the current large pixel-pitch anode. It may however be possible for very high energies due to the larger size of the electron cloud.

Finally, imaging gamma rays in the presence of a large continuum has been explored via the usage of differential imaging [95], but has been applied to only SBP. A good candidate for this technique would be to use it in conjuncture with FBP, which is a

linear process and does not come with the added challenges of an iterated process like MLEM.

Removal of continuum noise has been successful in MLEM with what the Orion group calls EIID [24,26]. It presents a good solution, but will be limited when shielding is present around the detector or source. It therefore might not make a good candidate for certain applications like imaging prompt gammas from proton therapy. Further investigation is required to fully explore all the possibilities.

9.2.2 3D Imaging

In order to fully elevate the 3D capabilities of the system, the 3D pose estimation method must be made more robust. This work explored the use of a foot-mounted IMU to estimate pose, but an assumption is still made about the orientation of the detector relative to that IMU. The assumption can be relaxed with the placement of a second IMU on the detector itself. This would make it a free moving detector.

Next, algorithmic changes must be made to the image reconstruction. Depending on the situation, the statistics will vary. The system will work with a large data set, but a count-starved scenario will be relatively challenging.

9.2.3 Time Encoded Imaging

The current time encoded imaging system is very well-engineered and develops high quality images. It could be improved on by stabilizing the mask and preventing further wobble. Algorithmic changes could be made to increase the resolution in low count rate scenario, such as HEU imaging. It is perhaps advantageous to look at machine learning[3] techniques.

For applications in quantitative imaging, the effect of deadtime in image reconstruction must be accounted for. Dr. Goodman has completed some studies on the

[3]It seems that machine learning and AI presents the new alchemy to problem solving.

effect of dead time on image performance but has found little effect. However, it may have an effect for quantification applications.

Mischief Managed!

- J.K. Rowling, *Harry Potter and the Prisoner of Azkaban*

BIBLIOGRAPHY

BIBLIOGRAPHY

[1] V. Schönfelder, A. Hirner, and K. Schneider, "A telescope for soft gamma ray astronomy," *Nuclear Instruments and Methods*, vol. 107, no. 2, pp. 385 – 394, 1973.

[2] E. Draeger, D. Mackin, S. Peterson, H. Chen, S. Avery, S. Beddar, and J. C. Polf, "3d prompt gamma imaging for proton beam range verification," *Physics in Medicine & Biology*, vol. 63, no. 3, p. 035019, 2018.

[3] K. Vetter, R. Barnowksi, A. Haefner, T. H. Joshi, R. Pavlovsky, and B. J. Quiter, "Gamma-ray imaging for nuclear security and safety: Towards 3-d gamma-ray vision," *Nuclear Instruments and Methods in Physics Research Section A: Accelerators, Spectrometers, Detectors and Associated Equipment*, vol. 878, pp. 159 – 168, 2018.

[4] G. F. Knoll, *Radiation Detection and Measurement*. John Wiley & Sons, Inc., 2010.

[5] E. R. M. B.Sc., "Viii. uranium radiation and the electrical conduction produced by it," *The London, Edinburgh, and Dublin Philosophical Magazine and Journal of Science*, vol. 47, no. 284, pp. 109–163, 1899.

[6] P. Villard, "Sur la reflexion et la refraction des rayons cathodiques et des rayons deviables du radium," *Comptes rendus*, vol. 130, pp. 1010–1012, 1900.

[7] P. Lenard, "Ueber die lichtelektrische wirkung," *Annalen der Physik*, vol. 313, no. 5, pp. 149–198, 1902.

[8] A. Einstein, "Uber einen die erzeugung und verwandlung des lichtes betreffenden heuristischen gesichtspunkt," *Annalen der Physik*, vol. 322, no. 6, pp. 132–148, 1905.

[9] A. H. Compton, "A Quantum Theory of the Scattering of X-rays by Light Elements," *Physical Review*, vol. 21, pp. 483–502, May 1923.

[10] J. Chadwick, P. M. S. Blackett, and G. Occhialini, "New evidence for the positive electron," *Nature*, vol. 131, no. 3309, pp. 473–473, 1933.

[11] C. D. Anderson, "The apparent existence of easily deflectable positives," *Science*, vol. 76, no. 1967, pp. 238–239, 1932.

[12] J. Xia, *Interaction Reconstruction in Digital 3-D CdZnTe Under Various Circumstances*. PhD thesis, University of Michigan, 2019.

[13] Y. Zhu, S. E. Anderson, and Z. He, "Sub-pixel position sensing for pixelated, 3-d position sensitive, wide band-gap, semiconductor, gamma-ray detectors," *IEEE Transactions on Nuclear Science*, vol. 58, pp. 1400–1409, June 2011.

[14] J. Chu, *Advanced Imaging Algorithms with Position-Sensitive Gamma-Ray Detectors*. PhD thesis, University of Michigan, 2018.

[15] C. E. Lehner and Z. He, "Image artifacts resulting from gamma-ray tracking algorithms used with compton imagers," in *IEEE Symposium Conference Record Nuclear Science 2004.*, vol. 3, pp. 1599–1603 Vol. 3, Oct 2004.

[16] J. A. Gubner, *Probability and Random Processes for Electrical and Computer Engineers*. Cambridge University Press, 2006.

[17] J. Chu, M. Streicher, J. A. Fessler, and Z. He, "Unbiased filtered back-projection in 4π compton imaging with 3d position sensitive detectors," *IEEE Transactions on Nuclear Science*, vol. 63, pp. 2750–2756, Dec 2016.

[18] H. Barrett and W. Swindell, *Radiological Imaging: The Theory of Image Formation, Detection, and Processing*. Elsevier Inc., 12 2012.

[19] N. Wiener, *Extrapolation, Interpolation, and Smoothing of Stationary Time Series*. The MIT Press, 1964.

[20] C. E. Lehner, Z. He, and F. Zhang, "4 pi compton imaging using a 3-d position-sensitive cdznte detector via weighted list-mode maximum likelihood," *IEEE Transactions on Nuclear Science*, vol. 51, pp. 1618–1624, Aug 2004.

[21] D. Goodman, *Passive Characterization of Unknown Spaces Using Large-Volume Pixelated CdZnTe*. PhD thesis, University of Michigan, 2019.

[22] C. Wahl, *Imaging, Detection, and Identification Algorithms for Position-Sensitive Gamma-Ray Detectors*. PhD thesis, University of Michigan, 2011.

[23] J. Chu, *Advanced Imaging Algorithms with Position-Sensitive Gamma-Ray Detectors*. PhD thesis, University of Michigan, 2018.

[24] W. Wang, C. G. Wahl, J. M. Jaworski, and Z. He, "Maximum-likelihood deconvolution in the spatial and spatial-energy domain for events with any number of interactions," *IEEE Transactions on Nuclear Science*, vol. 59, pp. 469–478, April 2012.

[25] A. W. Strong, "Maximum entropy imaging of comptel data," in *Imaging in High Energy Astronomy* (L. Bassani and G. Di Cocco, eds.), (Dordrecht), pp. 97–102, Springer Netherlands, 1995.

[26] D. Xu, *Gamma-ray imaging and polarization measure using 3-d position-sensitive CdZnTe detectors*. PhD thesis, University of Michigan, 2006.

[27] S. J. Wilderman, N. H. Clinthorne, J. A. Fessler, and W. L. Rogers, "List-mode maximum likelihood reconstruction of compton scatter camera images in nuclear medicine," in *1998 IEEE Nuclear Science Symposium Conference Record. 1998 IEEE Nuclear Science Symposium and Medical Imaging Conference (Cat. No.98CH36255)*, vol. 3, pp. 1716–1720 vol.3, Nov 1998.

[28] L. A. Shepp and Y. Vardi, "Maximum likelihood reconstruction for emission tomography," *IEEE Transactions on Medical Imaging*, vol. 1, pp. 113–122, Oct 1982.

[29] A. P. Dempster, N. M. Laird, and D. B. Rubin, "Maximum likelihood from incomplete data via the em algorithm," *Journal of the Royal Statistical Society. Series B (Methodological)*, vol. 39, no. 1, pp. 1–38, 1977.

[30] W. K. Newey and D. McFadden, "Chapter 36 Large sample estimation and hypothesis testing," *Handbook of Econometrics*, vol. 4, pp. 2111–2245, 1994.

[31] S. R. Gottesman and E. E. Fenimore, "New family of binary arrays for coded aperture imaging," *Appl. Opt.*, vol. 28, pp. 4344–4352, Oct 1989.

[32] K. F. Koral, W. L. Rogers, and G. F. Knoll, "Digital tomographic imaging with time-modulated pseudorandom coded aperture and anger camera," *Journal of Nuclear Medicine*, vol. 16, no. 5, pp. 402–413, 1975.

[33] S. Brown, *Time-Encoded Thermal Neutron Imaging Using Large-Volume Pixelated CdZnTe Detectors*. PhD thesis, University of Michigan, 2017.

[34] S. T. Brown, D. Goodman, J. Chu, B. Williams, M. R. Williamson, and Z. He, "Time-encoded gamma-ray imaging using a 3d-position-sensitive cdznte detector array," *IEEE Transactions on Nuclear Science*, 2019.

[35] J. C. Kim, W. R. Kaye, W. Wang, F. Zhang, and Z. He, "Impact of drift time variation on the compton image from large-volume cdznte crystals," *Nuclear Instruments and Methods in Physics Research Section A: Accelerators, Spectrometers, Detectors and Associated Equipment*, vol. 683, pp. 53 – 62, 2012.

[36] J. M. Verburg and J. Seco, "Proton range verification through prompt gamma-ray spectroscopy," *Physics in Medicine and Biology*, vol. 59, pp. 7089–7106, nov 2014.

[37] R. C. Runkle, D. L. Chichester, and S. J. Thompson, "Rattling nucleons: New developments in active interrogation of special nuclear material," *Nuclear Instruments and Methods in Physics Research Section A: Accelerators, Spectrometers, Detectors and Associated Equipment*, vol. 663, no. 1, pp. 75 – 95, 2012.

[38] G. A. de Nolfo, S. D. Hunter, L. M. Barbier, J. T. Link, S. Son, S. R. Floyd, N. Guardala, M. Skopec, and B. Stark, "Gamma-ray imaging for explosives detection," in *Chemical, Biological, Radiological, Nuclear, and Explosives (CBRNE) Sensing IX* (A. W. F. III and P. J. Gardner, eds.), vol. 6954, pp. 25 – 31, International Society for Optics and Photonics, SPIE, 2008.

[39] W. B. Atwood *et al.*, "The Large Area Telescope on the Fermi Gamma-ray Space Telescope Mission," *Astrophys. J.*, vol. 697, pp. 1071–1102, 2009.

[40] D. Shy and Z. He, "Gamma-ray tracking for high energy gamma-ray imaging in pixelated cdznte," *Nuclear Instruments and Methods in Physics Research Section A: Accelerators, Spectrometers, Detectors and Associated Equipment*, vol. 954, p. 161443, 2020. Symposium on Radiation Measurements and Applications XVII.

[41] D. Cullen, J. Hubbell, and L. Kissel, "Epdl97: the evaluated photo data library '97 version," *OSTI*, 9 1997.

[42] J. C. Kim, S. E. Anderson, W. Kaye, F. Zhang, Y. Zhu, S. J. Kaye, and Z. He, "Charge sharing in common-grid pixelated cdznte detectors," *Nuclear Instruments and Methods in Physics Research Section A: Accelerators, Spectrometers, Detectors and Associated Equipment*, vol. 654, no. 1, pp. 233 – 243, 2011.

[43] C. E. Lehner, *4-pi Compton imaging using a single 3-d position sensitive CdZnTe detector*. PhD thesis, University of Michigan, 2004.

[44] J. Kelley, J. Purcell, and C. Sheu, "Energy levels of light nuclei a=12," *Nuclear Physics A*, vol. 968, pp. 71 – 253, 2017.

[45] F. Berends and R. Kleiss, "Distributions for electron-positron annihilation into two and three photons," *Nuclear Physics B*, vol. 186, no. 1, pp. 22 – 34, 1981.

[46] W. R. Kaye, *Energy and Position Reconstruction in Pixelated CdZnTe Detectors*. PhD thesis, University of Michigan, 2012.

[47] W. Wang, W. R. Kaye, J. C. Kim, F. Zhang, and Z. He, "Improvement of compton imaging efficiency by using side-neighbor events," *Nuclear Instruments and Methods in Physics Research Section A: Accelerators, Spectrometers, Detectors and Associated Equipment*, vol. 687, pp. 62 – 68, 2012.

[48] R. A. Kroeger, W. N. Johnson, J. D. Kurfess, B. F. Phlips, and E. A. Wulf, "Three-Compton Telescope: Theory, Simulations, and Performance," *IEEE Transactions Nuclear Science*, vol. 49, no. 4, pp. 1887–1892, 2002.

[49] I. Lee, "Gamma-ray tracking detectors," *Nuclear Instruments and Methods in Physics Research Section A: Accelerators, Spectrometers, Detectors and Associated Equipment*, vol. 422, no. 1, pp. 195 – 200, 1999.

[50] N. Dogan, D. Wehe, and G. Knoll, "Multiple compton scattering gamma ray imaging camera," *Nuclear Instruments and Methods in Physics Research Section A: Accelerators, Spectrometers, Detectors and Associated Equipment*, vol. 299, no. 1, pp. 501 – 506, 1990.

[51] C. L. Thrall, C. G. Wahl, and Z. He, "Performance of five-or-more-pixel event sequence reconstruction for 3-D semiconductor gamma-ray-imaging spectrometers," in *2008 IEEE Nuclear Science Symposium Conference Record*, pp. 1299–1301, Oct 2008.

[52] O. Klein and Y. Nishina, "Über die streuung von strahlung durch freie elektronen nach der neuen relativistischen quantendynamik von dirac," *Zeitschrift für Physik*, vol. 52, pp. 853–868, Nov 1929.

[53] D. Maeder, R. Muller, and V. Wintersteiger, "Über die Linienform monochromatischer γ–Strahlungen im Szintillationsspektrographen. (German) [on the line shape of monochromatic gamma radiation in a scintillation spectrograph]," *Helvetica Physica Acta*, vol. Vol: 27, Mar 1954.

[54] S. Agostinelli et al., "Geant4—a simulation toolkit," *Nuclear Instruments and Methods in Physics Research Section A: Accelerators, Spectrometers, Detectors and Associated Equipment*, vol. 506, no. 3, pp. 250 – 303, 2003.

[55] J. Rigelsford, "Detection of explosives and landmines: Methods and field experience," *Sensor Review*, vol. 23, no. 4, pp. 365–366, 2003.

[56] W. C. Feldman, D. J. Lawrence, R. C. Elphic, B. L. Barraclough, S. Maurice, I. Genetay, and A. B. Binder, "Polar hydrogen deposits on the moon," *Journal of Geophysical Research: Planets*, vol. 105, no. E2, pp. 4175–4195, 2000.

[57] A. Haefner, D. Gunter, R. Barnowski, and K. Vetter, "A filtered back-projection algorithm for 4π compton camera data," *IEEE Transactions on Nuclear Science*, vol. 62, pp. 1911–1917, Aug 2015.

[58] V. Maxim, "Filtered backprojection reconstruction and redundancy in compton camera imaging," *IEEE Transactions on Image Processing*, vol. 23, pp. 332–341, Jan 2014.

[59] J. Driscoll and D. Healy, "Computing fourier transforms and convolutions on the 2-sphere," *Advances in Applied Mathematics*, vol. 15, no. 2, pp. 202 – 250, 1994.

[60] L. C. Parra, "Reconstruction of cone-beam projections from compton scattered data," *IEEE Transactions on Nuclear Science*, vol. 47, pp. 1543–1550, Aug 2000.

[61] M. A. Wieczorek and M. Meschede, "Shtools: Tools for working with spherical harmonics," *Geochemistry, Geophysics, Geosystems*, vol. 19, no. 8, pp. 2574–2592, 2018.

[62] D. Xu and Z. He, "Filtered back-projection in$4pi$compton imaging with a single 3d position sensitive cdznte detector," *IEEE Transactions on Nuclear Science*, vol. 53, pp. 2787–2796, 2006.

[63] M.-A. Parseval des Chenes, "Memoire sur les series et sur l'integration complete d'une equation aux differences partielles lineaire du second ordre, a coefficients constants," *Memoires presentes a l'Institut des Sciences, Lettres et Arts, par divers savants, et lus dans ses assemblees. Sciences, mathematiques et physiques*, vol. 1, pp. 638 – 648, 1806.

[64] B. Borden and J. Luscombe, *Essential Mathematics for the Physical Sciences*. 2053-2571, Morgan & Claypool Publishers, 2017.

[65] N. Schaeffer, "Efficient spherical harmonic transforms aimed at pseudospectral numerical simulations," *Geochemistry, Geophysics, Geosystems*, vol. 14, no. 3, pp. 751–758, 2013.

[66] R. Basko, G. L. Zeng, and G. T. Gullberg, "Application of spherical harmonics to image reconstruction for the compton camera," *Physics in Medicine and Biology*, vol. 43, pp. 887–894, Apr 1998.

[67] T. Tomitani and M. Hirasawa, "Image reconstruction from limited angle compton camera data," *Physics in Medicine and Biology*, vol. 47, pp. 2129–2145, jun 2002.

[68] M. Hirasawa and T. Tomitani, "Effect of compensation for scattering angular uncertainty in analytical compton camera reconstruction," *Physics in Medicine and Biology*, vol. 49, pp. 2083–2093, may 2004.

[69] Zhou Wang, A. C. Bovik, H. R. Sheikh, and E. P. Simoncelli, "Image quality assessment: from error visibility to structural similarity," *IEEE Transactions on Image Processing*, vol. 13, pp. 600–612, April 2004.

[70] *Multiservice tactics, techniques, and procedures for nuclear, biological, and chemical reconnaissance*. United States Department of the Army, FM 3-11.9, 2004.

[71] R. W. Todd, J. M. Nightingale, and D. B. Everett, "A proposed γ camera," *Nature*, vol. 251, no. 5471, pp. 132–134, 1974.

[72] M. Streicher, S. Brown, Y. Zhu, D. Goodman, and Z. He, "A method to estimate the atomic number and mass thickness of intervening materials in uranium and plutonium gamma-ray spectroscopy measurements," *IEEE Transactions on Nuclear Science*, vol. 63, pp. 2639–2648, Oct 2016.

[73] D. Goodman, "Single View, Ultra-Far-Field Source Detection and Absolute 3-D Localization Using HPGe and CdZnTe Detectors." (Submitted), 2018.

[74] A. Haefner, R. Barnowski, P. Luke, M. Amman, and K. Vetter, "Handheld real-time volumetric 3-d gamma-ray imaging," *Nuclear Instruments and Methods in Physics Research Section A: Accelerators, Spectrometers, Detectors and Associated Equipment*, vol. 857, pp. 42 – 49, 2017.

[75] J. Jaworski, *Compton Imaging Algorithms for Position-Sensitive Gamma-Ray Detectors in the Presence of Motion*. PhD thesis, University of Michigan, 2013.

[76] K. Vetter, R. Barnowksi, A. Haefner, T. H. Joshi, R. Pavlovsky, and B. J. Quiter, "Gamma-ray imaging for nuclear security and safety: Towards 3-d gamma-ray vision," *Nuclear Instruments and Methods in Physics Research Section A: Accelerators, Spectrometers, Detectors and Associated Equipment*, vol. 878, pp. 159 – 168, 2018. Radiation Imaging Techniques and Applications.

[77] D. Hellfeld, P. Barton, D. Gunter, A. Haefner, L. Mihailescu, and K. Vetter, "Real-time free-moving active coded mask 3d gamma-ray imaging," *IEEE Transactions on Nuclear Science*, vol. 66, pp. 2252–2260, Oct 2019.

[78] F. Mascarich, T. Wilson, C. Papachristos, and K. Alexis, "Radiation source localization in gps-denied environments using aerial robots," in *2018 IEEE International Conference on Robotics and Automation (ICRA)*, pp. 6537–6544, May 2018.

[79] M. S. Lee, D. Shy, W. R. Whittaker, and N. Michael, "Active range and bearing-based radiation source localization," in *2018 IEEE/RSJ International Conference on Intelligent Robots and Systems (IROS)*, pp. 1389–1394, Oct 2018.

[80] C. G. Wahl, W. R. Kaye, W. Wang, F. Zhang, J. M. Jaworski, A. King, Y. A. Boucher, and Z. He, "The polaris-h imaging spectrometer," *Nuclear Instruments and Methods in Physics Research Section A: Accelerators, Spectrometers, Detectors and Associated Equipment*, vol. 784, pp. 377 – 381, 2015. Symposium on Radiation Measurements and Applications 2014 (SORMA XV).

[81] Navigation Solutions LLC, "RT-BLE-001," Mar 2019.

[82] L. Ojeda and J. Borenstein, "Personal dead-reckoning system for gps-denied environments," in *2007 IEEE International Workshop on Safety, Security and Rescue Robotics*, pp. 1–6, Sep. 2007.

[83] W. R. Kaye, N. D. Bennett, C. G. Wahl, Zhong He, and Weiyi Wang, "Gamma-ray source location by attenuation measurements," in *2007 IEEE Nuclear Science Symposium Conference Record*, vol. 2, pp. 1294–1298, Oct 2007.

[84] E. Caroli, J. B. Stephen, G. Di Cocco, L. Natalucci, and A. Spizzichino, "Coded aperture imaging in x- and gamma-ray astronomy," *Space Science Reviews*, vol. 45, pp. 349–403, Sep 1987.

[85] R. Accorsi, F. Gasparini, and R. C. Lanza, "A coded aperture for high-resolution nuclear medicine planar imaging with a conventional anger camera: experimental results," *IEEE Transactions on Nuclear Science*, vol. 48, pp. 2411–2417, Dec 2001.

[86] R. S. Woolf, B. F. Phlips, A. L. Hutcheson, and E. A. Wulf, "Fast-neutron, coded-aperture imager," *Nuclear Instruments and Methods in Physics Research Section A: Accelerators, Spectrometers, Detectors and Associated Equipment*, vol. 784, pp. 398 – 404, 2015. Symposium on Radiation Measurements and Applications 2014 (SORMA XV).

[87] S. J. Kaye, W. R. Kaye, and Z. He, "Experimental demonstration of coded aperture imaging using thick 3d-position-sensitive cdznte detectors," in *2009 IEEE Nuclear Science Symposium Conference Record (NSS/MIC)*, pp. 1902–1906, Oct 2009.

[88] K. Ziock and M. Blackston, "Real time depth-of-interaction correction for coded-aperture, gamma-ray images," *Nuclear Instruments and Methods in Physics Research Section A: Accelerators, Spectrometers, Detectors and Associated Equipment*, vol. 916, pp. 56 – 65, 2019.

[89] Y. Zhu, S. E. Anderson, and Z. He, "Sub-pixel position sensing for pixelated, 3-d position sensitive, wide band-gap, semiconductor, gamma-ray detectors," *IEEE Transactions on Nuclear Science*, vol. 58, pp. 1400–1409, June 2011.

[90] Z. He, "Review of the shockley-ramo theorem and its application in semiconductor gamma-ray detectors," *Nucl. Inst. Meth. Phys. Res. A.*, vol. 463, no. 1-2, pp. 250 – 267, 2001.

[91] A. Levin, R. Fergus, F. Durand, and W. Freeman, "Image and depth from a conventional camera with a coded aperture," *ACM Trans. Graph.*, vol. 26, p. 70, 07 2007.

[92] L. J. Mitchell, B. F. Phlips, W. N. Johnson, E. A. Wulf, A. L. Hutcheson, C. J. Lister, K. D. Bynum, B. E. Leas, and G. Guadagno, "Mobile imaging and spectroscopic threat identification (misti): System overview," in *2009 IEEE Nuclear Science Symposium Conference Record (NSS/MIC)*, pp. 110–118, Oct 2009.

[93] K. P. Ziock, W. W. Craig, L. Fabris, R. C. Lanza, S. Gallagher, B. K. P. Horn, and N. W. Madden, "Large area imaging detector for long-range, passive detection of fissile material," *IEEE Transactions on Nuclear Science*, vol. 51, pp. 2238–2244, Oct 2004.

[94] A. D. Fulvio, T. Shin, T. Jordan, C. Sosa, M. Ruch, S. Clarke, D. Chichester, and S. Pozzi, "Passive assay of plutonium metal plates using a fast-neutron multiplicity counter," *Nuclear Instruments and Methods in Physics Research Section A: Accelerators, Spectrometers, Detectors and Associated Equipment*, vol. 855, pp. 92 – 101, 2017.

[95] Z. He, W. Wang, W. R. Kaye, C. G. Wahl, and J. M. Jaworski, "Reduction of background interference in a radiation image."